UNIVERSITY OF GENOVA

DOCTORAL THESIS

Modeling the flow over superhydrophobic and liquid-impregnated surfaces

Author:
Edoardo ALINOVI

Supervisor:
Prof. Alessandro BOTTARO

A thesis submitted in fulfillment of the requirements
for the degree of Doctor of Philosophy

Doctoral School in Civil, Chemical and
Environmental Engineering
Curriculum in Fluid Dynamics and Environmental Engineering

May 7, 2018

Supervisor:
Prof. Alessandro Bottaro - DICCA, University of Genova

External Reviewers:
Prof. Alfredo Pinelli - Department of Mechanical Engineering & Aeronautics, City University of London, UK
Prof. Ricardo García-Mayoral - Department of Engineering, Cambridge University, UK

Examination Committee:
Prof. Nicoletta Tambroni - DICCA, University of Genova
Prof. Ilaria Gnecco - DICCA, University of Genova
Prof. Simone Camarri - DICI, University of Pisa
Prof. Carlo Camporeale - DIATI, Polytechnic of Turin

Ph.D. program in Civil, Chemical and Environmental Engineering
Curriculum in Fluid Dynamics and Environmental Engineering
Cycle XXX

“Hunc igitur terrorem animi tenebrasque necessest non radii solis neque lucida tela diei discutiant, sed naturae species ratioque.”

Titus Lucretius Carus

Abstract

Modeling the flow over superhydrophobic and liquid-impregnated surfaces

by Edoardo ALINOVI

Superhydrophobic (SH) and liquid-impregnated surfaces (LIS) represent an interesting technique for the possible reduction of drag in applications involving the flow of liquids over solid surfaces, for a wide range of Reynolds number, from laminar to turbulent conditions. Such coatings work by the interposition of a gas/oil layer between the liquid and the solid wall, trapped by distributed microscopic roughness elements present at the wall; over the gas layer the liquid can flow with negligible friction. The present activity is focused on the numerical modeling of the slippage over such coatings and on their drag reduction performance in the turbulent regime. The problem is subdivided into two parts: a microscopic problem, accounting for the flow in the proximity of the roughness elements and a macroscopic problem, accounting for the turbulent flow over SHS/LIS, where the effect of the slippage at the wall is modeled through a proper boundary condition. The near-wall, microscopic problem, governed by the Stokes equation, is recast into an integral form and then solved using a boundary element method. The aim of the microscopic calculations, performed by varying the viscosity ratio between the fluids, is to obtain the values of the slip lengths, used to quantify slippage. The slip length are then used in the definition of Navier boundary condition, applied at the walls of a turbulent channel flow at moderate Reynolds number, solved by direct numerical simulations. The results are in excellent agreement with a theoretical model available in the literature.

Contents

List of Figures

List of Tables

To my beloved Erica

Chapter 1

Introduction

Fluid flows over and around bodies are commonplace in Nature and in technical applications. Probably, the most easy-to-understand phenomenon experienced by an arbitrary object moving through a fluid is the generation of a force which plays against its motion. The drag force is a mechanical force that usually is considered to carry with it negative effects: it reduces the velocity of cars, airplanes, ships and increases the fuel consumption together with the costs for the transportation of people and goods. It is usual to decompose the drag force into two fundamental contributions, at least in the incompressible limit: the pressure drag and the skin friction drag (see figure 1.1).

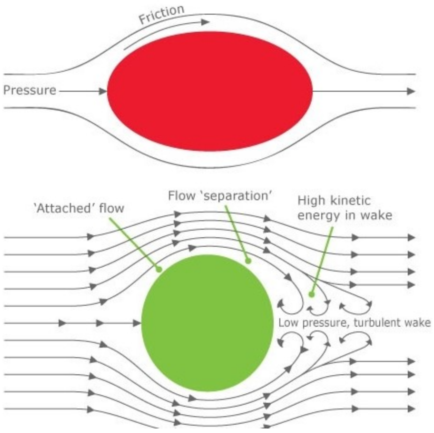

Figure 1.1: Sketch of the two kinds of drag force.

The former is associated to the pressure difference which takes place between the windward and the lee side of an object moving through a fluid. It is typical of bluff bodies that create a large wake behind them. The latter is associate to the friction between the fluid particles and the body in relative motion. It is always present, but plays an important role in streamlined bodies, where the pressure drag is negligible.

Even if the phenomenon of drag is intuitive, its physical formulation has been provided only at the beginning of the 20th century. Until then, the potential theory of the fluid motion, still in use today to estimate the lift forces, was unable to explain the mechanism of drag generation, leading Jean-Baptiste D'Alembert to formulate his famous paradox. The turning point towards the understanding of the drag force, was the idea of *boundary layer*, shown in figure 1.2, suggested by Ludwig Prandtl in 1904. He pointed out the existence of a very thin region near the body, where the velocity varies quickly from the surface value to the free stream value. In the boundary layer, the viscous forces are dominant and the friction exerted by the fluid in any point of the body turns out be

$$\boldsymbol{\tau}_w = \mu \frac{\partial \boldsymbol{u}}{\partial n}, \tag{1.1}$$

where μ is the dynamic viscosity of the fluid, $\boldsymbol{u}$ is flow velocity vector and $\boldsymbol{n}$ is the normal defined over the surface of the object.

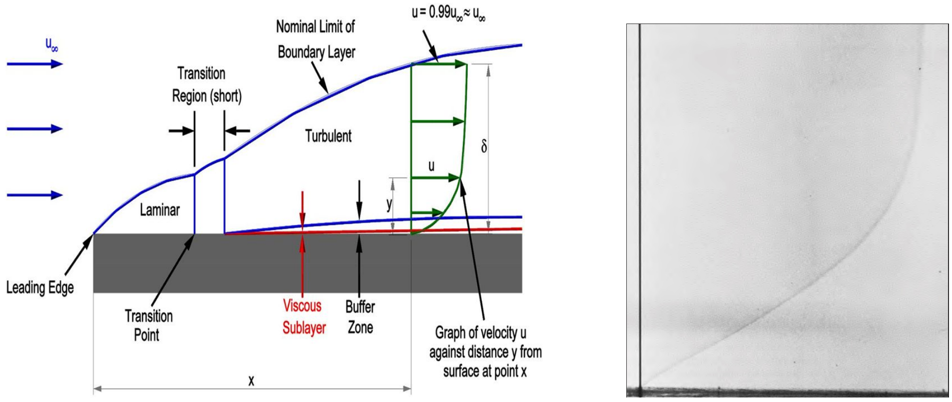

(a) (b)

Figure 1.2: Velocity boundary layer developing over a flat plate. (a) Schematic representation identifying different regimes of motion in the boundary layer; (b) flow visualization of a laminar flat plate boundary layer profile (*Wortmann, F. X. 1977 AGARD Conf. Proc. no. 224, paper 12*).

Despite the very small size of the boundary layer, the skin friction or viscous drag is currently considered a major barrier to the further optimization of most aerodynamic and hydrodynamic bodies. A large class of applications is substantially impacted by pressure drag, but there is an equally large class of devices whose performances are strongly affected by viscous drag. Among these, the sector of transport offers the best examples. The development of a low friction surface technology is of much interest for:

- high and low-speed aircraft (over 30% of skin-friction drag);
- tankers and other surface ships operating at low Froude number (50% skin-friction drag);
- underwater bodies (70% or greater skin-friction drag);

- pipelines for oil and gas transport (100% skin friction drag).

Looking beyond the pure aerodynamic/hydrodynamic performance, a viscous drag reduction of 10% immediately translates into a lower fuel consumptions, which potentially would produce savings for half a billion dollars per year to commercial transport companies. A recent study by Buhaug et al. [2009] presents the possibility of decreasing in a considerable manner the gas emissions generated by ships, if their hulls were be coated with a low friction material.

1.1 Toward skin friction drag reduction

Many efforts have been devoted to the research and development of low friction surfaces. The methods are basically subdivided into two families:

- active;
- passive.

The methods classified as active usually involves moving control surfaces, in which the motion is feed-back controlled by sensors and actuators. For examples electromagnetic tiles have been employed by Nosenchuck and Brown [1993] in order to control the boundary layer of a turbulent flow. The working principle is based on the effect exerted on a electrically conductive fluid by oscillating electric currents and magnetic fields introduced through a mosaic of surface electrodes, which applies spatially and temporally periodic body forces to the fluid reducing turbulence production. This method is only applicable in fluids with much higher electrical conductivity than ordinary air. Another popular active method is the so called micro-blowing, consisting in the upstream slot injection, or distributed injection through a porous surface, of air bubbles. Even if this technique can effectively reduce skin friction, the major drawback is the added complexity in the system design and the energy loss due to the continuous air injection.

The passive techniques do not require any external action and for this reason they are more attractive, since there is no need of a control loop, resulting in a simpler and safer usage. A passive skin friction drag reduction approach requires either a modification of the rheological properties of the fluid or a careful design of the surface. One way to alter the rheological properties of a given fluid is to inject a secondary fluid in the main stream, thus obtaining a mixture with exerts a lower friction. The drag-reducing properties of certain surfactants are known since the work of Savins [1967]. Since then, a large number of studies, mostly experiments, have been conducted and a review of the results obtained can be found in Shenoy [1976]. The surfactants that reduce drag seem to be only those that form long chains of the relatively small molecules called micelles. If a large shear is applied the chain breaks and the drag reduction effect is lost. However, this polymer has the ability to recombine together as soon as the shear stress decreases, thus restoring its properties. A drag reduction of up to 80% is found, but the working mechanism is not yet fully understood. Experiments show profound changes in the turbulent eddies, both in the near wall region and in the bulk flow, but clear indications on how to drive such changes, possibly by other actuation means, are missing. The most evident drawback of this technique is that it can be employed only with liquids in closed domains, such as pipelines; it is not applicable in external flows common in aerodynamics and hydrodynamics.

Another popular passive method, which has received much attention in the last decades, but with more modest achievements in term of drag reduction, is the technique of surface modification by riblets. The riblets are a pattern of small surface protrusions aligned approximately in the flow direction, as shown in figure 1.3(a-d).

The study on riblets has begun in the early 70s at NASA Langley Research Center [Walsh and Anders, 1989] and the first prototypes where produced by the 3M Company [Rawlings and Malone, 2014]. Their effective application outside the academic world however had a mixed success. Szodruch [1991] reported a drag reduction up to 2% for a complete Airbus 320 when the 70% of its surface was covered with riblets, but the off design working condition in real applications together with the alteration of the machined surface due to dust, ice and other external agents made difficult a large scale employment of this technology. Conversely, riblets proved their drag reduction capabilities in sporting events, such as rowing or sailing competitions, where the cost of maintenance is much less important than in commercial applications.

The physical mechanism behind the drag reduction induced by riblets is today reasonably well understood and discussed in details in Walsh [1990] and in García-Mayoral and Jiménez [2011]. In particular, the wall protrusions inhibits the lateral turbulent motion, generated by the near-wall streamwise vortices and associated to the velocity streaks in the viscous sublayer. The effectiveness of the riblets depends on their dimension with respect to the viscous length scale; referring to figure 1.3(e), the drag reduction, in terms of friction factor, presents an optimum minimum value for the ridge-to-ridge spacing, b, in wall units usually around $b^+ \approx 15$, with a positive effect surviving until $b^+ \approx 25$. If the spacing is larger than this threshold value, riblets behave like surface roughness and the effect is lost, turning drag reduction into a drag increase. The explanation of this fact was firstly given by Choi et al. [1994] and schematically depicted in figure 1.4. If the streamwise vortices in the near wall streaks are smaller than the riblets spacing, they are able to settle into the grooves and to bring high velocity fluid close to the walls, thus increasing the friction. Conversely, if the riblets are more closely spaced, the turbulent vortices are pushed away from the wall and the high velocity fluid generated by the down-wash is forced to cover a smaller area, thus diminishing the friction.

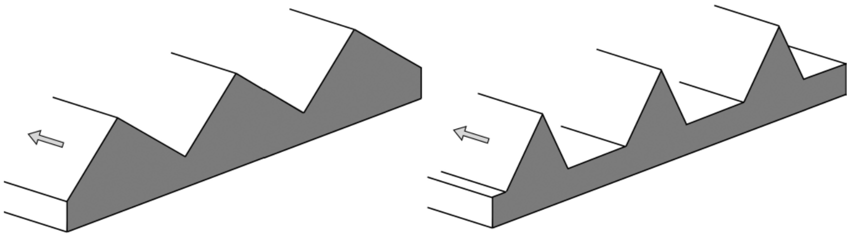

(a) Triangular riblet.   *(b)* Spaced triangular riblet.

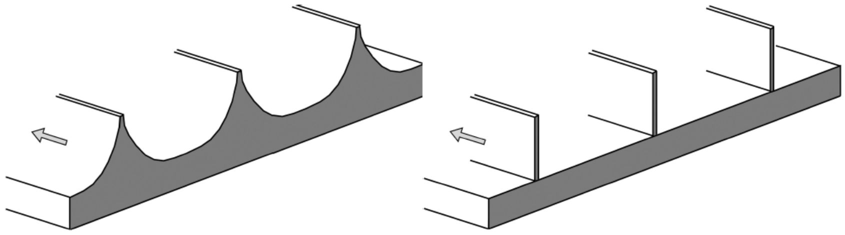

(c) U-shaped riblet.   *(d)* Blade riblet.

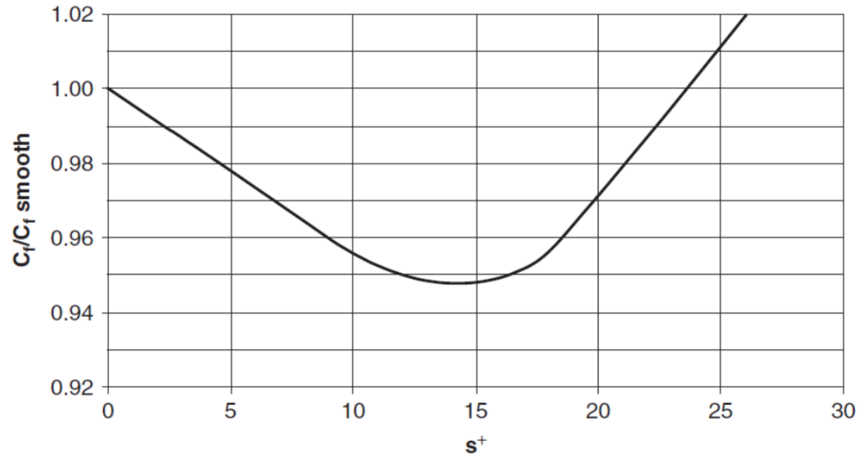

(e)

Figure 1.3: (a)-(d) Different shapes of riblets; (e) typical drag reduction curve as function of the ridge-to-ridge spacing in wall units for triangular riblets.

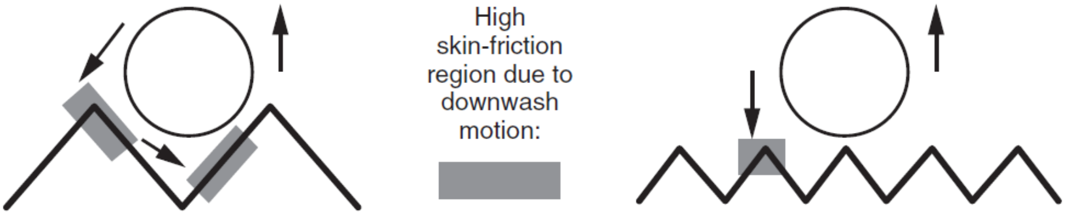

Figure 1.4: Schematic view of a wall vortex near riblets as reported by Choi et al. [1994].

1.2 Superhydrophobic and Liquid-impregnated coatings

A step forward in the design of low friction surfaces has been done by coupling the roughness elements composing the surfaces with a gas, in order to create gaseous pockets, over which a working liquid can flow with a sensible low friction. This is the case of the superhydrophobic surfaces (SHS), which today are receiving a tremendous attention. The research on SHS has been inspired by the remarkable slipping properties of the lotus leaf [Barthlott and Neinhuis, 1997]. A surface is identified as superhydrophobic on the basis of the contact angle α that a water droplet in stationary condition assumes with respect to the contact line, as shown in figure 1.5. In particular, we have the following distinctions:

- hydrophilic: $0^\circ < \alpha < 90^\circ$;
- hydrophobic: $90^\circ < \alpha < 150^\circ$;
- superhydrophobic: $\alpha > 150^\circ$.

The contact angle α depends uniquely on the physical characteristic of the three materials involved: the gas, the liquid and the solid surfaces, which intersect at the contact line. For our discussion, it is useful to introduce the interfacial energy, γ_{AB}, representing the work per unit of area required to increase the surface area of substance A in contact with B. An high value of the surface energy at the interface between a solid surface and a substance implies an affinity between the surface and the other substance, with high chances to bond. The wettability of a solid by water arises from a balance between adhesive (solid-water) and cohesive forces within the liquid. For a perfectly smooth, planar and chemically homogeneous surfaces, Young [1805] proposed a relation for the adhesion tension, A_t, which reads

$$A_t = \gamma_{SG} - \gamma_{LS} = \gamma_{GL} \cos\alpha, \tag{1.2}$$

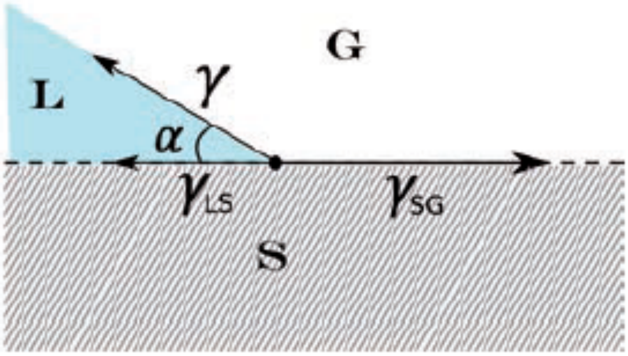

Figure 1.5: Static force balance at the triple point for a liquid (L) in contact with a solid surface (S) and surrounded by a quiescent gas (G). The greek letter γ denotes the inter-molecular forces between adjacent phases.

where the subscripts G, L, S stand for the gas, the liquid and the solid, respectively. Even if theoretically important, the expression (1.2) finds a difficult applicability since the only quantity easy to know is $\gamma_{GL} = \gamma$ (i.e. the surface tension).

Wenzel [1936] extended the work by Young with a comprehensive analysis of the wetting properties of rough materials. Within his results, he demonstrated that a rough surface increases the wetting angle, according to

$$cos(\alpha_w) = r \cos\alpha, \tag{1.3}$$

where α_w is the angle assumed on a rough surface and r is a parameter, determined experimentally, which expresses the ratio of the actual surface of the interface to its planar projection. Since $r \geq 1$, it turns out that a rough surface increases the hydrophobicity of a surface and this explains why most of the water repellent plants present micro- or nano-structures on their leafs (see figure 1.6).

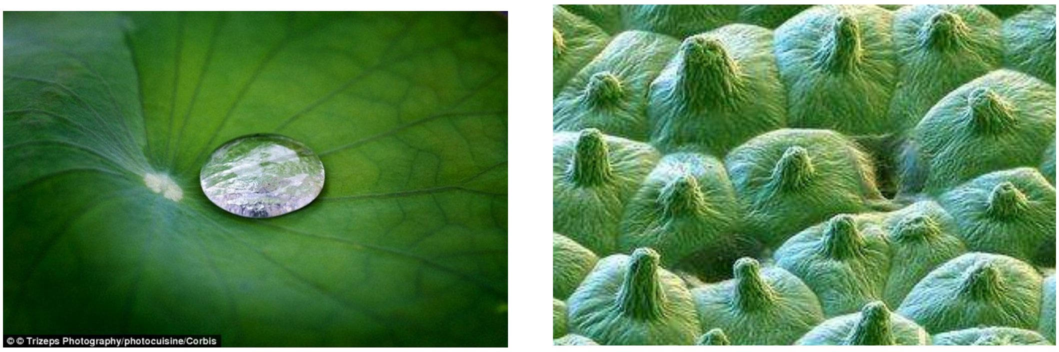

(a) (b)

Figure 1.6: A water droplet sitting on a lotus leaf (a) and the structures on the top of the same leaf at the electron microscope (b).

If air is trapped within asperities, so that the solid-liquid contact area is decreased, ultra- or super-hydrophobicity can be attained, with the drop partially sitting on an air cushion. This state, also known as Cassie-Baxter state [Cassie and Baxter, 1944], is at the basis of the functioning of SHS. In static conditions, this occurs above a critical pressure difference between the liquid and the gas, function of the roughness scale, of surface tension, and of the contact angle. Furthermore, even for a liquid pressure below critical, the transition to the Wenzel state can still take place, over longer time scales, because of the solubility of gases in water, chemical reactions or Marangoni effects. To maintain the gas layer trapped within the asperities is however difficult and the transition to the fully wetted, Wenzel state is the main problem related to SHS. The study of the aquatic plants suggests that improved robustness of the gas layer could be obtained by using a hierarchical structures of the asperities at the wall, which render the Cassie-Baxter state more energetically stable [Su et al., 2010], [Giacomello et al., 2012].

Despite its promising performances, the drawback encountered in using this technology is that the gaseous pockets lack robustness and they can easily collapse under working conditions, thus imposing a severe limitation in practical applications, especially when large scale problems and long operating times are concerned. One way to overcome this issue, is to substitute the gas trapped within the wall texture with oils, creating the so called liquid-impregnated-surfaces (LIS). The mechanism underlying the LIS technology is essentially the same identified in the SHS: the relative slip between the two fluid triggers a skin friction drag reduction. The usage of oil, instead of the gas, increases the stability of the fluid-fluid interface, and, at the same time, exhibits interesting properties in terms of biofouling [Epstein et al., 2012] and icephobicity [Ozbay et al., 2015]. However, the skin-friction drag reduction capabilities of LIS deteriorate if the oil viscosity is large compared with the viscosity of the other working fluid. This point will be stressed and supported by numerical simulations later on in this work.

There are several ways to artificially produce a wall pattern suitable for SHS and LIS, but all of them starts from two fundamentals features:

- a low surface energy material;
- a surface roughness with appropriate dimensions.

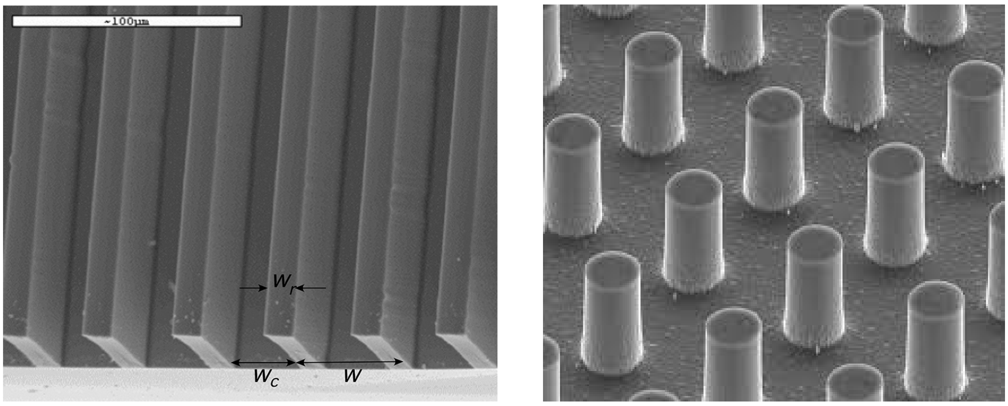

(a) (b)

Figure 1.7: Man-made superhydrophobic surfaces [Maynes et al., 2011]. (a) Longitudinal ridges; (b) pillars.

The materials often used to produce superhydrophobic coatings are polymers because of the excellent surface properties and their easy production [Shirtcliffe et al., 2004]. The drawbacks is related to their softness which renders them vulnerable to damage under working conditions; however, a simple way to produce a more resistant layer is to combine the polymer with inorganic fillers. SHS and LIS can be realized using microfabrication processes developed for the electronic industry, leading to regular arrays of microposts or microridges, as shown in figure 1.7. The high level of technology of the fabrication process and thus the relevant costs however are still considered a major problem in the realization of such coatings for large scale applications, leaving for now their usage mainly in the context of laboratory experiments [Lee and Kim, 2009, Park et al., 2014]. A cheaper alternative was introduced by Hsu and Sigmund [2010] who use a $20\mu m$ thick polycarbonate membrane filter as mold. In their techniques the polymer substrate is pressed against the mold, successively peeled off, leaving a ready-to-use hydrophobic surface. Another alternative is constituted by spray deposition, which allows to rapidly coat large areas on a variety of substrates while enhancing the stability of the Cassie-Baxter state [Srinivasan et al., 2011]. The most promising technique in term of industrial application is however obtained with the direct abrasion of the surface as proposed by Nilsson et al. [2010] who have used various grits of sandpaper to treat smooth surfaces made of Teflon. The abrasion was performed along the flow direction, obtaining good results in term of drag reduction.

1.3 Previous works

Many studies on SHS/LIS have been undertaken in the last decade because their potentialities are of much interest in the field of modern micro-fluidics, towards the development of lab-on-a-chip devices for biochemical and medical purposes [Stone et al., 2004]. Also large scale engineering devices would take advantage of low friction surfaces, especially the maritime industry could enhance the efficiency and lower the emissions by coating the ships' hulls with this particular technology. In this section a brief review on the principal works on the topic are reported. From the experimental side, Ou et al. [2004], Ou and Rothstein [2005] were the first to demonstrate the drag reduction capabilities of SHS. They focused attention on microchannels with different heights, patterned by silicon micro-posts or micro-ridges at a wall, reporting a drag reduction of up to 40% in laminar conditions. Similar drag reduction was found by Choi and Kim [2006] using a nanograted texture. Appreciable drag reduction in turbulent flows was observed by Ou and Rothstein [2009], who studied a rectangular channel with the walls coated by PDMS micro-ridges of different span and spacing. The experiment performed in the range $2000 < Re < 10000$ highlighted a skin friction drag reduction up to 50% for a large value of the slip length of approximately $80\mu m$.

The main works on LIS have been published in more recent years. As already pointed out, on the one hand the lubricant layer is more stable but, on the other hand the skin-friction drag reduction capabilities deteriorates if the oil viscosity is large compared with the viscosity of the working fluid. This behaviour was recently observed by Solomon et al. [2014], who conducted experiments with a cone and plate rheometer. They achieved a drag reduction of 16% when the impregnating fluid was two orders of magnitude less viscous than the working fluid, but little to no drag reduction with more viscous oils (with oil/fluid viscosity ratio greater than 30) . Analogue conclusions and similar drag reductions, but for a turbulent flow in a

Taylor-Couette configuration at $6000 < Re < 9000$, have been drawn by Rosenberg et al. [2016], who experimented a drag reduction of few percent for a viscosity ratio of 30, with even a drag increase for Reynolds numbers grater that 6000.

Besides the experiments, theoretical works to model slip at the walls are available. Philip [1972] was the first to study the flow past an idealized superhydrophobic flat surface, composed by alternating stripes with no-slip/no-shear boundary conditions, both aligned and perpendicular to the flow direction, by using conformal mapping. More recently, Lauga and Stone [2003] solved analytically the Stokes flow through circular channels with the same assumptions on the wall boundary conditions made by Philip. The key parameter to quantify the slippage generated by SHS or LIS is related the idea of protrusion height, or slip length, defined as the fictional distance below the surface at which the velocity field would extrapolate to zero. Mathematically speaking, the slip length concept allows to model the slip at rigid wall with the help of the Navier boundary condition [Navier, 1823]

$$\boldsymbol{u} = \boldsymbol{h}\Big(\frac{\partial \boldsymbol{u}}{\partial n}\Big), \quad \boldsymbol{h} = diag(h_{||}, h_{\perp}) \tag{1.4}$$

where n is the wall-normal coordinate, $\boldsymbol{u}$ is the vector of velocity field components in the in-plane directions and $\boldsymbol{h}$ is the slip tensor, which depends on the wall texture, while the condition for the wall normal velocity is simply $v = 0$. The condition (1.4) gives a relation between the slip velocity and the wall shear stress and is common way to model the experimental evidence of slippage over SHS and LIS. Later on, the effect of interface curvature on the slip length was studied for a flow aligned or perpendicular to periodic arrays of circular protrusions. The solution is analytic, given in terms of power expansions of the protrusion angle which quantifies how much the interface is depressing into or protruding out of the wall cavities, but only for small extension of the slip region. In particular, Davis and Lauga [2009] demonstrated that the perpendicular slip length presents a maximum for a slightly protruding bubble. Despite the theoretical limit of dilute system, their result is in good agreement with numerical simulations by Hyväluoma and Harting [2008] and Sbragaglia and Prosperetti [2007]. The longitudinal flow problem was solved in a similar fashion by Crowdy [2010], who found an increase of the slip length as the protrusion of the interface out of the wall becomes larger. His results is however slightly more sensitive to the span of the slip region, as shown by Teo and Khoo [2010], who analyzed the same problem using the finite elements method. The main assumption common in these works is that perfect slip is applied on the interface, which is a good approximation only in case the fluid trapped into the wall cavities is much less viscous than the working fluid (e.g. air-water) and the cavities deeply cave in the wall. The first attempt to remove this restriction, is due to Ng and Wang [2011], who derived a semi-analytical model for the longitudinal and transverse flow over a periodic array of circular and spherical protrusions, allowing only partial slip on the interface. The partial slip condition is rendered by using the relation (1.4), introducing an intrinsic slip length related to the interface. The solution is given in term of a series, where unknown coefficients have to be found in dependence on the slip allowed. Few years ago, with the same assumption on interface boundary condition, Crowdy [2015] extended the work of Ng and Wang [2011] by finding an explicit approximation for the longitudinal slip length using a method based on spectral functions. Schönecker and Hardt [2013] and Schönecker et al. [2014], considering a flat interface, found a closed-form analytical expressions for the flow field and effective slip length of the primary fluid explicitly containing the influence of the viscosities of the two fluids. The results were compared with numerical simulations on the same problem, giving a very good agreement.

The computational works related to quantify the drag reduction induced by SHS or LIS is mainly based on direct numerical simulations of a classical turbulent channel with various approximation on the boundary conditions at walls. The first work was conducted by Min and Kim [2004] who modeled the slip at the wall using the Navier boundary conditions. Their work highlighted the effect of the streamwise and spanwise slip, pointing out that a slip in the transverse direction enhances the turbulence, contributing to a drag increase. However, the slip lengths were arbitrarily fixed, even if to reasonable values. Taking advantage of these results, Fukagata and Kasagi [2006] proposed a theoretical model of friction drag reduction for arbitrary values of the slip lengths. Martell et al. [2009] performed numerical simulations of a turbulent flow over SHS using a variety of shear-free surface patters (longitudinal stripes or square posts) applied only at the bottom wall. The same authors extended their previous work up to $Re_\tau = 590$ [Martell et al., 2010]. In these cases the slip length was deduced as a results of the simulations and drag reduction was measured. Busse and Sandham [2012] extended the work of Min and Kim [2004] performing several numerical simulation of a turbulent channel flow exploring the influence of an anisotropic slip-length boundary condition. They also improved the analytical model proposed Fukagata and Kasagi [2006], obtaing an excellent agreement with their numerical simulations. Turk et al. [2014] gave an extensive analysis of the turbulent statistics and the secondary flows for a similar case, but with both the channel walls coated with longitudinal ridges. Seo et al. [2015] performed several DNS at $Re_\tau \approx 197$ and $Re_\tau \approx 395$ using again posts or ridges at the wall where the no-shear condition was applied to mimic the superhydrophobic effect. However, they accounted also for the deformation of the interface together with the turbulent flow, by solving the Young-Laplace equation after the pressure distribution at the wall had been determined. Later on, the same authors [Seo et al., 2018] extended their work proposing a threshold criterion for the failure of superhydrophobic surfaces and boundary maps that identify stable and unstable zones in a parameter space consisting of working parameter and design parameters including texture size and material contact angle. The numerical simulations by Luchini [2015] and, later on by Seo and Mani [2016], demonstrated that the complete no-slip/no-shear boundary conditions give equivalent results in term of drag reduction to the Navier boundary conditions, provided that extension of the shear free region does not exceed 20 wall units. This is a favorable results that allows to employ a homogeneous treatment of the wall (i.e the Navier boundary conditions) without affecting the accuracy of the results.

1.4 Aim of the present work

The present activity is focused on the numerical modeling of the slippage over SHS/LIS coatings and on their drag reduction performance in the turbulent regime. The problem is subdivided into three fundamentals parts:

- stability analysis of the flow over SHS/LIS;
- study of the microscopic flow in the proximity of the wall cavities filled with a lubricant fluid;
- Analysis of the drag reduction properties of the SHS/LIS through direct numerical simulations of the macroscopic problem.

In the first part the modal and non-modal stability analysis of a channel coated with superhydrophobic walls is performed. The superhydrophobicity is rendered through the Navier boundary condition and the calculations take into account several salient geometric and physical parameters influencing the flow stability and the energy growth of the disturbances.

In the second part, the near-wall microscopic problem, accounting for the flow in the proximity of the roughness elements is considered. The flow is governed by the Stokes equation, which is recast into an integral form and then solved using a boundary element method. The aim of the microscopic calculations, performed by varying the viscosity ratio between the fluids, is to obtain the values of the slip lengths, used to quantify slippage.

In the last part, the macroscopic problem, the slip lengths are used in the definition of Navier boundary conditions and applied at the walls of a turbulent channel flow at moderate Reynolds number, solved by direct numerical simulations.

Chapter 2

Stability of the flow in a plane microchannel with SH walls

In this chapter the modal and non-modal linear stability of the flow in a microchannel coated with either one or two SH walls is considered. The topography of the bounding walls has the shape of elongated ridges with arbitrary alignment with respect to the direction of the mean pressure gradient which drives the flow inside the microchannel. The SH walls are modeled using the Navier slip condition [Philip, 1972, Lauga and Stone, 2003] through a slip tensor, which allow us to tune the level of slippage by increasing or decreasing the values of the slip lengths. The employment of such boundary condition represents, in an homogenized sense, the alternation of no-slip and no-shear elongated regions which are found when micro-ridges cover the walls, under the assumption that the gas in the cavities exerts no shear stress on the liquid above it. Since the boundary condition is based on a linearization in the parameters $h_{||}$ and $h_{\perp}$, the results obtained are considered to be valid for values of slip lengths small enough. Luchini [2015] and Seo and Mani [2016] conducted direct numerical simulations of turbulence in a channel with two superhydrophobic walls, by comparing slip-length boundary condition cases with simulations carried out on walls with alternating no-slip and no-shear conditions (with the shear-free interface of the same length as the no-slip portion above the ribs). He found that the concept of a slip length can be employed as long as the periodicity of the longitudinal micro-ridges remains below about 20 wall units.

This same hydrodynamic stability problem has been performed by Min and Kim [2005], considering isotropic, superhydrophobic channel walls (characterized, in an averaged sense, by the same scalar *slip length*, h), and studied the case of both exponentially growing two-dimensional modes and three-dimensional pseudo-modes excited algebraically over short time intervals. Whereas two dimensional Tollmien-Schlichting (TS) waves were stabilized by the use of a non-zero slip length, the effect of slip on the transient amplification of streak-like perturbations was found to be minor; Min and Kim performed also a few direct numerical simulations of transition to turbulence initiated by two-dimensional TS waves in different configurations (in the presence of only streamwise slip, only spanwise slip, or slip along both horizontal directions) finding that in some cases transition was advanced (with respect to the no-slip situation) and in others it was retarded. From the results it appears that it is the presence of spanwise slip (which is, in all practical cases, unavoidable when superhydrophobic surfaces are used) to favour the early triggering of transition.

Also Lauga and Cossu [2005] considered isotropic, superhydrophobic surfaces using a scalar slip length to model the wall. Their modal stability results demonstrated a strong stabilizing effect for two-dimensional TS waves (particularly when both channel walls display slip), whereas only a minor influence was found on the maximum transient energy growth of streamwise streaks.

Recently, Yu et al. [2016] have re-considered the temporal, modal stability problem for the flow in a channel with longitudinal superhydrophobic grooves on one or both walls, without employing the concept of a slip length. They resolved the two-dimensional problem for the base flow in the plane orthogonal to the mean flow direction, and the two-dimensional problem for the disturbance field, assuming the interface flat and pinned at the corners of the ribs. When both the spanwise periodicity of the grooves and the shear-free fraction are sufficiently small, compared to the channel thickness, the results of Yu et al.'s analysis reproduce those obtained by employing a slip length. As the periodicity and the shear-free fraction are increased, a new wall mode is found, apparently related to the presence of inflection points in the mean, streamwise velocity profile; it is such a new mode which can lead the flow to an early instability.

The main motivation of this chapter is to understand under which conditions and parameters the most stabilizing or destabilizing effects are obtained. The results obtained give indications on transition delay or enhancement from laminar to turbulent flow and consequently on the possibility of drag reduction.

2.1 Problem formulation

The effect of superhydrophobic (SH) surfaces on the instability onset, and consequently the initial stages of laminar-turbulent transition, is addressed in the framework of plane micro-channel where the Reynolds number is typically small. We assume that the channel has thickness $2h^\star$ and use $h^\star$ to normalize distances, and the bulk speed $\bar{U}^\star$ is employed to scale the velocity. Superscript $\star$ denotes dimensional quantities.

The SH riblet-like wall considered here forms an anisotropic texture (figure 2.1) for which a slip tensor $\boldsymbol{h}$ in the plane of the walls (x, z) can be defined [Bazant and Vinogradova, 2008, Belyaev and Vinogradova, 2010, Asmolov and Vinogradova, 2012] as

$$\boldsymbol{\Lambda} = \boldsymbol{Q} \begin{bmatrix} h_{\|} & 0 \\ 0 & h_{\perp} \end{bmatrix} \boldsymbol{Q}^T, \quad \text{with} \quad \boldsymbol{Q} = \begin{bmatrix} \cos\theta & -\sin\theta \\ \sin\theta & \cos\theta \end{bmatrix}, \tag{2.1}$$

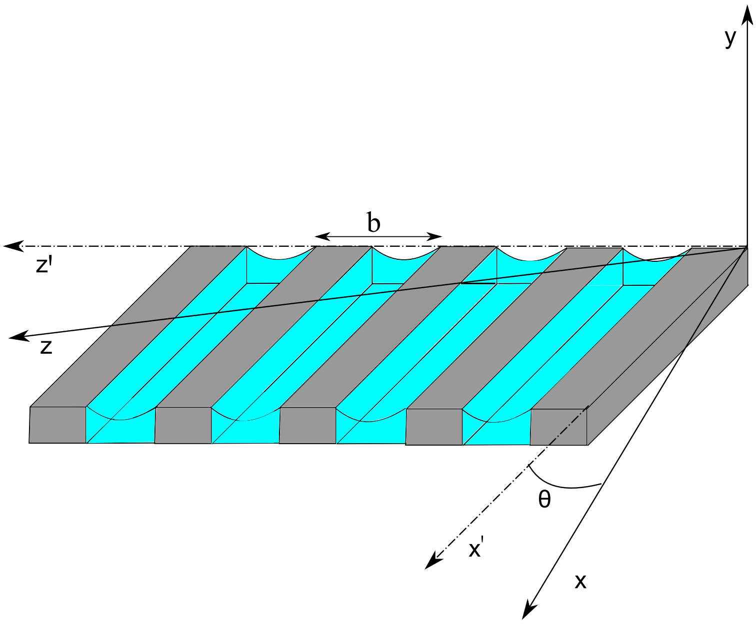

Figure 2.1: Sketch of the wall pattern with definition of axes, angle θ and ridges periodicity b. The gas-liquid interface is represented as a curved surface in light blue color for illustrative purposes; the way in which the Navier slip lengths are modified by the curvature of the interface has been addressed by Teo and Khoo [2010]

where $h_{\|}$ and $h_{\perp}$ are the eigenvalues of the slip tensor $\boldsymbol{\Lambda}$ for $\theta = 0^\circ$ and 90°, and the transformation (2.1) represents a rotation of the tensor by an angle θ. For $\theta = 0^\circ$ the ridges are aligned with x, and for $\theta = 90^\circ$ they are aligned with z. In the special case of isotropic SH it is $h_{\|} = h_{\perp}$; for the case of microridges aligned along the mean pressure gradient [Philip, 1972, Lauga and Stone, 2003, Asmolov and Vinogradova, 2012] we have $h_{\|} = 2h_{\perp}$. This latter result will be used from now on, and the results will be expressed as a function only of $h_{\|}$.

By denoting with u, v and w the streamwise, wall-normal and spanwise velocity components, respectively, the dimensionless boundary conditions for the horizontal velocity components at the two walls in $y = \pm 1$ read

$$\begin{bmatrix} u(x,-1,z) \\ w(x,-1,z) \end{bmatrix} = \boldsymbol{\Lambda} \frac{\partial}{\partial y} \begin{bmatrix} u(x,-1,z) \\ w(x,-1,z) \end{bmatrix}, \tag{2.2}$$

$$\begin{bmatrix} u(x,1,z) \\ w(x,1,z) \end{bmatrix} = -\boldsymbol{\Lambda} \frac{\partial}{\partial y} \begin{bmatrix} u(x,1,z) \\ w(x,1,z) \end{bmatrix}, \tag{2.3}$$

in the case of both walls being textured, plus vanishing conditions for the vertical velocity component v at the two walls. If one of the two walls is not superhydrophobic, the condition there is simply $\boldsymbol{u} = \boldsymbol{0}$.

2.1.1 Base flow and linear stability equations

The velocity and pressure are decomposed into a steady base flow and an unsteady disturbance according to

$$\boldsymbol{u}(x,y,z,t) = \boldsymbol{U}(x,y,z) + \epsilon \boldsymbol{u}'(x,y,z,t), \tag{2.4}$$

$$p(x,y,z,t) = P(x,y,z) + \epsilon p'(x,y,z,t), \tag{2.5}$$

with $\epsilon \ll 1$. The governing equations for plane, incompressible and steady channel flow read

$$\frac{\mathrm{d}P}{\mathrm{d}x} = \frac{1}{Re}\frac{\mathrm{d}^2 U}{\mathrm{d}y^2}, \tag{2.6}$$

where the Reynolds number is defined as $Re = \bar{U}^\star h^\star/\nu^\star$. When the boundary conditions (2.2–2.3) are used, the analytical solution of the base flow, in the case of two superhydrophobic walls, reads

$$U(y) = -3\frac{y^2 - 1 - h_{\parallel}(1+\cos^2\theta)}{2 + 3h_{\parallel}(1+\cos^2\theta)}, \quad W(y) = 3\frac{h_{\parallel}\sin\theta\cos\theta}{2 + 3h_{\parallel}(1+\cos^2\theta)}. \tag{2.7}$$

When θ differs from $0°$ and $90°$, a small component of the base flow orthogonal to the mean pressure gradient is created in the channel [Stone et al., 2004]. In the case in which only the bottom wall is superhydrophobic the basic flow is:

$$U(y) = -\frac{3}{4}\frac{(y^2-1)(8 + 6h_{\parallel} + h_{\parallel}^2) + 2h_{\parallel}(y-1)(2 + 2\cos^2\theta + h_{\parallel})}{6h_{\parallel} + 3h_{\parallel}\cos^2\theta + 4 + 2h_{\parallel}^2}, \tag{2.8}$$

$$W(y) = -3h_{\parallel}\frac{\sin\theta\cos\theta(y-1)(4 - h_{\parallel}\cos^2\theta + 2h_{\parallel})}{[4 + h_{\parallel}(1+\sin^2\theta)](6h_{\parallel} + 3h_{\parallel}\cos^2\theta + 4 + 2h_{\parallel}^2)}, \tag{2.9}$$

and this flow presents a streamwise component of the vorticity which is a maximized by $\theta = \pm 45°$ when $h_{\parallel}$ is smaller than about 0.1 (above this value of $h_{\parallel}$ the absolute value of the inclination angle of the grooves which displays the largest vorticity increases mildly). Examples of the base flow for $h_{\parallel} = 0.155$, in the case of one and two superhydrophobic walls, are displayed in figure 2.2 for two values of θ.

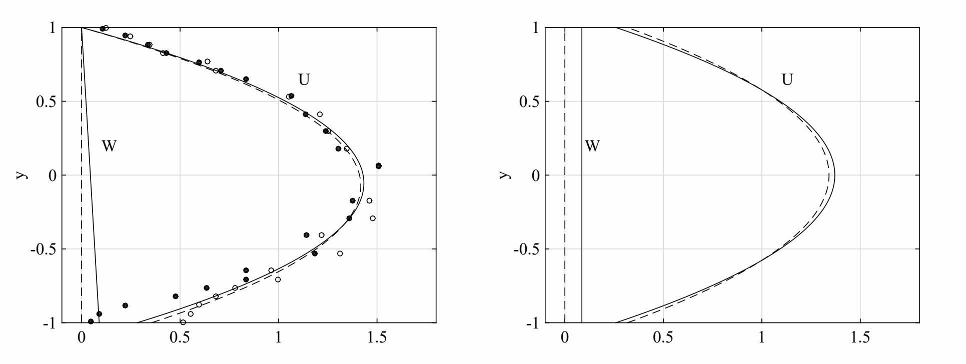

(a) (b)

Figure 2.2: Streamwise U and spanwise W velocity components of the base flow when $h_{\|} = 0.155$ for the cases $\theta = 0°$ (dashed) and $\theta = 45°$ (solid). Left: one superhydrophobic wall. Right: two superhydrophobic walls. The symbols show the experimental micro-PIV data of Ou and Rothstein [2005] for the case $\theta = 0°$; the filled circles show measurements above the ribs, whereas the empty symbols are taken above the gas-water interface.

The linear stability equations are obtained by introducing (2.4) into the Navier-Stokes equations and collecting terms of order ϵ. In primitive variable form they read:

$$\frac{\partial u'}{\partial x} + \frac{\partial v'}{\partial y} + \frac{\partial w'}{\partial z} = 0, \tag{2.10}$$

$$\frac{\partial u'}{\partial t} + U\frac{\partial u'}{\partial x} + v'\frac{\mathrm{d}U}{\mathrm{d}y} + W\frac{\partial u'}{\partial z} = -\frac{\partial p'}{\partial x} + \frac{1}{Re}\nabla^2 u', \tag{2.11}$$

$$\frac{\partial v'}{\partial t} + U\frac{\partial v'}{\partial x} + W\frac{\partial v'}{\partial z} = -\frac{\partial p'}{\partial y} + \frac{1}{Re}\nabla^2 v', \tag{2.12}$$

$$\frac{\partial w'}{\partial t} + U\frac{\partial w'}{\partial x} + v'\frac{\mathrm{d}W}{\mathrm{d}y} + W\frac{\partial w'}{\partial z} = -\frac{\partial p'}{\partial z} + \frac{1}{Re}\nabla^2 w', \tag{2.13}$$

with $\nabla^2 = \frac{\partial^2}{\partial x^2} + \frac{\partial^2}{\partial y^2} + \frac{\partial^2}{\partial z^2}$. The disturbance field (denoted by primes) is expressed in terms of Fourier modes along the wall-parallel directions, i.e.

$$q'(x, y, z, t) = \tilde{q}(y, t)\exp[i(\alpha\, x + \beta\, z)] + c.c., \tag{2.14}$$

for the generic variable q', where α and β are the streamwise and spanwise wavenumbers, respectively, and $c.c.$ denotes complex conjugate.

The theory developed is applicable as long as the disturbance wavelength $2\pi/k$, with $k = \sqrt{\alpha^2 + \beta^2}$, is sufficiently longer than the spatial periodicity b of the micro-ridges.

2.2 Numerical method

Using relation (2.14), the linearized momentum and continuity equations read

$$\begin{cases} i\alpha\tilde{u} + \dfrac{\partial v}{\partial y} + i\beta\tilde{w} = 0 \\ \dfrac{\partial \tilde{u}}{\partial t} + i\alpha\tilde{u}U + \tilde{v}\dfrac{\partial U}{\partial y} + i\beta\tilde{u}W + i\alpha\tilde{p} = \dfrac{1}{Re}\left[\dfrac{\partial^2\tilde{u}}{\partial y^2} - (\alpha^2+\beta^2)\tilde{u}\right] \\ \dfrac{\partial \tilde{v}}{\partial t} + i\alpha\tilde{v}U + i\beta\tilde{v}W + \dfrac{\partial \tilde{p}}{\partial y} = \dfrac{1}{Re}\left[\dfrac{\partial^2\tilde{v}}{\partial y^2} - (\alpha^2+\beta^2)\tilde{v}\right] \\ \dfrac{\partial \tilde{w}}{\partial t} + i\alpha\tilde{w}U + \tilde{v}\dfrac{\partial W}{\partial y} + i\beta\tilde{w}W + i\beta\tilde{p} = \dfrac{1}{Re}\left[\dfrac{\partial^2\tilde{w}}{\partial y^2} - (\alpha^2+\beta^2)\tilde{w}\right]. \end{cases} \tag{2.15}$$

In compact form, introducing the vector $\tilde{\boldsymbol{q}} = (\tilde{u}, \tilde{v}, \tilde{w}, \tilde{p})^T$, we can recast system (2.15) as

$$\boldsymbol{C}\frac{\partial \hat{\boldsymbol{q}}}{\partial t} = \boldsymbol{D}\tilde{\boldsymbol{q}}, \tag{2.16}$$

with $\boldsymbol{C}$ and $\boldsymbol{D}$ diagonal matrices of size 4×4. For the classical no-slip wall, the boundary conditions simply read

$$\tilde{u} = \tilde{v} = \tilde{w} = 0, \tag{2.17}$$

while considering for example the bottom wall as superhydrophobic, we have

$$\tilde{u} - \frac{\lambda}{2}[(1+\cos^2\theta)\frac{\partial \tilde{u}}{\partial y} + \sin\theta\cos\theta\frac{\partial \tilde{w}}{\partial y}] = 0, \tag{2.18}$$

$$\tilde{w} - \frac{\lambda}{2}[(1+\sin^2\theta)\frac{\partial \tilde{w}}{\partial y} + \sin\theta\cos\theta\frac{\partial \tilde{u}}{\partial y}] = 0. \tag{2.19}$$

The modal analysis is performed by assuming a temporal behaviour of the form

$$\tilde{q}(y,t) = \hat{q}(y)\exp(-i\,\omega\,t), \tag{2.20}$$

where ω is the complex angular frequency and $\omega_i > 0$ denotes unstable solutions. Substituting the asymptotic temporal behaviour (2.20) into the linearized equations (2.15) yields a generalized eigenvalue problem. In discrete form the resulting system of equations can be written as

$$i\omega\boldsymbol{B}\hat{\boldsymbol{q}} = \boldsymbol{A}\hat{\boldsymbol{q}}, \tag{2.21}$$

where $\hat{\boldsymbol{q}} = (\hat{u}, \hat{v}, \hat{w}, \hat{p})$; $\boldsymbol{A}$ and $\boldsymbol{B}$ are complex-valued $4n \times 4n$ matrices and n is the number of discrete points taken in the y-direction. The equations are discretized on a staggered grid and the spatial derivatives are treated with second order finite differences; a uniform grid is adopted along the y-direction and 300 discrete points are sufficient to obtain converged eigenvalues, with errors with respect to reference solutions lower than 0.1%. The solution for $\hat{\boldsymbol{q}}$ and ω is found using the inverse-iteration iterative algorithm [Golub and Van Loan, 1989].

The non-modal behaviour is studied by computing the maximum finite-time amplification; the initial disturbance velocity field, $\tilde{\boldsymbol{u}}_0$, is *optimal* when the gain

$$G(Re, \alpha, \beta, T, h_{\parallel}, \theta) = \frac{e(T)}{e(0)}, \tag{2.22}$$

is maximized, where

$$e(t) = \frac{1}{2}\int_{-1}^{1} (\tilde{u}\tilde{u}^* + \tilde{v}\tilde{v}^* + \tilde{w}\tilde{w}^*)dy,$$

and T is the target time of the optimization. This is conducted by introducing Lagrange multipliers enforcing the constraints given by the governing linear equations and the boundary conditions. The corresponding adjoint equations are derived using a discrete approach [Luchini and Bottaro, 2014]. We further define

$$G_M(Re, h_{\parallel}, \theta) = \max_{\forall \alpha, \beta, T} G,$$

when G is maximized with respect to the wavenumbers (α, β) and the final time T. The final time and spanwise wavenumber corresponding to G_M are denoted T_M and β_M, respectively. The discrete counterpart of system (2.16) is advanced in time using a second order accurate in time scheme reading

$$\boldsymbol{L}\boldsymbol{q}^{n+1} = \boldsymbol{f}, \boldsymbol{L} = \frac{3}{2}\frac{\boldsymbol{B}}{\Delta t} + \boldsymbol{A}, \boldsymbol{f} = \frac{\boldsymbol{B}}{\Delta t}\left[2\boldsymbol{q}^n - \frac{1}{2}\boldsymbol{q}^{n-1}\right]. \tag{2.23}$$

The code used to compute the non-modal growth has been tested on several cases found in the literature (using no-slip boundary conditions); in particular, the value of the optimal gain $G_M = 2 \times 10^{-4}\, Re^2$ and the corresponding time at which it is achieved, $T_M = 0.076\, Re$, with $\alpha = 0$ and $\beta = 2.04$, are recovered within less than 0.1% [Schmid and Henningson, 2001]. Results are obtained imposing that convergence is reached when the relative difference in gain between two consecutive iterations is below 10^{-8}.

2.3 A digression on Squire's theorem and Squire modes

In a channel with no-slip walls, Squire's theorem states that the instability of the coupled system stems from the amplification of a two-dimensional Orr-Sommerfeld mode [Schmid and Henningson, 2001]. This is proven by applying Squire's transformation ($k\, u_{2D} = \alpha\hat{u} + \beta\hat{w}$; $k\, Re_{2D} = \alpha\, Re$; $p_{2D}/k = \hat{p}/\alpha$; $v_{2D} = \hat{v}$; $\omega_{2D}/k = \omega/\alpha$) to the linearized system. The result is that, if a three-dimensional mode is unstable, a two-dimensional mode will be unstable at a lower value of the Reynolds number, $Re_{2D} = \alpha\, Re/k \leq Re$. Furthermore, it can be shown, always in the no-slip case, that Squire modes (eigensolutions of the unforced Squire's equation for the vertical vorticity component) are always damped. In the present wall-slip case, however, the statements above do not necessarily apply.

By decomposing the velocity vector $\hat{\boldsymbol{u}} = (\hat{u}, \hat{v}, \hat{w})$ into components parallel and perpendicular to the wavenumber vector, i.e.

$$u_{\parallel} = \frac{(\alpha\hat{u} + \beta\hat{w})}{k}, \quad u_{\perp} = \frac{(\beta\hat{u} - \alpha\hat{w})}{k},$$

the governing equations satisfied by $(u_{\parallel}, v_{2D}, p_{2D})$ are independent of $u_{\perp}$:

$$iku_{\parallel} + \frac{\mathrm{d}v_{2D}}{\mathrm{d}y} = 0, \tag{2.24}$$

$$-i\omega_{2D}u_{\parallel} + ik\overline{U}u_{\parallel} + \frac{\mathrm{d}\overline{U}}{\mathrm{d}y}v_{2D} = -ikp_{2D} + \frac{1}{Re_{2D}}(\frac{\mathrm{d}^2}{\mathrm{d}y^2} - k^2)u_{\parallel}, \tag{2.25}$$

$$-i\omega_{2D}v_{2D} + ik\overline{U}v_{2D} = -\frac{\mathrm{d}p_{2D}}{\mathrm{d}y} + \frac{1}{Re_{2D}}(\frac{\mathrm{d}^2}{\mathrm{d}y^2} - k^2)v_{2D}. \tag{2.26}$$

Whereas at first sight this appears to imply that Squire's theorem is satisfied, it is not the case, since (*i*) the base flow of this new two-dimensional problem is different from U (it is $\overline{U} = U + \frac{\beta}{\alpha}W$) and (*ii*) the boundary conditions for the parallel component of the velocity do not decouple, i.e. at $y = \pm 1$ the boundary conditions are expressed in terms of both $u_{\parallel}$ and $u_{\perp}$. The decoupling of the problem into two separate problems (a homogeneous problem for $(u_{\parallel}, v_{2D}, p_{2D})$ and a second problem for $u_{\perp}$, forced by v_{2D}) is possible only in the case of isotropic SH walls (i.e. $\lambda_{\parallel} = \lambda_{\perp}$ and $W = 0$), and it is only in this case that Squire's theorem holds.

Furthermore, the fact that Squire modes are not necessarily damped can be seen by considering the equation for the velocity component perpendicular to the wavevector, i.e.

$$\left[-i\omega + i\alpha U + i\beta W - \frac{1}{Re}\left(\frac{\mathrm{d}^2}{\mathrm{d}y^2} - k^2\right)\right]u_{\perp} = \left(\beta\frac{\mathrm{d}U}{\mathrm{d}y} - \alpha\frac{\mathrm{d}W}{\mathrm{d}y}\right)\frac{v_{2D}}{k}, \tag{2.27}$$

known as Squire's equation. By multiplying the unforced equation (2.27) by $u_{\perp}^*$, with the $*$ superscript denoting complex conjugate, and integrating in y across the fluid domain, we find

$$\omega\int_{-1}^{1} u_{\perp}^* u_{\perp}\ dy = \int_{-1}^{1}\left[(\alpha U + \beta W)u_{\perp}^* u_{\perp} + \frac{i}{Re}u_{\perp}^*(\frac{d^2}{dy^2} - k^2)u_{\perp}\right]\mathrm{d}y. \tag{2.28}$$

Integrating by parts once and taking the imaginary part (subscript i denotes imaginary part, subscript r denotes real part) we are left with

$$\omega_i\int_{-1}^{1}|u_{\perp}|^2\ dy = -\frac{1}{Re}\int_{-1}^{1}\left(\left|\frac{\mathrm{d}u_{\perp}}{\mathrm{d}y}\right|^2 + k^2|u_{\perp}|^2\right)\mathrm{d}y + \frac{A}{Re}, \tag{2.29}$$

where

$$A = \frac{1}{k^2}\left[\alpha^2\left(\hat{w}_r\frac{d\hat{w}_i}{dy} - \hat{w}_i\frac{d\hat{w}_r}{dy}\right) + \beta^2\left(\hat{u}_r\frac{d\hat{u}_i}{dy} - \hat{u}_i\frac{d\hat{u}_r}{dy}\right) + \right.$$
$$\left. + \alpha\beta\left(\hat{u}_i\frac{d\hat{w}_r}{dy} + \hat{w}_i\frac{d\hat{u}_r}{dy} - \hat{u}_r\frac{d\hat{w}_i}{dy} - \hat{w}_r\frac{d\hat{u}_i}{dy}\right)\right]_{-1}^{1}. \qquad (2.30)$$

There is no evident reason why A, which contains boundary terms arising from integration by parts, should be negative (or positive and small, so as not to render positive the right-hand-side of equation (2.29); thus, Squire modes (characterized by $\hat{v} \equiv 0$ throughout y) can, in principle, be amplified (since ω_i in equation (2.29) is not necessarily negative).

In our experience, however, Squire modes remain damped (cf. Section III), both those in the so-called A branch (also known as *wall modes*) and those in the P branch (*center modes*). Conversely, recent results by Szumbarski [2007] and Mohammadi et al. [2015] for the flow in channels with streamwise-invariant and spanwise-periodic corrugations demonstrate that it is precisely the least stable Squire mode (in the P branch) which can become unstable for a sufficiently large corrugation amplitude. When the amplitude of the corrugation exceeds a value of $\mathcal{O}(10^{-2})$ an inviscid mechanism – driven by the spanwise gradient of the main velocity component – forces the destabilisation of the Squire *center* mode. These findings are related to those by Yu et al. [2016], who focussed however on *wall* modes. We re-emphasize here that the rough walls considered have spatial scales sufficiently small for an homogenisation procedure – leading to the Navier-slip concept – to be tenable.

2.4 Modal analysis

We initiate the discussion of the modal results by showing some representative behaviors for the case of a single superhydrophobic wall. Figure 2.3 (top, left) illustrates the variation of the growth rate ω_i of the most unstable (or least stable) Orr-Sommerfeld (OS) mode as a function of the slip length, for the parameters indicated in the figure's caption. The wave angle considered is $\Phi = tan^{-1}\beta/\alpha = 20°$; this three-dimensional mode is initially damped at low $h_{\|}$. However, past a threshold value of the slip length, the mode becomes unstable with a maximum growth rate which is achieved at $h_{\|} = 0.25$. The disturbance mode shapes in correspondence to this point are plotted in the left frame, center row, of figure 2.3; they correspond to classical OS eigenfunctions, asymmetric about $y = 0$ because of the slip condition at $y = -1$. On the right side of figure 2.3 the behavior of a different mode is represented, at a much smaller value of the Reynolds number than the one considered so far. This instability mode displays a comparable behavior of the growth rate as a function of $h_{\|}$ (an initial decrease of ω_i, followed by an increase, with a maximum amplification for $h_{\|} = 0.15$), but radically different eigenfunctions, displayed in the center row, right frame.

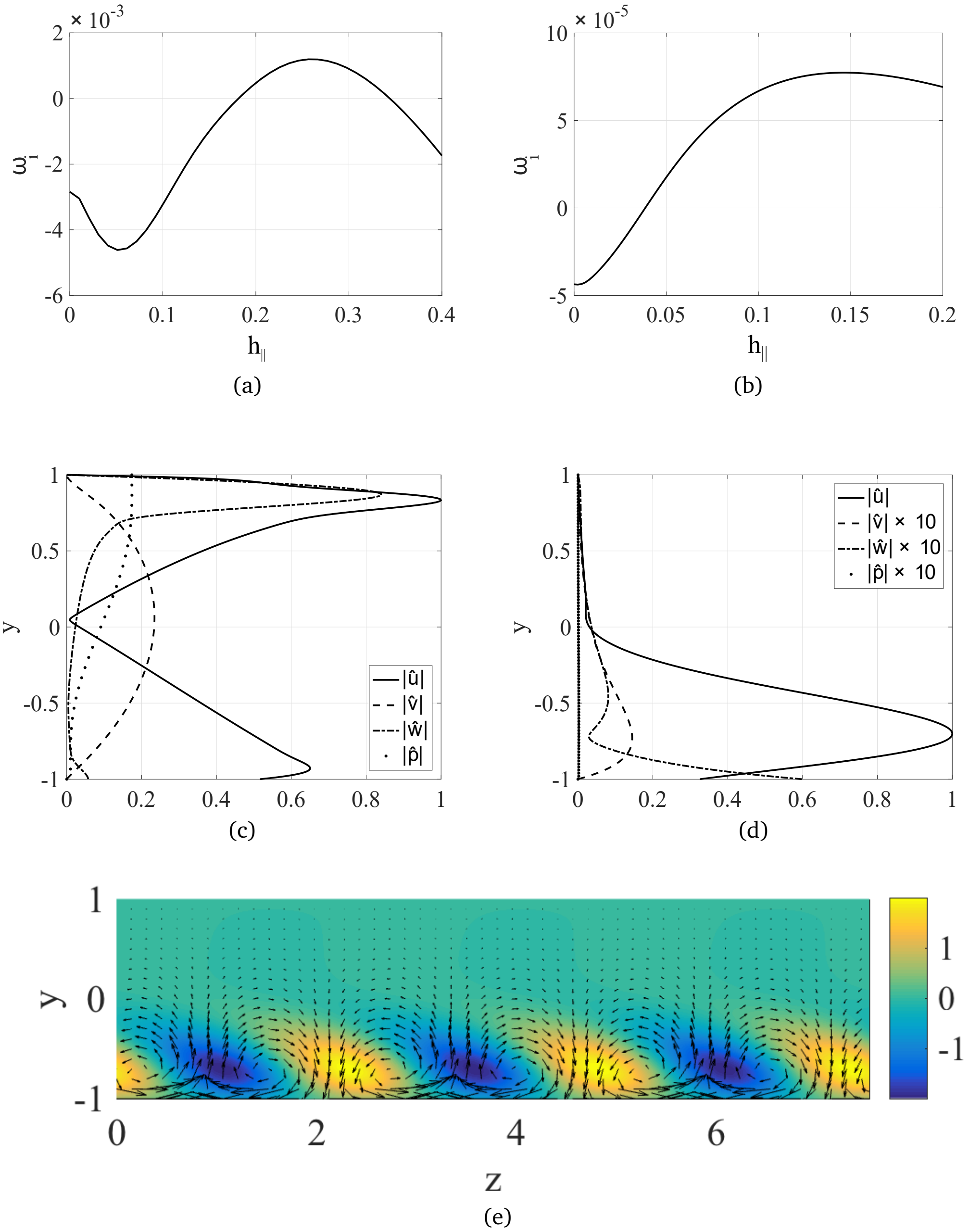

(a)

(b)

(c)

(d)

(e)

Figure 2.3: Growth rate ω_i as a function of $h_{\|}$ and absolute value of the disturbance velocity components and disturbance pressure, using one SH wall. (a)-(c) $Re = 10000$, $\theta = 80°$, $\Phi = 20°$ and $\alpha = 0.65$; (b)-(d) $Re = 2000$, $\theta = 45°$, $\Phi \approx 90°$ and $\alpha \approx 0$. The values of $h_{\|}$ in the middle row, where eigenfunctions are plotted, correspond to the maximum growth rate for the respective case, i.e. 0.25 and 0.145. (e) Contours, in the (y, z) plane, of the positive and negative streamwise disturbance velocity component relative to the case in the right column over three spanwise periods $(\beta = 2.5)$. The vectors represent wall-normal and spanwise components.

This mode, which is found to be dominating when the ridges are at an angle around 45^o to the mean pressure gradient, takes the form of near-wall vortices, as exemplified on the bottom frame of figure 2.3. Alternating high and low speed streaks, elongated in the streamwise direction x ($\alpha = 10^{-3}$ in all the calculations for which we state $\alpha \approx 0$, the case α exactly equal to zero being ill-posed numerically), are present near the SH wall, with corresponding low amplitude secondary vortices. While it is not a surprise that inclined ridges at the wall yield low frequency streamwise or quasi-streamwise vortices, it is remarkable that this behavior is rendered so clearly by the homogenized Navier-slip boundary condition. This new instability mode depends crucially on the wall ridges' amplitude (a threshold value $h_{||} = 0.038$ is found with the present settings) and orientation with respect to the mean pressure gradient (i.e. θ), and displays a temporal amplification factor typically larger than the most unstable three-dimensional OS wave (cf. the top two frames of the figure).

It is now instructive to examine the spectra, in terms of either the complex phase speed c or the complex frequency ω, depending on the value of the streamwise wavenumber, for the two cases discussed so far; such spectra are plotted in figure 2.4. The figure on the top is the classical spectrum which can be observed when α is not close to zero, with the three branches, classically denoted as A, P and S branch; this figure displays, in fact, all of the eigenvalues which exist when $h_{||}$ varies in the range $[0, 0.4]$. It is interesting to observe that the degenerate Squire modes of branch A (shown with red/grey bullets) split: such degenerate modes correspond, in the no-slip case, to a symmetric/antisymmetric couple of $\hat{u}$ eigenfunctions. When slip occurs on one wall, one of the two wall modes of the initially degenerate pair in branch A moves rapidly away from the $h_{||} = 0$ value, thus displaying a very strong sensitivity (in fact, also OS wall modes are highly sensitive). Despite this, the Squire eigenvalues, both the wall modes and the center modes, never cross the real axis in all cases considered here, and the mode which becomes unstable is the three-dimensional OS mode with c_r close to 0.2. The picture is radically different for the case of ridges at 45^o to the mean pressure gradient (bottom frame); as $h_{||}$ increases, the modes which are initially degenerate, all damped and concentrated along a single vertical line with $\omega_r \approx 0$ (for $h_{||} = 0$), separate and diverge from one another. The continuous line in the bottom frame joins all the least stable modes found for $h_{||} < 0.038$ and the unstable modes which emerge when $h_{||}$ exceeds 0.038.

The results obtained so far indicate that a new wall-vortex mode, driven by the presence of inclined wall ridges of sufficiently large amplitude, exists when Re is rather small, to presumably dominate the early stages of the transition process.

A parametric study, with θ and $h_{||}$ varied systematically to infer trends is reported in figures 2.5 and 2.6. The first of these figures show that the OS mode identifies the critical conditions only when θ is close to 0^o and 90^o; for θ in a range around 45^o (range which is wider with the increase of $h_{||}$) the wall-vortex mode is the dominating instability.

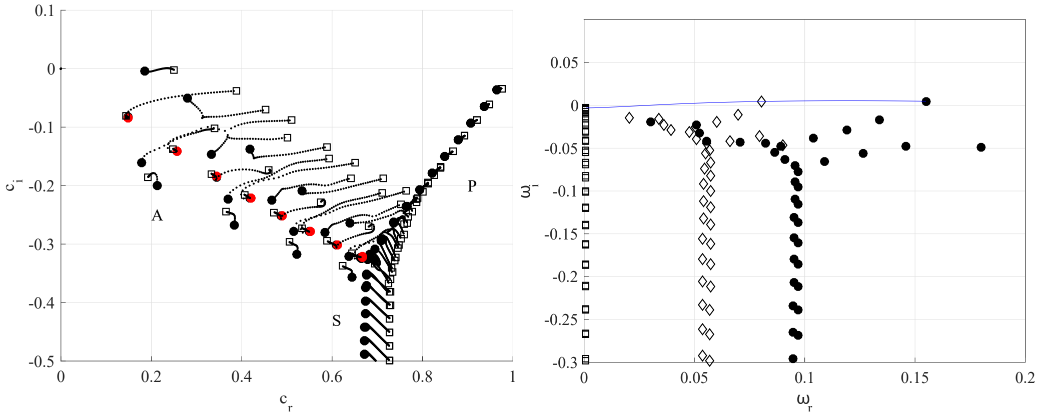

(a) (b)

Figure 2.4: (a) Spectra of the complex phase velocity c in the case of one SH wall at $Re = 10000$, $\theta = 80°$, $\Phi = 20°$ and $\alpha = 0.65$ and different values of $h_{||}$. The filled circles correspond to $h_{||} = 0$; in particular, the red/grey bullets show the Squire modes on branch A. The open squares represent the spectrum for $h_{||} = 0.4$ and the dots show the trajectory of each eigenmode when $h_{||}$ varies from 0 to 0.4. (b) Spectra of the complex frequency ω in the case of one SH wall when $Re = 2000$, $\theta = 45°$, $\Phi \approx 90°$ and $\alpha \approx 0$. The open squares, diamonds and filled circles show the spectra for $h_{||} = 0, 0.1, 0.2$, respectively. The continuous line traces the least stable mode for $h_{||}$ varying in the range $[0, 0.2]$.

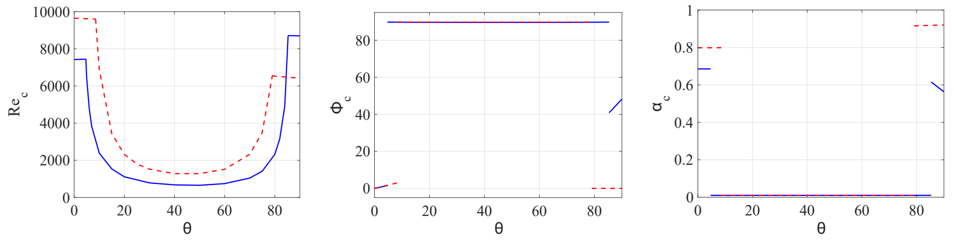

(a) (b) (c)

Figure 2.5: Critical Reynolds number Re_c (left), the corresponding wave angle (middle) and streamwise wavenumber (right) as a function of θ for the case of $h_{||} = 0.07$ (dashed line) and $h_{||} = 0.155$ (solid line) for one SH wall.

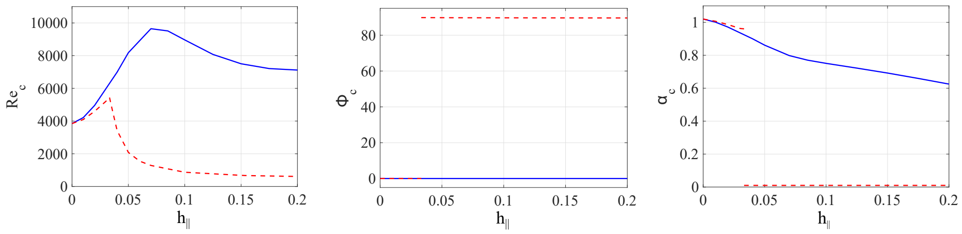

(a) (b)

Figure 2.6: Critical Reynolds number Re_c (left), the corresponding wave angle (middle) and corresponding streamwise wavenumber (right) as a function of $h_{||}$ for the case of $\theta = 0°$ (solid line) and $\theta = 45°$ (dashed line) in the presence of one SH wall.

The smallest critical Reynolds numbers, Re_c, are found at 45^o for both cases examined in figure 2.5 and are around a value of 1000, much smaller than the values of the corresponding neutral OS modes. The critical wave angle is 90^o in the range of θ's where this new instability dominates.

Figure 2.6 shows the behavior of the most unstable, two-dimensional OS mode (solid lines) which leads the instability when $\theta = 0°$, and the switch between the OS wave and the wall-vortex mode, when $\theta = 45°$, taking place at $h_{||} = 0.033$. As expected from previous studies, a stabilization effect (i.e. an increase of Re_c) is found for the OS mode as $h_{||}$ grows from zero ($Re_c = 3848$ for $h_{||} = 0$). However, when the ridges are at an angle of 45^o the OS mode is eventually overruled by the streamwise wall-vortex mode, which becomes unstable at progressively smaller values of the Reynolds number; for $h_{||}$ above around 0.15 an asymptotic value of the critical Re close to 600 is reached for the onset of the wall-vortex mode.

The case of two superhydrophobic walls is considered next, focussing on lower values of $h_{||}$ since it is known [Bottaro, 2014] that, when the walls are isotropic, a comparable stabilizing effect is achieved in the case of two SH walls for a value of the slip length ten times smaller than for a single SH wall. The results are summarized by figures 2.7 and 2.8. The notable effect in this case is that the streamwise wall-vortex mode does not emerge, with a competition which is now instaured between two-dimensional and three-dimensional OS modes; figure 2.7 shows that the onset of an exponential instability is delayed when $h_{||}$ is increased and that the two-dimensional OS wave (with $\Phi_c = 0$) dominates the transition process only for θ sufficiently large (the switch-over value increasing with $h_{||}$). The stabilizing effect of $h_{||}$ is confirmed by figure 2.8; for $h_{||}$ below 0.01 the stability characteristics are similar to those of the no-slip case, and two-dimensional OS modes prevail (for any value of θ). In the case of ridges inclined at an angle of 45^o to the mean streamwise velocity component, the mode which takes the lead past $h_{||} = 0.033$ is quasi-streamwise (α is small and decreasing).

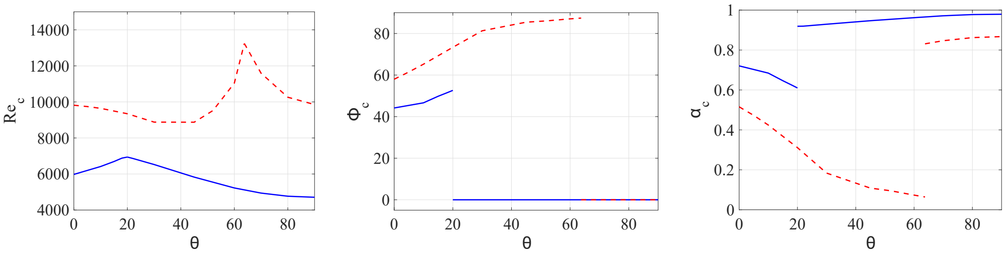

(a) (b) (c)

Figure 2.7: Critical Reynolds number Re_c (left) and corresponding wave angle (middle) and streamwise wavenumber (right) as a function of θ for the case of $h_{||} = 0.02$ (solid line) and $h_{||} = 0.05$ (dashed line) in the presence of two SH walls.

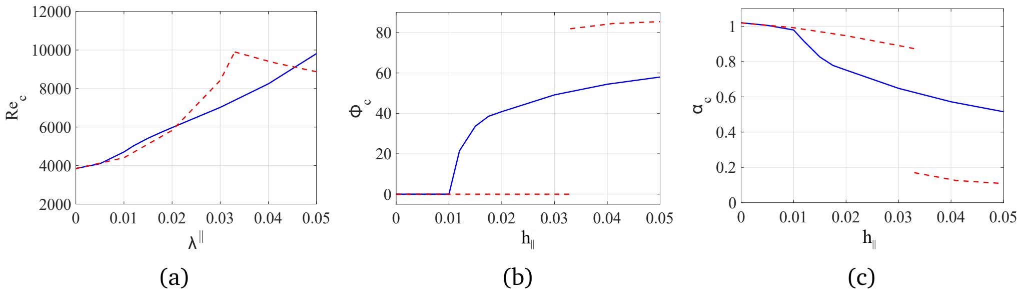

(a) (b) (c)

Figure 2.8: Critical Reynolds number Re_c (left) and corresponding wave angle (middle) and streamwise wavenumber (right) as a function of $h_{||}$ for the case of $\theta = 0°$ (solid line) and $\theta = 45°$ (dashed line) in the presence of two SH walls.

The spectrum of eigenvalues for a representative case is presented in the left part of figure 2.9 for $h_{||} = 0.05$, $\theta = 45°$ and $Re = 10000$. The classical branches, A, P and S, are present, with the unstable mode on the A branch. The shape of the unstable mode is found in the right frame of figure 2.9, where the shape of a (distorted) three-dimensional OS wave can be seen.

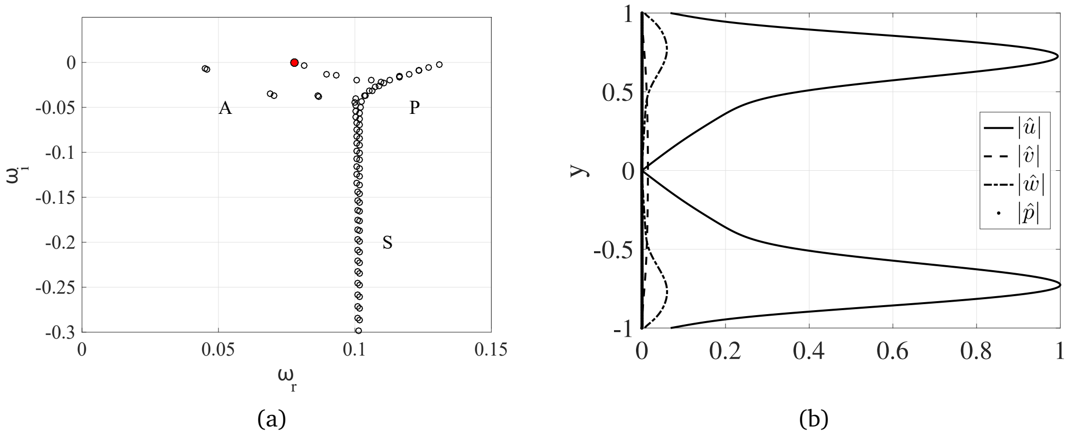

(a) (b)

Figure 2.9: Spectrum of temporal eigenvalues ω, with the unstable mode marked with a red/grey bullet (left), and absolute value of the disturbance velocity components (u, v, w) and disturbance pressure of the unstable mode (right), for $Re = 10000$, $h_{||} = 0.05$, $\theta = 45°$, $\alpha = 0.1$, $\Phi = 86°$ $(\beta = 1.4)$. Both walls are superhydrophobic.

2.5 Non-modal analysis

Figure 2.10 displays representative optimal perturbations (left column) for a given target time, for both no-slip and SH cases, together with their output fields (right column). The intermediate row (one slip wall at $y = -1$) is interesting since the initial disturbance field is more intense near the bottom wall than near the top one, and is oblique in the (y, z) plane.

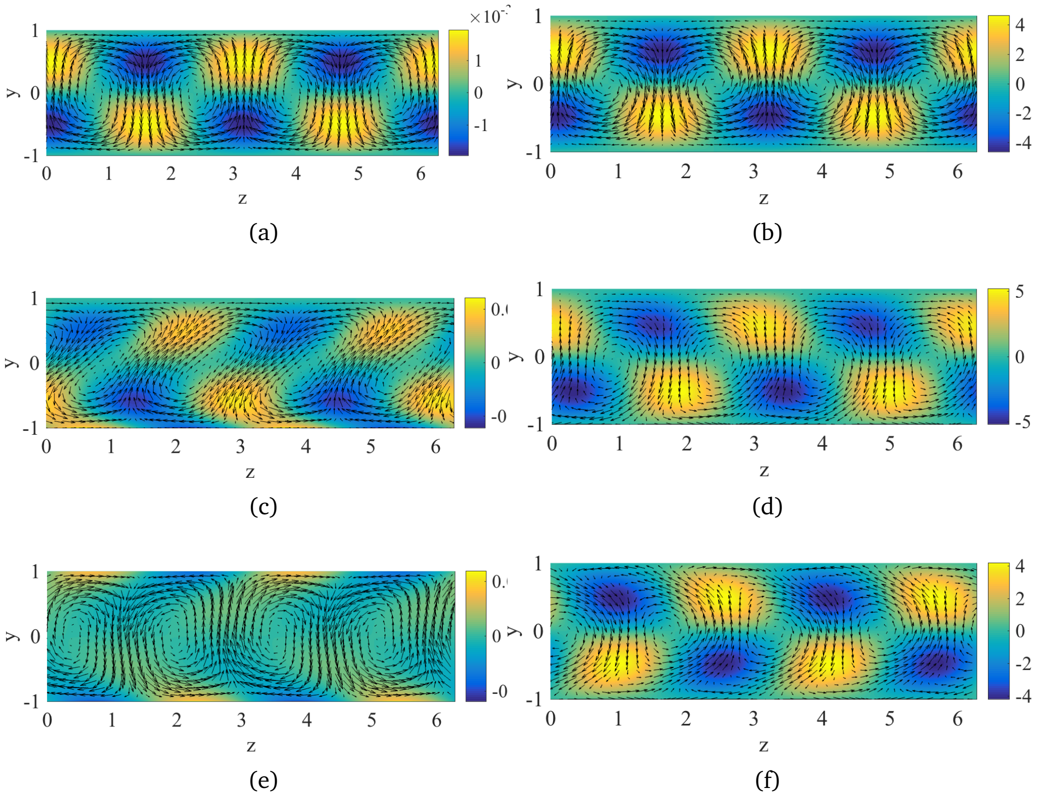

Figure 2.10: Vectors and contours, in the (y, z) plane, of the optimal disturbance at $t = 0$ (left column) and the ensuing solution at the target time $T = 105$ (right column), shown over two spanwise periods, for $h_{\parallel} = 0$ (top row), $h_{\parallel} = 0.05$ and one SH wall (middle row), $h_{\parallel} = 0.05$ and two SH walls (bottom row). The shaded contours represent the positive and negative streamwise disturbance velocity component, whereas the vectors represent wall-normal and spanwise components. The parameters are $Re = 1333$, $\beta = 2$, $\alpha \approx 0$, $\theta = 30°$.

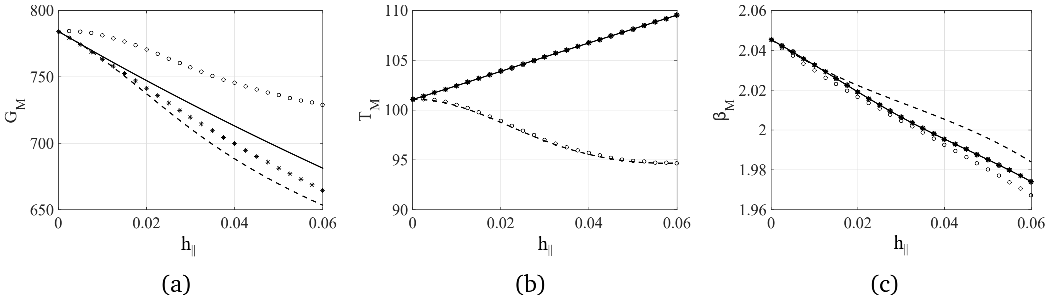

Figure 2.11: Gain G_M (left), corresponding time T_M (middle) and spanwise wavenumber β_M (right) as a function of $h_{\parallel}$ in the case of $\theta = 0°$ (–), $\theta = 15°$ ($*$), $\theta = 30°$ (– –), $\theta = 60°$ ($\circ$), for $Re = 1333$ and two SH walls. In all cases the corresponding optimal streamwise wavenumber is $\alpha_M \approx 0$.

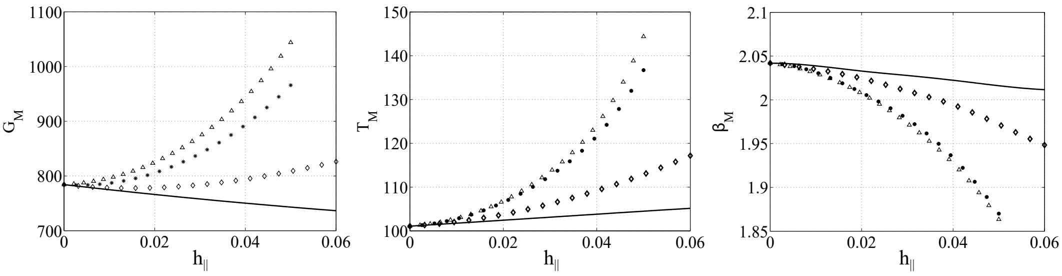

(a) (b) (c)

Figure 2.12: Gain G_M (left), corresponding time T_M (middle) and spanwise wavenumber β_M (right) as a function of $h_{\|}$ in the case of $\theta = 0°$ $(-)$, $\theta = 15°$ (d$iamond$), $\theta = 30°$ $(*)$, $\theta = 60°$ (d$elta$). In all cases $Re = 1333$, $\alpha_M \approx 0$ and only one wall is superhydrophobic.

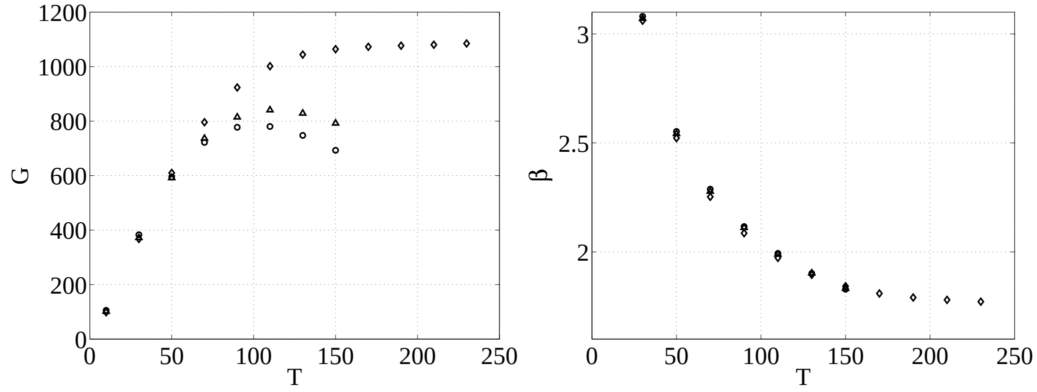

(a) (b)

Figure 2.13: Gain G (left) and corresponding optimal spanwise wavenumber β (right) as a function of the final time T, for the case of $h_{\|} = 0$ ($\circ$), $h_{\|} = 0.03$ (d$elta$), $h_{\|} = 0.06$ (d$iamond$), $\theta = 30°$, $\alpha \approx 0$ and $Re = 1333$.

The maximum gain G_M of a disturbance over a given time, maximized with respect to the wavevector, depends parametrically on $Re, h_{\|}$ and θ. The results shown in figures 2.11 through 2.13 are computed for a fixed value of $Re = 1333$, which is the same used by Min and Kim [2005] (they scaled Re with the centerline velocity which is why they quote a value of 2000). This Reynolds number is subcritical from a modal analysis point of view in the no-slip case.

In figure 2.11 G_M is given as a function of $h_{\|}$ for different values of θ, in the case of two SH walls. For $h_{\|} = 0$ we recover the no-slip case and for $h_{\|} > 0$ there is a monotonic decrease of the gain for all θ's. In all cases the corresponding $\alpha_M \approx 0$ and the variation of both β_M and T_M with the slip length is weak. In the case of a single SH wall the results show a different trend, as demonstrated in figure 2.12. Again, the gain G_M is presented as a function of $h_{\|}$ for different values of θ. For values of the ridge angle larger than zero the gain always increases as the Navier slip length is increased. Moreover, for some values of the ridge angle θ, and above a threshold $h_{\|}$, the flow becomes unstable from a modal point of view: in these cases no finite value of T_M is found, since the gain increases monotonically with the increase of the final target time. An example is presented in figure 2.13 where the gain G is plotted as a function of the final time T of the optimization and three different values of $h_{||}$ for the case in which $\theta = 30°$. For $h_{||} = 0$ and 0.03 the gain decreases for large enough values of T; conversely, when $h_{||} = 0.06$ the gain increases, albeit slowly, with T, with the spanwise wavenumber β reaching an asymptotic value equal to 1.78. The unbounded increase of G with T is the indication of the occurrence of the streamwise wall-vortex exponential instability.

2.6 Summarizing remarks

The modal behavior has yielded surprising results in two senses: on the one hand, a new streamwise wall-vortex mode has been found in the case of a single SH wall, driven by the wall boundary condition, and capable to reduce significantly the value of the Reynolds number for the onset of the instability. This new mode is enhanced by the increase of $h_{||}$ and is found to be most effective when the ridges are inclined by an angle of about $45°$ to the mean pressure gradient. On the other hand, when two walls are superhydrophobic, the instability is ruled by either a two-dimensional or a three-dimensional Orr-Sommerfeld mode, as function of θ and $h_{||}$, demonstrating *a posteriori* the inapplicability of Squires theorem for this flow.

The non-modal analysis shows that while the presence of two SH walls yields a slight reduction in energy growth over time, the case of only one SH wall produces an increase of the disturbance kinetic energy for a large range of values of $h_{||}$ when θ is sufficiently greater than zero. It is further shown that, for a single SH wall, beyond a threshold slip length, for values of the inclination angle of the micro-ridges around $45°$ the gain becomes unbounded with the final target time, a sign of the onset of the wall-vortex instability.

2.6.1 When is the Navier slip condition applicable?

The boundary conditions (2.2) and (2.3) used throughout the present analysis for both the base flow, and the perturbations are based on a linearization in the parameters $h_{||}$ and $h_{\perp}$. Inevitably, when the values of $h_{||}$ and $h_{\perp}$ increase the excluded higher order terms are no longer negligible. For applications of the presented method it would be useful to have an estimate of the values of the slip lengths below which we can have some confidence that the Navier slip condition applies.

The error committed by the imposed boundary condition can be evaluated in a manner which has been suggested to us by Paolo Luchini: Let's imagine that we displace the lower wall a distance h in the vertical direction, from $y = -1$ to $y = -1 + h$ and thus to have slip at the position $y = -1 + h$. The linearized boundary

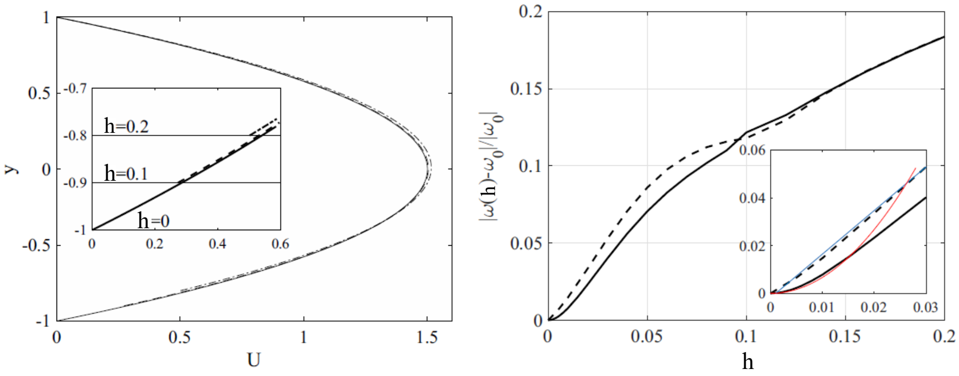

Figure 2.14: (Left) Base flow when $h = 0, 0.1, 0.2$; the inset shows a close-up of the lower boundary for three values of $h_{||}$. (Right) Modulus of the difference between the complex frequency ω, for different values of $h_{||}$, and the value of ω when $h_{||} = 0$. Here $h_{||} = h_{\perp}$ (solid line), $h_{||} = 2h_{\perp}$ (dashed line), $Re = 10000$ and $\alpha = \beta = \frac{1}{\sqrt{2}}$. A linear (blue) and a quadratic (red) functions have been superposed to the results of the two cases to emphasize the behaviors when $h_{||}$ is small (thin lines in the inset).

condition (here for the mean flow, but later in the same form also for the perturbation velocity components) at order one is

$$U(-1+h) = h\frac{dU}{dy}(-1+h), \tag{2.31}$$

found by assuming no-slip at $y = -1$. The analytical solution of the base flow is simply

$$U(y) = \frac{6}{4-3h^2}\left[1 - y^2 - \frac{1}{2}h^2(1-y)\right] \tag{2.32}$$

where we have set $\theta = 0$, for simplicity, which means that $W = 0$. The linearization yields a small nonzero velocity at the lower boundary, $U(-1) = \frac{-6h^2}{(4-3h^2)}$, indicating that the error committed on the mean flow by using equation 2.31 is of order h^2. Examples of the base flow profiles are plotted in figure 2.14 (left frame) for three values of h, demonstrating that small differences appear and increase with the slip length.

The errors in the stability analysis can be evaluated by comparing the complex eigenvalue ω evaluated for different slip lengths against the case for which $h_{||} = h_{\perp} = 0$; a measure of such errors is $\frac{\omega(h) - \omega(h=0)|}{|\omega_0|}|$, with ω_0 the complex angular frequency in equation 2.31 computed for $h = 0$.

Two cases are considered next: one is the case of isotropic roughness, i.e., $h_{||} = h_{\perp} = h$, and the second is the case of longitudinal ridges, for which $h_{||} = 2h_{\perp} = h$. These two cases are expected to yield different behaviors, particularly at low h, in view of the fact that the only relevant protrusion length scale is the difference between $h_{||}$ and $h_{\perp}$. This occurs, as explained by Luchini et al. [1991], since any physically significant parameter must be independent of the choice of the origin of the wall (which we might for convenience place at the tip of the roughness elements).

Thus, it is d$eltah = h_{||} - h_{\perp}$ which provides a quantitative measure of the effect of roughness on the boundary layer stability behavior; in the case of isotropic roughness d$eltah = 0$, and the effect must thus be of second order in h, i.e., the curve of the error must be initially parabolic. Conversely, for longitudinal ridges it is d$eltah = \frac{h_{||}}{2}$, and the error in the eigenvalue should scale linearly with h. This is confirmed by our stability calculations (figure 2.14, right frame), carried out at $Re = 10000$ for a disturbance of wavenumber $k = 1$ inclined by 45° to the x axis, for values of h up to 0.2. Other inclinations of the perturbation wave yield similar results, confirming the conclusions: in the case of ridges, the linear deviations from the exact solution can be expected to hold until $h \approx 0.05$, whereas the error remains approximately quadratic with h in the case of cylindrical, regularly spaced posts, only until $h \approx 0.02$. The percentage error in ω remains below 10% for h up to about 0.1; such a value of the protrusion height could thus be taken as an upper bound, beyond which the Navier slip condition becomes untenable. Some results in the paper obtained for values of h larger than the threshold above should be considered only as illustrative.

A final note concerns the boundary condition for the normal-to-the wall velocity. Because of continuity, the homogenized boundary condition for $\hat{v}$ is simply $\hat{v} = 0$. However, for superhydrophobic walls, with an underformable gas plastron which completely fills the microcavities, it is clearly correct to impose no penetration of the fluid at the tip of the roughness elements, a question might remain when the wetted state is reached: should a protrusion height be defined also for the vertical velocity component? The answer in the case of microridges is no [Luchini, 2013], since the solution of the near-wall Stokes problem has only two degrees of freedom, i.e., only two protrusion heights can be defined. Thus, the vanishing of the normal velocity at a given y position rather than another one has only a second order effect on the result, comparable to the error which is made anyway.

Chapter 3

The microscopic problem

3.1 Problem formulation

The velocity profile in the boundary layer generated by a turbulent flow along a locally plane surface has been extensively studied from both numerical and experimental point of view, leading to an in-depth knowledge of the phenomena taking place in this thin, but important region. It is common practice to subdivide the turbulent boundary layer into different zones, depending on the value of the wall normal coordinate in wall units:

- viscous sublayer: very thin region extending until $y^+ \approx 5$, where the viscous forces are dominant with respect to the inertial ones. If y is the wall normal coordinate, $y^+ = \dfrac{u_\tau y}{\nu}$, with $u_\tau = \sqrt{\dfrac{\tau_w}{\rho}}$ the friction velocity, and τ_w the wall shear stress. Here the conversion of convected momentum into viscous stress is negligible, thus the flow is governed mainly by the balance of viscous stresses. The velocity profile is linear with respect to the wall normal coordinate y^+;

- buffer layer: it is found between the viscous sublayer and the log-law region and no analytical laws are defined there. The viscous and inertial forces are of the same order and, in the middle of this region, the peak production and dissipation of the turbulent energy is know to occur.

- log-law region: it is located far from the wall ($y^+ > 30$), where the velocity profile exhibits a logarithmic behaviour of the type

  $$u^+ = \frac{1}{k}\log(y^+) + A, \tag{3.1}$$

  where $k \approx 0.4$ is the Von Karman's constant, considered universal (at least for moderate to high Reynolds number flows) and $A \approx 5$ for the classical case of flat plate boundary layer with zero pressure gradient.

Our aim is to understand how a micro-corrugated wall, with gas/oil cavities within, affects the viscous sublayer, in both the directions parallel and normal to the corrugations. Since in this region the convective terms are negligible, the momentum equation reduces to the Stokes form

$$\nabla p = \mu \nabla^2 \boldsymbol{u}, \quad \nabla \cdot \boldsymbol{u} = 0. \tag{3.2}$$

The starting point consists in recognizing that two problems exist, an inner problem ruled by microscopic variables and an outer, macroscopic problem for which the bounding surface is smooth (and can be taken to coincide with the tips of the ribleted surface). The boundary behaviour of the outer solution requires there to be a wall slip velocity, U_s, and a wall shear rate, $\kappa_w = \frac{\partial U}{\partial y}|_{y=0}$. In dimensionless terms, an outer wall-normal variable, Y, can be defined, related to the corresponding inner variable $\tilde{y}$ by

$$Y = \epsilon \tilde{y};$$

$\epsilon = b/L$ is a small parameter (with b the microscopic length scale and L the macroscale characterizing outer flow phenomena). The inner scales used to normalize the dimensional Stokes equations and the boundary conditions are b as length scale (see figure 3.1), $b\,\kappa_w$ as velocity scale and $\mu\,\kappa_w$ as pressure scale. The shear rate is imposed by the outer solution onto the inner one so that, when the outer variable $Y \to 0$, the dimensional streamwise component of the velocity tends to $U_s + \kappa_w L Y$ (the spanwise component also behaves linearly in Y, by an analogous reasoning). Observe that when $Y \to 0$ we have $\tilde{y} \to \infty$ and, in inner variables scalings, the streamwise velocity component $\tilde{u}$, in dimensionless form, tends to $\frac{U_s}{b\,\kappa_w} + \tilde{y}$, i.e.

$$\frac{\partial \tilde{u}}{\partial \tilde{y}}|_{y \to \infty} \to 1.$$

Adopting the above normalization, the governing equations (Stokes plus continuity) read:

$$\nabla p = \nabla^2 \boldsymbol{u}, \quad \nabla \cdot \boldsymbol{u} = 0, \tag{3.3}$$

note that there should be no ambiguity on the fact that, from now on, everything is non-dimensional, although tildes have been removed from the variables' names.

In principle, the above is a three-dimensional system; however, it might be decoupled into two separate two-dimensional problems when corrugations homogeneous along the streamwise directions are considered. In order to apply this geometric constraint, we have to assume that the interface between the two fluids is allowed to deform only under the effect of the transverse flow, remaining homogeneous along the longitudinal direction. If this hypothesis is satisfied, the initial Stokes problem is split into two different parts, known as transverse and longitudinal problems, whose governing equations together with the appropriate boundary conditions are reported in figure 3.1. In particular, the Laplace equation is found to govern the longitudinal flow, while the two dimensional Stokes equation holds for the transverse and wall normal components of the velocity.

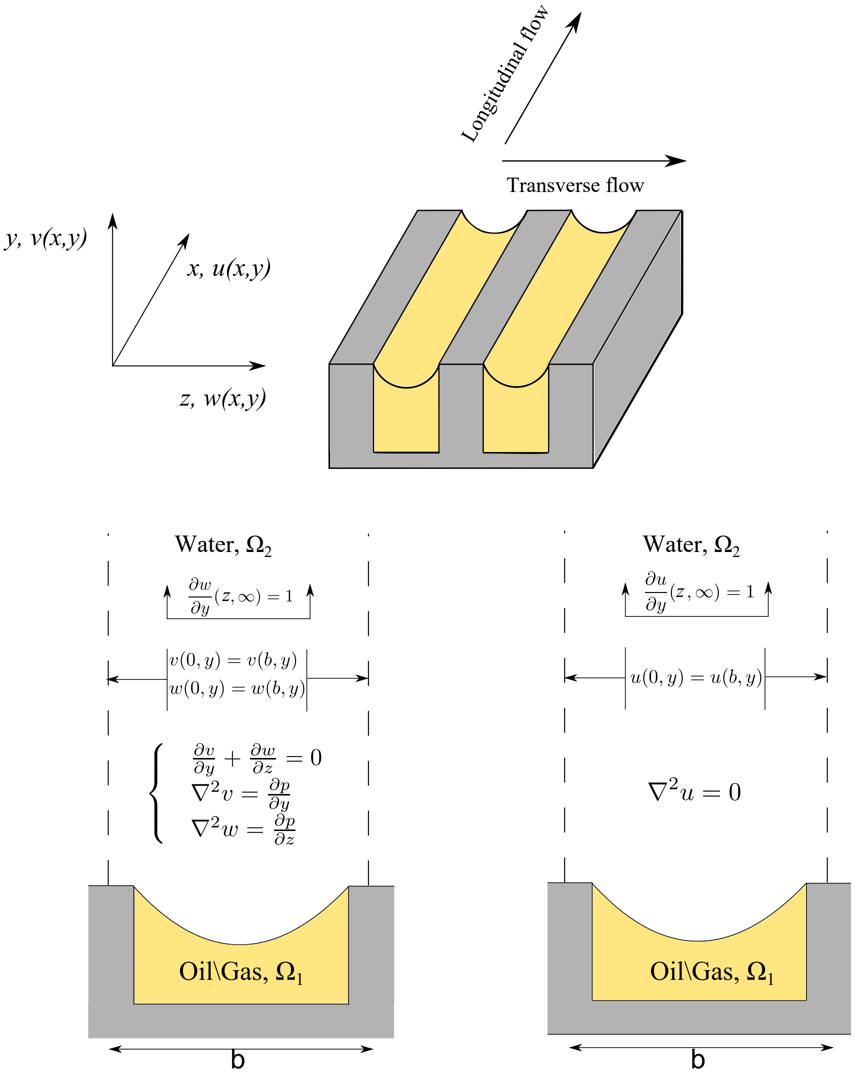

Figure 3.1: Geometry, governing equations and boundary conditions for the transverse (bottom left) and the longitudinal (bottom right) problems.

3.1.1 The definition of protrusion heights

The linearity of the Laplace and the Stokes equations allows to perform some important analytical considerations on the behaviour of the longitudinal and transverse velocity components. The problem of the longitudinal flow over a grooved surface has been studied by Bechert and Bartenwerfer [1989] who found a solution in terms of Fourier series of the form:

$$\begin{cases} u = \sum_{n=-\infty}^{+\infty} \tilde{u}_n e^{inz}, \\ \tilde{u}_0 = a_0 + b_0 y, \\ \tilde{u}_n = a_n e^{-|n|y} + b_n e^{|n|y}, \quad n \neq 0. \end{cases} \tag{3.4}$$

Applying the condition $\dfrac{\partial u}{\partial y} \to 1$, it is easy to show that $b_0 = 1, b_n = 0$, and the unknown coefficients a_n are determined from the condition at the wall surface. If the wall surface is smooth and with a standard no-slip condition, the longitudinal velocity profile is readily calculated as

$$u(y) = \left(\frac{\partial u}{\partial y}\right) y, \tag{3.5}$$

which is a simple linear profile. If the surface has a general shape, the expression of the coefficients a_n cannot be expressed explicitly and have to be calculated case by case. However, it can be noted that, since all the coefficients $\tilde{u}_n$ vanishes as soon as $y \to +\infty$, the asymptotic behaviour of the longitudinal velocity component takes the simple form

$$u = y + a_0, \tag{3.6}$$

which represents a linear profile shifted in the wall normal direction by the quantity a_0. Usually, a_0 depends on the shape of the wall and it is called parallel protrusion height or Navier slip length and indicated with $h_{||}$.

A similar discussion can be conducted for the transverse flow [Luchini et al., 1991]. In order to obtain a more suitable form, we introduce the stream function ψ and recast the Stokes equation as

$$\nabla^4 \psi = 0. \tag{3.7}$$

The solution of the biharmonic equation satisfying periodic boundary condition along the spanwise direction reads

$$\begin{cases} \psi = \sum_{n=-\infty}^{+\infty} \tilde{\psi}_n e^{inz}, \\ \tilde{\psi}_0 = a_0 + b_0 y + c_0 y^2 + d_0 y^3, \\ \tilde{\psi}_n = (a_n + b_n) e^{-|n|y} + (c_n + d_n) e^{|n|y}, \quad n \neq 0, \end{cases} \tag{3.8}$$

which assumes a form quite similar to equation (3.4). Due to the fixed gradient of the spanwise velocity far from the protrusion (i.e $\frac{\partial^2 \psi}{\partial y^2} = 1$), we obtain that $c_0 = \frac{1}{2}$ and $d_0 = c_n = d_n = 0$, while the remaining coefficient are again to be determined by applying the prescribed boundary condition at the wall. Proceeding in a similar way to the longitudinal problem, we consider the asymptotic behavior of the solution, obtaining

$$\psi = a_0 + b_0 y + \frac{1}{2} y^2, \tag{3.9}$$

thus

$$w = y + b_0. \tag{3.10}$$

In this case the constant b_0 is called transverse protrusion height (here it is $h_\perp$), since it is related to the transverse problem. As sketched in figure 3.2, the protrusion heights represent the two virtual distances below a reference surface at which the velocity profiles would extrapolate to zero. We may remark, however, that any origin of the y-axis can be set to measure these quantities. It is evident that any physically significant parameter must be independent of the choice of the origin: the only combination of the two protrusion heights that has this property is their difference $\Delta h = h_{||} - h_{\perp}$. The concept of protrusion height becomes relevant in order to quantitatively measure the effect of a particular wall on the viscous sublayer and the value of Δh expresses how much the actual wall pattern impedes the cross-flow more than it does the longitudinal flow [Luchini et al., 1991].

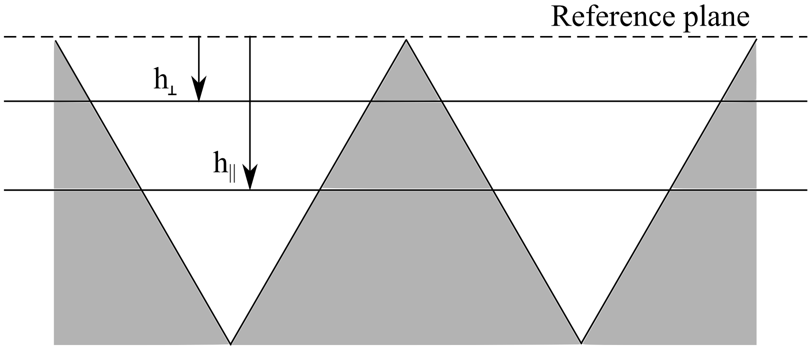

Figure 3.2: Definition of the protrusion heights with respect to a reference plane.

3.2 The boundary integral method

The boundary integral method (BIM) is a powerful mathematical technique that allows to recast an original differential problem into an integral one. In theory, there are no restrictions on the type of the differential problem suitable for this transformation; however, the BIM is mostly applied to linear, elliptic, and homogeneous partial differential equations governing boundary-value problems in the absence of a homogeneous source. The method covers a wide range of applications, spanning from solid mechanics to electrostatics and from noise propagation to fluid mechanics. The key idea of this method is to express the solution in terms of boundary distributions of fundamental solutions of the differential equation considered. The fundamental solutions are Green's functions expressing the field due to a localized source and the densities of the distributions are then computed to satisfy the specified boundary conditions. Since in the present dissertation, the equations involved are the Laplace equation, governing the longitudinal problem, and the Stokes equation, governing the transverse problem, the BIM finds an effective applicability.

In the following the basic derivation of the boundary integral equations (BIE) for both the Laplace and Stokes equation for a single phase flow is offered. The result is of fundamental importance since highlights the main procedure to recast a differential problem into an integral form. Moreover, the single phase BIE will be used as starting point to extended the theory to the case of two phase flows.

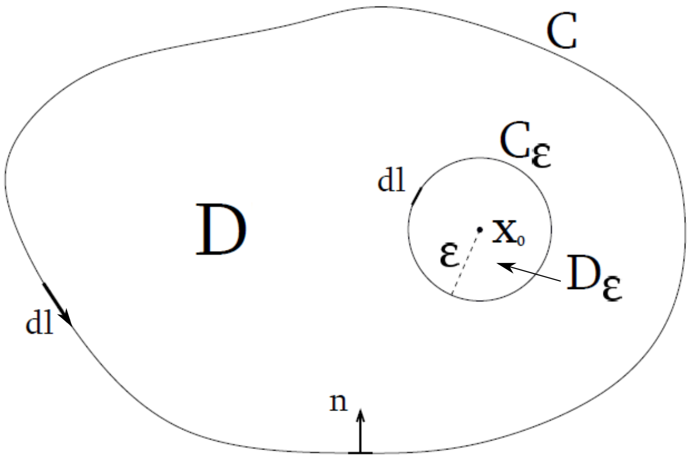

Figure 3.3: Sketch of the domain used for the derivation of the boundary integral equations.

3.2.1 BIM for the Laplace equation in two dimensions

Let us consider a closed domain D, with contour C and normal $\boldsymbol{n}$, as sketched in figure 3.3. The Laplace equation holds in D for an unknown scalar function u and reads

$$\nabla^2 u = 0. \tag{3.11}$$

In order to transform the Laplace equation into an integral form, we exploit Green's second identity

$$G\nabla^2 u - u\nabla^2 G = \nabla \cdot (G\nabla u - u\nabla G), \tag{3.12}$$

where G is known as Green's function, satisfying by definition the singularity forced Laplace equation

$$\nabla^2 G(\mathbf{x}, \mathbf{x_0}) + \delta(\mathbf{x} - \mathbf{x_0}) = 0, \tag{3.13}$$

with $\boldsymbol{x}_0$ a specific point into the domain, called field point. The simplest choice for G is the free space Green's function, corresponding to the solution of equation (3.13) in unbounded space:

$$G = \frac{1}{2\pi} \log(r), \quad r = \sqrt{(x - x_0)^2 + (y - y_0)^2} \tag{3.14}$$

The Green's function usually presents a singularity at $\mathbf{x} = \mathbf{x}_0$, thus it is convenient to integrate the Green's second identity (3.12) over the reduced domain $D' = D - D_\epsilon$ (see figure 3.3), obtaining:

$$\iint_{D'} (G\nabla^2 u - u\nabla^2 G) dS = \iint_{D'} \nabla \cdot (G\nabla u - u\nabla G) dS, \tag{3.15}$$

where the left-hand side of equation (3.15) is equal to zero, since $\nabla^2 u = 0$ and $\nabla^2 G = 0$, when $\mathbf{x} \neq \mathbf{x}_0$. Next, applying the divergence theorem to the left-hand side of equation (3.15) we obtain

$$\int_{C+C_\epsilon} (G\nabla u - u\nabla G) \cdot \mathbf{n}\, dl = 0, \tag{3.16}$$

where C is the boundary of D, C_ϵ is the boundary of D_ϵ, and l measures arc length along either C or C_ϵ.

We now consider the limit for $\epsilon \to 0$ of the integral around C_ϵ and we recall that, since C_ϵ is a circumference, r can be substituted with ϵ. Since $\epsilon \to 0$ the small surface portion $D_\epsilon \to 0$ and thus $u(\boldsymbol{x}) \to u(\boldsymbol{x}_0)$ leading to

$$\lim_{\epsilon\to 0} I_\epsilon = \lim_{\epsilon\to 0} \left[\frac{1}{2\pi} \log(\epsilon) \frac{\partial u(\boldsymbol{x}_0)}{\partial r} \int_{C_\epsilon} dl - \frac{u(\boldsymbol{x}_0)}{2\pi\epsilon} \int_{C_\epsilon} dl \right] = \\ \frac{1}{2\pi} \log(\epsilon) \frac{\partial u(\boldsymbol{x}_0)}{\partial r} 2\pi\epsilon - u(\boldsymbol{x}_0) \frac{1}{2\pi\epsilon} 2\pi\epsilon = -u(\boldsymbol{x}_0). \tag{3.17}$$

Substituting back the result of the limit (3.17) into the relation (3.16), we obtain the following important identity

$$u(\mathbf{x_0}) = \int_C u(\mathbf{x})\mathbf{n} \cdot \nabla G(\mathbf{x}, \boldsymbol{x}_0)\, dl - \int_C G(\mathbf{x}, \boldsymbol{x}_0)\mathbf{n} \cdot \nabla u(\mathbf{x})\, dl. \tag{3.18}$$

Equation (3.18) establishes a relationship between the unknown function u in an arbitrary point within the domain D and two integral operators involving the boundary values of u or ∇u. The first integral on the right-hand side is called double-layer potential (DLP), while the second one is called single-layer potential (SLP). These operators represent a continuous distribution of sources or dipoles along the domain's boundary and they are the building blocks of the boundary integral method.

To complete the derivation of the boundary integral equation, we let the point $\boldsymbol{x}_0$ lay on the domain's contour C such that all the quantities in equation (3.18) involve the unknown function or its gradient only at the boundary. In proceeding with this operation, some care is needed when the limit for $\boldsymbol{x}_0 \to C$ is considered. It can be demonstrated [Pozrikidis, 1992] that the single-layer potential is continuous through the boundary C, while the double-layer potential undergoes a jump discontinuity of the type:

$$\lim_{\boldsymbol{x}_0 \to C} \int_C u(\mathbf{x})\mathbf{n} \cdot \nabla G(\mathbf{x}, \boldsymbol{x}_0)\, dl = \int_C^{PV} u(\mathbf{x})\mathbf{n} \cdot \nabla G(\mathbf{x}, \boldsymbol{x}_0)\, dl \pm \frac{1}{2}, \tag{3.19}$$

where the plus sign is to taken when the limit is done starting from a point within the domain D, whereas the minus sign holds if the limit is done from a point defined in the exterior of the domain. The upper-script PV denotes that the integral is to be intended in the sense of its principal value. Keeping this in mind and performing the limit of equation (3.15) for a point $\boldsymbol{x}_0$ defined either inside or outside D (in this case the velocity $u(\boldsymbol{x}_0) = 0$ in equation 3.18), the following result is obtained

$$\frac{1}{2}u(\mathbf{x_0}) = \int_C^{PV} u(\mathbf{x})\mathbf{n}\cdot\nabla G(\mathbf{x},\mathbf{x_0})\,dl - \int_C G(\mathbf{x},\mathbf{x_0})\mathbf{n}\cdot\nabla u(\mathbf{x})\,dl \tag{3.20}$$

Equation (3.20) is known as the boundary integral equation for the Laplace equation and allows to solve for the unknown function u or ∇u at the boundary, as function of the boundary conditions. Once the boundary quantities are know, the field inside D can be reconstructed using the relation (3.18).

3.2.2 BIM for the Stokes equation in two dimensions

Just like the Laplace equation, the Stokes equation can be recast into integral form. The starting point is the Lorenz reciprocal identity [Pozrikidis, 1992], which relate two arbitrary flows $\boldsymbol{u}$ and $\boldsymbol{u}^{'}$ together with their associated stress tensors $\boldsymbol{\sigma}$ and $\boldsymbol{\sigma}^{'}$ as

$$\frac{\partial}{\partial x_j}\left(u_i'\sigma_{ij} - u_i\sigma_{ij}'\right) = 0. \tag{3.21}$$

Identifying $\boldsymbol{u}^{'}$ with the flow generated by a point source of constant and arbitrary strength $\boldsymbol{b}$, located in $\boldsymbol{x}_0$ (see again figure 3.3), we obtain

$$u_i'(\mathbf{x}) = \frac{1}{4\pi\mu}G_{ij}(\mathbf{x},\boldsymbol{x}_0)b_j, \tag{3.22}$$

$$\sigma_{ij}'(\mathbf{x}) = \frac{1}{4\pi\mu}T_{ijk}(\mathbf{x},\boldsymbol{x}_0)b_j, \tag{3.23}$$

where, similarly to the Laplace equation, G_{ij} is the Green's function and T_{ijk} is its associated stress tensor. The Green's function is a tensor of rank 2, since the Stokes equation has two components. Similarly to the previous case, the simplest choice for G_{ij} is to select the solution of the singularly forced Stokes equation in the free space, which is also known with the name of Stokeslet:

$$G_{ij} = \delta_{ij}\log r + \frac{\hat{x}_i\hat{x}_j}{r^2} \tag{3.24}$$

$$T_{ijk} = -4\frac{\hat{x}_i\hat{x}_j\hat{x}_k}{r^4}, \tag{3.25}$$

with r the euclidean distance in the Cartesian plane and $\hat{\boldsymbol{x}} = \boldsymbol{x} - \boldsymbol{x}_0$. In order to obtain an integral representation of Stokes equation, we first substitute the relations (3.22) for $\boldsymbol{u}^{'}$ and $\boldsymbol{\sigma}^{'}$ into the Lorenz identity (3.21), then we integrate over the result over the reducted domain $D - D_\epsilon$ and apply Green's divergence theorem, obtaining

$$\iint_{C+C_\epsilon} G_{ij}\sigma_{ik} - \mu u_i T_{ijk} n_k dl = 0 \tag{3.26}$$

Again, since the Stokeslet is singular at $\boldsymbol{x} = \boldsymbol{x}_0$, the strategy consists in removing the singularity from D and adding it back later through a limit operation on D_ϵ. After the above manipulations, the right hand side of expression (3.26) is split into two contributions involving the line integral along the external domain's contour and the line integral along the contour of a small circular region D_ϵ of radius ϵ, defined around $\boldsymbol{x}_0$. The results of this manipulations leads to

$$\iint_C G_{ij}\sigma_{ik}n_k - \mu u_i T_{ijk} n_k \, dl = - \iint_{C_\epsilon} G_{ij}\sigma_{ik}n_k - \mu u_i T_{ijk} n_k \, dl. \tag{3.27}$$

Letting $\epsilon \to 0$, we find that over C_ϵ, to leading order in ϵ, the tensors $\boldsymbol{G}$ and $\boldsymbol{T}$ on the right hand side reduce to the Stokeslet and it associated stress tensor (3.24) . Substituting their expressions in the integral relation (3.27) and noting that along C_ϵ the euclidean distance r is equal to the circle's radius ϵ, we have

$$\lim_{\epsilon \to 0} \left[\int_{C_\epsilon} \left(\delta_{ij} \epsilon \mathrm{log} \epsilon + \frac{\hat{x}_i \hat{x}_j}{\epsilon} \right) \sigma_{ik} n_k \, d\theta + \int_{C_\epsilon} 4\mu u_i \frac{\hat{x}_i \hat{x}_j}{\epsilon^3} \hat{x}_k n_k \, d\theta \right], \tag{3.28}$$

where the differential dl has been conveniently expressed in polar coordinates as $dl = r d\theta = \epsilon d\theta$ and the normal $\boldsymbol{n} = \frac{\hat{\boldsymbol{x}}}{\epsilon}$.

Consider now the first term of the limit (3.28)

$$\int_{C_\epsilon} \left(\delta_{ij} \epsilon \mathrm{log} \epsilon + \frac{\hat{x}_i \hat{x}_j}{\epsilon} \right) \sigma_{ik} n_k \, d\theta, \tag{3.29}$$

as $\epsilon \to 0$, $\boldsymbol{x} \to \boldsymbol{x}_0$ and $\sigma_{ik}(\boldsymbol{x}) \to \sigma_{ik}(\boldsymbol{x}_0)$. Also $\dfrac{\hat{x}_i \hat{x}_j}{\epsilon} \sim \epsilon \to 0$, so the whole of the first term vanishes in the limit of $\epsilon \to 0$.

For the second term, since $\hat{x}_k n_k = \dfrac{|\boldsymbol{x}|^2}{\epsilon} = \epsilon$ and $\lim\limits_{\epsilon \to 0} u_i(\boldsymbol{x}) = u_i(\boldsymbol{x}_0)$, we have

$$4\mu u_i(\boldsymbol{x}_0) \int_{C_\epsilon} \frac{\hat{x}_i \hat{x}_j}{\epsilon^2} \, d\theta = 4\pi\mu u_j(\boldsymbol{x}_0), \quad \text{with} \quad \int_0^{2\pi} \frac{\hat{x}_i \hat{x}_j}{\epsilon^2} \, d\theta = \pi \delta_{ij} \tag{3.30}$$

Finally, substituting the result (3.30) into equation (3.27), we obtain the desired boundary integral equation of the Stokes flow

$$4\pi\mu u_j(\mathbf{x_0}) = \mu \int_C u_i(\mathbf{x}) T_{ijk}(\mathbf{x}, \mathbf{x_0}) n_k dl - \int_C G_{ij}(\mathbf{x}, \mathbf{x_0}) \sigma_{ik}(\mathbf{x}) n_k dl. \tag{3.31}$$

3.3 Boundary integral method for two phase flows

The boundary integral method is often used to describe physical problems in multiple domains, connected to each other. This is the case of multiphase flows, where immiscible fluids with different physical properties are in contact and separated by a deformable interface. The strategy to derive the BIE for this kind of problems is to write down the integral representation for the unknowns involved in each domain and then couple them together using proper boundary conditions at the interface. Our problem is a typical situation where the BIM finds an efficient application. We refer to figure 3.4, which represents the simplest type of SHS/LIS consisting of rectangular grooves elongated along the streamwise direction and regularly spaced along the spanwise direction. The exactly same procedure applies to different wall pattern, provided that the fundamentals hypothesis guaranteeing the decoupling of the problem are respected. We will consider the flow in a two-dimensional domain filled with two viscous fluids of viscosity ratio $\lambda = \frac{\mu_1}{\mu_2}$; fluid 1 is found in domain Ω_1, while fluid 2 is contained within Ω_2. The two domains are separated by the interface, I, of unit normal $\boldsymbol{n}$ when seen from Ω_1.

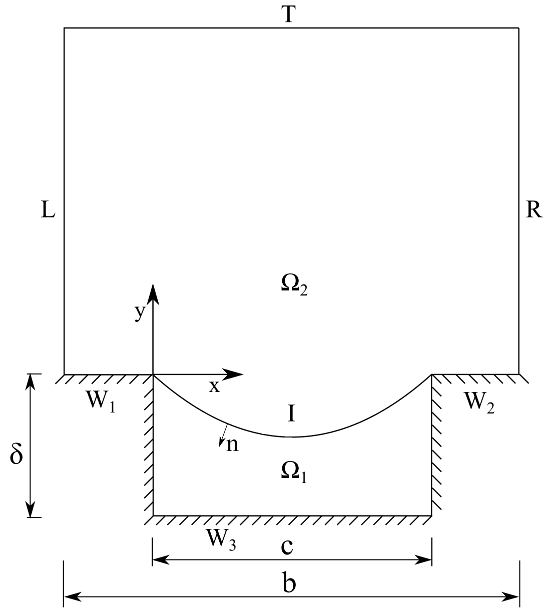

Figure 3.4: Sketch of two different fluid domains separated by the interface I. The letters T, L, R, I and W denote, respectively, the top, left, right boundaries, the interface and the wall. In the figure, W comprises all the walls of the cavity

The boundary conditions to be applied on each patch are described in figure 3.1 for both the transverse and the longitudinal problems. The standard no-slip conditions is applied at the walls composing the indentation, while patches L and R are periodic. They are explicitly reported in figure 3.4, since they have been taken into account while deriving the boundary integral equations. One of the interesting features of the BIM is that the integrals over the domain's boundaries can sometimes be eliminated, if a tailored Green's function is used during the derivation. In this case, the usage of a Greens' function satisfying the periodicity of the flow leads to a consistent simplification of the final mathematical formulation of the problem, avoiding the inclusion of the periodic boundaries. With the same reasoning, also the patch T can be eliminated, when using a Green's function which takes into account the asymptotic linear behavior of the velocity profile. However, in our formulation we maintain T in order to have a precise location to directly measure the velocity far from the wall and, thus, having immediate access to the value of the protrusion heights.

The main objective is to derive two boundary integral formulations for the longitudinal and the transverse flow. From their solution the values of the protrusions heights are calculated by varying the main physical and geometric parameters involved in the problems.

3.4 The microscopic longitudinal problem

We consider first the longitudinal flow over a periodic array of grooves aligned with the main flow direction. The Laplace equation holds in both the domains Ω_1 and Ω_2 and reads $\nabla^2 u = 0$. Considering a simple shear flow over such a surface, far from the wall the velocity profile is known to be [Crowdy, 2010]:

$$\boldsymbol{u} = (y + h_{||})\hat{\boldsymbol{x}}, \tag{3.32}$$

where $\hat{\boldsymbol{x}}$ is the flow direction and the constant $h_{||}$ is the already introduced longitudinal protrusion height. We transform the differential problem into an integral problem involving only quantities at the boundary of the domain, taking advantage of the boundary integral method.

Let us reintroduce the single-layer and the double-layer potentials for the Laplace equation, defined for a closed, two-dimensional, contours $\mathcal{C}$ as

$$\begin{aligned}
\mathcal{F}^{SLP}(\boldsymbol{x}_0, \nabla u \cdot \boldsymbol{n}; \mathcal{C}) &= \int_{\mathcal{C}} G(\boldsymbol{x}, \boldsymbol{x_0})[\nabla u(\boldsymbol{x}) \cdot \boldsymbol{n}]\, dl(\boldsymbol{x}), & (3.33)\\
\mathcal{F}^{DLP}(\boldsymbol{x}_0, u; \mathcal{C}) &= \int_{\mathcal{C}} u(\boldsymbol{x})[\nabla G(\boldsymbol{x}, \boldsymbol{x_0}) \cdot \boldsymbol{n}]\, dl(\boldsymbol{x}), & (3.34)
\end{aligned}$$

where $\boldsymbol{x}_0$ is the generic field point, $\boldsymbol{n}$ is the normal vector to the contour $\mathcal{C}$, pointing inward the domain, and $G(\boldsymbol{x}, \boldsymbol{x}_0)$ is the Green function for the two-dimensional Laplace equation. The basic idea is to derive one boundary integral equation, linking the fluid quantities at the boundary of the domain using the operators (3.33)-(3.34), for each patch composing the geometry under investigation. Maintaining the usual convention of the boundary integral method, all the normal vectors $\boldsymbol{n}$ defined over the patches point inward the respective domain; since the interface is shared between both the domains, we choose its normal pointing inward the domain Ω_1 (see figure 3.4) and, thus, the relation $\boldsymbol{n}^{(2)} = -\boldsymbol{n}^{(1)}$ holds on $\mathcal{I}$.

The starting point to derive the longitudinal flow integral representation is to apply the boundary integral formulation [Pozrikidis, 2002] in the lower fluid (superscript (1)) for a point $\boldsymbol{x}_0$ located at the interface I, which reads

$$\frac{u^{(1)}}{2} = -\mathcal{F}^{SLP}(\boldsymbol{x}_0, \nabla u^{(1)} \cdot \boldsymbol{n}; \mathsf{W}_3) - \mathcal{F}^{SLP}(\boldsymbol{x}_0, \nabla u^{(1)} \cdot \boldsymbol{n}^{(1)}; \mathsf{I}) + \hat{\mathcal{F}}^{DLP}(\boldsymbol{x}_0, u^{(1)}; \mathsf{I}), \tag{3.35}$$

where $\hat{\mathcal{F}}^{DLP}$ denotes the principal value of the double layer potential and the superscript is retained only in the normal vector defined over the interface to recall that in this case they are of opposite sign, while for the other cases it is implicitly assumed that the normal vector follows the convection described above. Repeating the derivation in the upper fluid (superscript (2)) for a point $\boldsymbol{x}_0$ located at the interface, we obtain

$$\begin{aligned}\frac{u^{(2)}}{2} = -\mathcal{F}^{SLP}(\boldsymbol{x}_0, \nabla u^{(2)} \cdot \boldsymbol{n}; \mathsf{W}_1 + \mathsf{W}_2 + \mathsf{T}) + \mathcal{F}^{DLP}(\boldsymbol{x}_0, u^{(2)}; \mathsf{T})\\ - \mathcal{F}^{SLP}(\boldsymbol{x}_0, \nabla u^{(2)} \cdot \boldsymbol{n}^{(2)}; \mathsf{I}) + \hat{\mathcal{F}}^{DLP}(\boldsymbol{x}_0, u^{(2)}; \mathsf{I}).\end{aligned} \tag{3.36}$$

It is worth noting that the contributions of the periodic boundaries $\mathcal{L}$ and $\mathcal{R}$ cancel out from the integral equations if a suitable Green's function for the Laplace equation [Pozrikidis, 2002] is employed during the derivations. Since the velocity is assumed continuous across the interface, we add equation (3.35), multiplied by the viscosity ratio $\lambda = \frac{\mu^{(1)}}{\mu^{(2)}}$, to equation (3.36) and we collect the terms involving the velocity at the interface. The multiplication by λ is necessary to introduce in the final boundary integral equation the dependence from this parameter. Proceeding as illustrated, the first boundary integral equation reads

$$\begin{aligned}\frac{1+\lambda}{2} u(\boldsymbol{x}_0) = \mathcal{F}^{DLP}(\boldsymbol{x}_0, u; \mathsf{T}) - \lambda \mathcal{F}^{SLP}(\boldsymbol{x}_0, \nabla u \cdot \boldsymbol{n}; \mathsf{W}_3)\\ - \mathcal{F}^{SLP}(\boldsymbol{x}_0, \nabla u \cdot \boldsymbol{n}; \mathsf{W}_1 + \mathsf{W}_2 + T)\\ + \mathcal{F}^{SLP}(\boldsymbol{x}_0, [\nabla u^{(2)} - \lambda \nabla u^{(1)}] \cdot \boldsymbol{n}; \mathsf{I}) + (\lambda - 1)\hat{\mathcal{F}}^{DLP}(\boldsymbol{x}_0, u; \mathsf{I}),\end{aligned} \tag{3.37}$$

with the interface unit normal vector $\boldsymbol{n}$ taken to coincide with $\boldsymbol{n}^{(1)}$.

Next, we consider the equation for the velocity in the lower fluid for a point $\boldsymbol{x}_0$ at the lower wall, multiplied by λ, together with the reciprocal relation for the Laplace equation [Pozrikidis, 2002]:

$$\begin{aligned}\frac{\lambda}{2} u^{(1)} = -\lambda \mathcal{F}^{SLP}(\boldsymbol{x}_0, \nabla u^{(1)} \cdot \boldsymbol{n}; \mathsf{W}_3)\\ - \lambda \mathcal{F}^{SLP}(\boldsymbol{x}_0, \nabla u^{(1)} \cdot \boldsymbol{n}^{(1)}; \mathsf{I}) + \lambda \mathcal{F}^{DLP}(\boldsymbol{x}_0, u^{(1)}; \mathsf{I}),\end{aligned} \tag{3.38}$$

$$
\begin{aligned}
-\mathcal{F}^{SLP}(\boldsymbol{x}_0, \nabla u^{(2)} \cdot \boldsymbol{n}; \mathsf{W}_1 + \mathsf{W}_2 + \mathsf{T}) + \mathcal{F}^{DLP}(\boldsymbol{x}_0, u^{(2)}; \mathsf{T}) \\
- \mathcal{F}^{SLP}(\boldsymbol{x}_0, \nabla u^{(2)} \cdot \boldsymbol{n}^{(2)}; \mathsf{I}) + \mathcal{F}^{DLP}(\boldsymbol{x}_0, u^{(2)}; \mathsf{I}) = 0. \quad (3.39)
\end{aligned}
$$

We move the term composing equation (3.39) from the left hand side to the right hand side and then we change its sign; adding the result of this manipulation to equation (3.38), we end up with

$$
\begin{aligned}
0 = \mathcal{F}^{DLP}(\boldsymbol{x}_0, u; \mathsf{T}) - \lambda \mathcal{F}^{SLP}(\boldsymbol{x}_0, \nabla u \cdot \boldsymbol{n}; \mathsf{W}_3) \\
- \mathcal{F}^{SLP}(\boldsymbol{x}_0, \nabla u \cdot \boldsymbol{n}; \mathsf{W}_1 + \mathsf{W}_2 + \mathsf{T}) + (\lambda - 1)\mathcal{F}^{DLP}(\boldsymbol{x}_0, u; \mathsf{I}) \\
+ \mathcal{F}^{SLP}(\boldsymbol{x}_0, [\nabla u^{(2)} - \lambda \nabla u^{(1)}] \cdot \boldsymbol{n}; \mathsf{I}), \quad (3.40)
\end{aligned}
$$

where the zero on the left hand side is due to the fact that the no-slip boundary condition is applied at the solid walls. The same equation can be derived for a point $\boldsymbol{x}_0$ belonging to the walls W_1 and W_2 by writing the equation for the upper fluid and the reciprocal relation, using as integration path the lower fluid domain, again multiplied by λ.

Finally, we apply the boundary integral formulation for a point $\boldsymbol{x}_0$ on the upper wall, and the reciprocal relation, multiplied by λ, obtaining:

$$
\begin{aligned}
\frac{u^{(2)}}{2} = -\mathcal{F}^{SLP}(\boldsymbol{x}_0, \nabla u^{(2)} \cdot \boldsymbol{n}; \mathsf{W}_1 + \mathsf{W}_2 + \mathsf{T}) + \mathcal{F}^{DLP}(\boldsymbol{x}_0, u^{(2)}; \mathsf{T}) + \\
- \mathcal{F}^{SLP}(\boldsymbol{x}_0, \nabla u^{(2)} \cdot \boldsymbol{n}^{(2)}; \mathsf{I}) + \mathcal{F}^{DLP}(\boldsymbol{x}_0, u^{(2)}; \mathsf{I}), \quad (3.41)
\end{aligned}
$$

$$
- \lambda \mathcal{F}^{SLP}(\boldsymbol{x}_0, \nabla u^{(1)} \cdot \boldsymbol{n}; \mathsf{W}_3) - \lambda \mathcal{F}^{SLP}(\boldsymbol{x}_0, \nabla u^{(1)} \cdot \boldsymbol{n}; \mathsf{I}) + \lambda \mathcal{F}^{DLP}(\boldsymbol{x}_0, u^{(1)}; \mathsf{I}) = 0. \quad (3.42)
$$

Summing the above equations (3.41) and (3.42) and performing similar manipulations as in equation (3.39), we obtain the last boundary integral equation

$$
\begin{aligned}
\frac{1}{2} u(\boldsymbol{x}_0) = \hat{\mathcal{F}}^{DLP}(\boldsymbol{x}_0, u; \mathsf{T}) - \lambda \mathcal{F}^{SLP}(\boldsymbol{x}_0, \nabla u \cdot \boldsymbol{n}; \mathsf{W}_3) \\
- \mathcal{F}^{SLP}(\boldsymbol{x}_0, \nabla u \cdot \boldsymbol{n}; \mathsf{W}_1 + \mathsf{W}_2 + \mathsf{T}) + (\lambda - 1)\mathcal{F}^{DLP}(\boldsymbol{x}_0, u; \mathsf{I}), \\
+ \mathcal{F}^{SLP}(\boldsymbol{x}_0, [\nabla u^{(2)} - \lambda \nabla u^{(1)}] \cdot \boldsymbol{n}; \mathsf{I}), \quad (3.43)
\end{aligned}
$$

which forms, together with (3.37) and (3.40), a system of integral equations for the unknown velocity or stress distribution along the domain's boundaries. The formulation undergoes a further simplification if the jump in shear stress across the interface, $[\nabla u^{(2)} - \lambda \nabla u^{(1)}] \cdot \boldsymbol{n}$, along the longitudinal direction is specified. In this particular problem we require $\nabla u^{(2)} \cdot \boldsymbol{n} = \lambda \nabla u^{(1)} \cdot \boldsymbol{n}$, i.e. we assume the shear stress to be continuous across the interface.

Once the velocity and its gradient are know at the boundaries, the internal field can be readily reconstructed by using the following integral relation:

$$\begin{aligned}\alpha u(\boldsymbol{x}_0) = -\lambda \mathcal{F}^{SLP}(\boldsymbol{x}_0, \nabla u \cdot \boldsymbol{n}; \mathsf{W}_3) - \mathcal{F}^{SLP}(\boldsymbol{x}_0, \nabla u \cdot \boldsymbol{n}; \mathsf{W}_1 + \mathsf{W}_2 + \mathsf{T}) \\ + \mathcal{F}^{DLP}(\boldsymbol{x}_0, u; \mathsf{T}) + (\lambda - 1)\mathcal{F}^{DLP}(\boldsymbol{x}_0, u; \mathsf{I}), \quad (3.44)\end{aligned}$$

with

$$\begin{cases} \alpha = \lambda, & \text{if} \quad \boldsymbol{x}_0 \in \Omega_1, \\ \alpha = 1, & \text{if} \quad \boldsymbol{x}_0 \in \Omega_2. \end{cases}$$

3.5 The microscopic transverse problem

Following a similar procedure to that described in the previous section, we derive the governing integral equations for the transverse problem, involving the wall normal and the spanwise components of the velocity vector, denoted by $\boldsymbol{v} = (w, v)$. We firstly introduce the single-layer and the double-layer potential for the Stokes flow, which read

$$\mathcal{F}_j^{SLP}(\boldsymbol{x}_0, \boldsymbol{f}; \mathcal{C}) = \frac{1}{4\pi\mu} \int_{\mathcal{C}} f_i(\boldsymbol{x}) \boldsymbol{G}_{ij}(\boldsymbol{x}, \boldsymbol{x_0}) \, dl(\boldsymbol{x}), \quad (3.45)$$

$$\mathcal{F}_j^{DLP}(\boldsymbol{x}_0, \boldsymbol{v}; \mathcal{C}) = \frac{1}{4\pi} \int_{\mathcal{C}} v_i(\boldsymbol{x}) \boldsymbol{T}_{ijk}(\boldsymbol{x}, \boldsymbol{x_0}) n_k(\boldsymbol{x}) \, dl(\boldsymbol{x}), \quad (3.46)$$

We start with the boundary integral representation for the velocity $u_j^{(1)}(\boldsymbol{x}_0)$ in the lower fluid, in the generic point $\boldsymbol{x}_0 \in \mathsf{I}$ [Pozrikidis, 1992]

$$\frac{1}{2} v_j^{(1)}(\boldsymbol{x}_0) = -\frac{1}{\lambda} \mathcal{F}_j^{SLP}(\boldsymbol{x}_0, \boldsymbol{f}^{(1)}; \mathsf{W}_3 + \mathsf{I}) + \mathcal{F}_j^{DLP}(\boldsymbol{x}_0, \boldsymbol{v}^{(1)}; \mathsf{W}_3) + \hat{\mathcal{F}}_j^{DLP}(\boldsymbol{x}_0, \boldsymbol{v}^{(1)}; \mathsf{I}), \quad (3.47)$$

where $\hat{\mathcal{F}}^{DLP}$ denotes the principal value of the double layer potential.

Repeating the same derivation for the velocity $v_j^{(2)}(\boldsymbol{x}_0)$ in the upper fluid, we obtain an analogous representation

$$\begin{aligned}\frac{1}{2} v_j^{(2)}(\boldsymbol{x}_0) = -\mathcal{F}_j^{SLP}(\boldsymbol{x}_0, \boldsymbol{f}^{(2)}; \mathsf{T} + \mathsf{W}_1 + \mathsf{W}_2 + \mathsf{I} + \mathsf{L} + \mathsf{R}) + \\ \mathcal{F}_j^{DLP}(\boldsymbol{x}_0, \boldsymbol{v}^{(2)}; \mathsf{T} + \mathsf{L} + \mathsf{R}) + \hat{\mathcal{F}}_j^{DLP}(\boldsymbol{x}_0, \boldsymbol{v}^{(2)}; \mathsf{I}). \quad (3.48)\end{aligned}$$

We assume no-slip along $\mathsf{W}_1, \mathsf{W}_2$ and W_3, while the left and right boundaries, L and R, are considered periodic. With these choices, equation (3.47) and (3.48) simplify in

$$\frac{1}{2}\lambda v_j^{(1)}(\boldsymbol{x}_0) = -\mathcal{F}_j^{SLP}(\boldsymbol{x}_0, \boldsymbol{f}^{(1)}; \mathsf{W}_3 + \mathsf{I}) + \lambda\hat{\mathcal{F}}_j^{DLP}(\boldsymbol{x}_0, \boldsymbol{v}^{(1)}; \mathsf{I}), \tag{3.49}$$

$$\begin{aligned}\frac{1}{2}v_j^{(2)}(\boldsymbol{x}_0) = &-\mathcal{F}_j^{SLP}(\boldsymbol{x}_0, \boldsymbol{f}^{(2)}; \mathsf{W}_1 + \mathsf{W}_2 + \mathsf{I} + \mathsf{T}) + \\ &\mathcal{F}_j^{DLP}(\boldsymbol{x}_0, \boldsymbol{v}^{(2)}; \mathsf{T}) + \hat{\mathcal{F}}_j^{DLP}(\boldsymbol{x}_0, \boldsymbol{v}^{(2)}; \mathsf{I}).\end{aligned} \tag{3.50}$$

It is worth noting that the contribution of the periodic boundaries cancels out from equation (3.48) only if the Green's function is chosen to be periodic. Next, we add equations (3.49) and (3.50) and, recalling that the velocity is continuous across the interface, we achieve the following final form:

$$\begin{aligned}\frac{1+\lambda}{2}v_j(\boldsymbol{x}_0) = &-\mathcal{F}_j^{SLP}(\boldsymbol{x}_0, \boldsymbol{f}; \mathsf{W} + \mathsf{T}) + \mathcal{F}_j^{DLP}(\boldsymbol{x}_0, \boldsymbol{v}; \mathsf{T}) \\ &-\mathcal{F}_j^{SLP}(\boldsymbol{x}_0, \Delta\boldsymbol{f}; \mathsf{I}) + (\lambda - 1)\hat{\mathcal{F}}_j^{DLP}(\boldsymbol{x}_0, \boldsymbol{v}; \mathsf{I}),\end{aligned} \tag{3.51}$$

with $\mathsf{W} = \mathsf{W}_1 + \mathsf{W}_2 + \mathsf{W}_3$. The non-dimensional jump in traction through the interface is $\Delta\boldsymbol{f} = \boldsymbol{f}^{(1)} - \boldsymbol{f}^{(2)} = \frac{K\boldsymbol{n}}{Ca}$, with Ca the capillary number, $Ca = \frac{\mu_2 u_{ref}}{\sigma_s}$; σ_s is the surface tension present at the interface between fluids 1 and 2, u_{ref} is the characteristic velocity of the problem and K is the local curvature of the interface. In the following, Ca will be understood to be a control parameter which tunes the rigidity of the fluid interface.

Proceeding further, we reconsider an arbitrary point $\boldsymbol{x}_0 \in \mathsf{W}_3$ but, this time, we derive an alternative integral relation for the velocity $v_j^{(1)}(\boldsymbol{x}_0)$ integrating over the contour of domain Ω_2 and taking advantage of the reciprocal theorem for Stokes flow, leading to:

$$-\mathcal{F}_j^{SLP}(\boldsymbol{x}_0, \boldsymbol{f}^{(1)}; \mathsf{T} + \mathsf{W}_1 + \mathsf{W}_2 + \mathsf{I}) + \mathcal{F}_j^{DLP}(\boldsymbol{x}_0, \boldsymbol{v}; \mathsf{T} + \mathsf{I}) = 0. \tag{3.52}$$

Recalling the orientation of the normal vector and the continuity of the velocity on the interface, summing with equation (3.49) we obtain:

$$\begin{aligned}\frac{1}{2}\lambda v_j(\boldsymbol{x}_0) = &-\mathcal{F}_j^{SLP}(\boldsymbol{x}_0, \boldsymbol{f}; \mathsf{T} + \mathsf{W}) + \mathcal{F}_j^{DLP}(\boldsymbol{x}_0, \boldsymbol{v}; \mathsf{T}) \\ &-\mathcal{F}_j^{SLP}(\boldsymbol{x}_0, \Delta\boldsymbol{f}; \mathsf{I}) + (\lambda - 1)\mathcal{F}_j^{DLP}(\boldsymbol{x}_0, \boldsymbol{v}^{(1)}; \mathsf{I}) = 0.\end{aligned} \tag{3.53}$$

A third integral equation can be obtained proceeding in the same way as before: we take an arbitrary point $\boldsymbol{x}_0 \in \mathsf{W}_{1,2}$, we integrate along the contour of domain Ω_1 and we apply the reciprocal theorem, i.e

$$-\mathcal{F}_j^{SLP}(\boldsymbol{x}_0, \boldsymbol{f}^{(2)}; \mathsf{W}_3 + \mathsf{I}) + \lambda\mathcal{F}_j^{DLP}(\boldsymbol{x}_0, \boldsymbol{v}^{(2)}; \mathsf{I}) = 0. \tag{3.54}$$

Again, we add equation (3.54) to equation (3.50) and end up with:

$$\frac{v_j(\boldsymbol{x}_0)}{2} = -\mathcal{F}_j^{SLP}(\boldsymbol{x}_0, \boldsymbol{f}; \mathsf{W}+\mathsf{T}) - \mathcal{F}_j^{SLP}(\boldsymbol{x}_0, \boldsymbol{f}; \mathsf{T}) + \mathcal{F}_j^{DLP}(\boldsymbol{x}_0, \boldsymbol{v}; \mathsf{T}) - \mathcal{F}_j^{SLP}(\boldsymbol{x}_0, \Delta\boldsymbol{f}; \mathsf{I}) + (\lambda-1)\mathcal{F}_j^{DLP}(\boldsymbol{x}_0, \boldsymbol{v}; \mathsf{I}) = 0. \quad (3.55)$$

If $\boldsymbol{x}_0 \in \mathsf{T}$ we obtain an equation formally similar to (3.55)

$$\frac{v_j(\boldsymbol{x}_0)}{2} = -\mathcal{F}_j^{SLP}(\boldsymbol{x}_0, \boldsymbol{f}; \mathsf{W}+\mathsf{T}) - \mathcal{F}_j^{SLP}(\boldsymbol{x}_0, \boldsymbol{f}; \mathsf{T}) + \hat{\mathcal{F}}_j^{DLP}(\boldsymbol{x}_0, \boldsymbol{v}; \mathsf{T}) - \mathcal{F}_j^{SLP}(\boldsymbol{x}_0, \Delta\boldsymbol{f}; \mathsf{I}) + (\lambda-1)\mathcal{F}_j^{DLP}(\boldsymbol{x}_0, \boldsymbol{v}; \mathsf{I}). \quad (3.56)$$

Equations (3.51), (3.53), (3.55) and (3.56) are a system of integral equations for the unknown stresses along the solid walls, the interface velocity and the velocity or the stress on the top wall T, as function of the applied boundary conditions. The internal velocity field can be reconstructed using the following relation

$$\alpha v_j(\boldsymbol{x}_0) = -\mathcal{F}_j^{SLP}(\boldsymbol{x}_0, \boldsymbol{f}; \mathsf{W}+\mathsf{T}) - \mathcal{F}_j^{SLP}(\boldsymbol{x}_0, \boldsymbol{f}; \mathsf{T}) + \mathcal{F}_j^{DLP}(\boldsymbol{x}_0, \boldsymbol{v}; \mathsf{T}) - \mathcal{F}_j^{SLP}(\boldsymbol{x}_0, \Delta\boldsymbol{f}; \mathsf{I}) + (\lambda-1)\mathcal{F}_j^{DLP}(\boldsymbol{x}_0, \boldsymbol{v}; \mathsf{I}) \quad (3.57)$$

with

$$\begin{cases} \alpha = \lambda, & \text{if} \quad \boldsymbol{x}_0 \in \Omega_1, \\ \alpha = 1, & \text{if} \quad \boldsymbol{x}_0 \in \Omega_2. \end{cases}$$

3.6 Flow over riblets of arbitrary shape

It is worth to note that the general integral representations can be conveniently simplified if the single phase flow over ribleted surfaces is under consideration. In this case there are no interfaces and the fluid properties are the same in the whole domain. The integral representations can be thus easily derived setting $\lambda = 1$ and deleting from the equations derived in section 3.4 and section 3.5 every integral involving the interface I. The integral representation for the longitudinal and the transverse flow reduce to

$$\alpha u(\boldsymbol{x}_0) = -\mathcal{F}^{SLP}(\boldsymbol{x}_0, \nabla u \cdot \boldsymbol{n}; \mathsf{W}+\mathsf{T}) + \mathcal{F}^{DLP}(\boldsymbol{x}_0, u; \mathsf{T}), \quad (3.58)$$

$$\alpha v_j(\boldsymbol{x}_0) = -\mathcal{F}_j^{SLP}(\boldsymbol{x}_0, \boldsymbol{f}; \mathsf{W}+\mathsf{T}) + \hat{\mathcal{F}}_j^{DLP}(\boldsymbol{x}_0, \boldsymbol{v}; \mathsf{T}), \quad (3.59)$$

with

$$\begin{cases} \alpha = \frac{1}{2}, & \text{if} \quad \boldsymbol{x}_0 \in \mathsf{W},\ \mathsf{T}, \\ \alpha = 1, & \text{if} \quad \boldsymbol{x}_0 \in \Omega, \end{cases}$$

for the longitudinal and transverse problem respectively. The integral representation (3.58) and (3.59) are equivalent to those given by Luchini et al. [1991], but expressed here in terms of primary variables and not in terms of stream function and vorticity.

3.7 Numerical Method

The integral equations described in the previous sections hardly present an analytical solution due to the complexity of the integral operators. The common practice to obtain a solution is to employ the boundary element method (BEM). The BEM is the numerical counterpart of BIM and consists in subdividing the boundary of the domain into a collection of discrete elements. The shape of the element is important in order to obtain an accurate representation of the boundary with a low number of element and minimize the computational efforts. The simplest option is to approximate the boundary with a set of straight segments, while more involved solutions require the usage of high order spline approximations. The elements' shape is not the only choice to be taken, since also the boundary quantities in the integral have to be somehow estimated. The simplest option is to consider constant the integrand function over each element, but in this case a large number of elements is to be expected if an accurate solution is needed. A higher order approximation based on polynomial interpolants is often used to obtain a more accurate solution with a lower resolution. One aspect that is always to keep in mind is that both the shape of the elements and the order of the boundary quantity interpolants directly reflect on the complexity of the method, leading to a higher efforts in assembling the numerical code. On the basis of the choices taken for the shape of elements and the approximation of the boundary quantities, different types of BEMs are defined [Katsikadelis, 2002]

- sub-parametric: the elements have a lower order with respect to the boundary quantities;
- iso-parametric: the elements and the boundary quantities are of same order;
- super-parametric: the elements have an higher order with respect to the boundary quantities.

Our choice is to use a super-parametric BEM, which has a good balance between accuracy and difficulty of implementation. We employ a linear approximation for the boundary quantities, while cubic splines for the elements in order to have a good approximation of possibly non-straight boundaries. A detail description of the numerical method is postponed to sections 3.7.1 and 3.7.2; here we proceed to the discretization of the governing integral equation, without specifying any type of approximation for either the discrete elements or the boundary quantities, leading to a general numerical discretization. Independently from the type of BEM, its main advantage is that it is not necessary to compute the required functions throughout the domain of solution. Once the unknown boundary distribution is available, the solution at any point may be produced by direct evaluation. Thus, the key of the boundary-element method is the reduction of the dimension of the solution space with respect to physical space by one unit.

Let us proceed to the discretization and thus define N_T, $N_W = N_{W_1} + N_{W_2} + N_{W_3}$ and N_I as the number of the collocation points distributed along the top boundary, the lower wall and the interface, respectively. The integral equations in their discrete form for the longitudinal problem read

$$\begin{cases} -\boldsymbol{D}^{TT}\cdot\boldsymbol{u}^T + \dfrac{1}{2}\boldsymbol{u}^T + \boldsymbol{S}^{TW_{1,2}}\cdot\boldsymbol{u}_n^{W_{1,2}} + \lambda\boldsymbol{S}^{TW_3}\cdot\boldsymbol{u}_n^{W_3} - (\lambda-1)\boldsymbol{D}^{TI}\cdot\boldsymbol{u}^I = \\ -\boldsymbol{S}^{TT}\cdot\boldsymbol{u}_n^T - \boldsymbol{S}^{TI}\cdot\Delta\boldsymbol{u}_n^I, \\ -\boldsymbol{D}^{WT}\cdot\boldsymbol{u}^T - (\lambda-1)\boldsymbol{D}^{WI}\cdot u^I + \lambda\boldsymbol{S}^{WW_3}\cdot\boldsymbol{u}_n^{W_3} + \boldsymbol{S}^{WW_{1,2}}\cdot\boldsymbol{u}_n^{W_{1,2}} = \\ -\boldsymbol{S}^{WT}\cdot\boldsymbol{u}_n^T - \boldsymbol{S}^{WI}\cdot\Delta\boldsymbol{u}_n^I, \\ -\boldsymbol{D}^{IT}\cdot\boldsymbol{u}^T + \lambda\boldsymbol{S}^{IW_3}\cdot\boldsymbol{u}_n^{W_3} + \boldsymbol{S}^{IW_{1,2}}\cdot\boldsymbol{u}_n^{W_{1,2}} - (\lambda-1)\boldsymbol{D}^{II}\cdot\boldsymbol{u}^I + \dfrac{1+\lambda}{2}\boldsymbol{u}^I = \\ -\boldsymbol{S}^{IT}\cdot\boldsymbol{u}_n^T - \boldsymbol{S}^{II}\cdot\Delta\boldsymbol{u}_n^I, \end{cases} \tag{3.60}$$

while for the transverse problem

$$\begin{cases} -\boldsymbol{D}^{TT}\cdot\boldsymbol{v}^T + \dfrac{1}{2}\boldsymbol{v}^T + \boldsymbol{S}^{TW}\cdot\boldsymbol{f}^W - (\lambda-1)\boldsymbol{D}^{TI}\cdot\boldsymbol{v}^I = -\boldsymbol{S}^{TT}\cdot\boldsymbol{f}^T - \boldsymbol{S}^{TI}\cdot\Delta\boldsymbol{f}^I, \\ -\boldsymbol{D}^{WT}\cdot\boldsymbol{v}^T - (\lambda-1)\boldsymbol{D}^{WI}\cdot\boldsymbol{v}^I + \boldsymbol{S}^{WW}\cdot\boldsymbol{f}^W = -\boldsymbol{S}^{WT}\cdot\boldsymbol{f}^T - \boldsymbol{S}^{WI}\cdot\Delta\boldsymbol{f}^I, \\ -\boldsymbol{D}^{IT}\cdot\boldsymbol{v}^T + \boldsymbol{S}^{IW}\cdot\boldsymbol{f}^W - (\lambda-1)\boldsymbol{D}^{II}\cdot\boldsymbol{v}^I + \dfrac{1+\lambda}{2}\boldsymbol{v}^I = -\boldsymbol{S}^{IT}\cdot\boldsymbol{f}^T - \boldsymbol{S}^{II}\cdot\Delta\boldsymbol{f}^I. \end{cases} \tag{3.61}$$

The quantity $\boldsymbol{u}_n$ is shorthand notation for scalar product $\nabla\boldsymbol{u}\cdot\boldsymbol{n}$, while $\Delta\boldsymbol{u}_n = [\lambda\nabla u^{(1)} - \nabla u^{(2)}]\cdot\boldsymbol{n}$ is the jump in shear stress across the interface and along the longitudinal direction; the matrices $\boldsymbol{S}$ and $\boldsymbol{D}$ are called influence matrices and are the discretized counterpart of the single-layer and the double-layer potential operators defined in (3.45) and (3.46). The first letter in the superscript denotes the position of the collocation point, while the second letter identifies the piece of boundary over which the integral operator is being evaluated. Since the matrices $\boldsymbol{D}^{**}$ have the same size of the corresponding matrices $\boldsymbol{S}^{**}$, only the size of the matrices $\boldsymbol{S}^{**}$ is reported in table 3.1. Regarding the expression of the coefficients of $\boldsymbol{S}$ and $\boldsymbol{D}$, they strictly depends on the shape and the order of the interpolation of the boundary quantities along the elements.

$\boldsymbol{S}^{TT}$	$2N_T \times 2N_T$	$\boldsymbol{S}^{WI}$	$2N_W \times 2N_I$
$\boldsymbol{S}^{WT}$	$2N_W \times 2N_T$	$\boldsymbol{S}^{WW}$	$2N_W \times 2N_W$
$\boldsymbol{S}^{TW}$	$2N_T \times 2N_W$	$\boldsymbol{S}^{IT}$	$2N_I \times 2N_T$
$\boldsymbol{S}^{TI}$	$2N_T \times 2N_I$	$\boldsymbol{S}^{IW}$	$2N_I \times 2N_W$
$\boldsymbol{S}^{WT}$	$2N_W \times 2N_T$	$\boldsymbol{S}^{II}$	$2N_I \times 2N_I$

Table 3.1: Size of the discretized single-layer operator.

If the longitudinal problem is being considered, the size of the operators reported in table 3.1 is to be divided by a factor 4, since the field has only one component.

3.7.1 Domain Discretization

Different types of elements can be employed in order to approximate the domain's boundary, however the most accurate results are given by elements defined by cubic spline interpolation, which lead to a globally smooth representation. To implement this discretization, let us describe the boundary with n_c arbitrary spaced nodes and define at the i^{th} node the current length s_i of the polygonal line connecting sequential nodes, measured from an arbitrary starting point.

The i^{th} boundary element included between the i and $i+1$ node is described in parametric form by the cubic polynomials:

$$x(s) = B(s) = a_i(s-s_i)^3 + b_i(s-s_i)^2 + c_i(s-s_i) + x_i^G, \tag{3.62}$$

$$y(s) = B^{'}(s) = \hat{a}_i(s-s_i)^3 + \hat{b}_i(s-s_i)^2 + \hat{c}_i(s-s_i) + y_i^G, \tag{3.63}$$

with $\boldsymbol{x}_i^G = (x_i^G, y_i^G)$ the Cartesian coordinates of the i^{th} node. Three conditions for each coordinate parametrization are needed to fix the coefficients in equations (3.62) and (3.63). Keeping, for example, the $x-$coordinate and defining $h_i = s - s_i$, we must require:

1. the interpolation condition:

$$P_i(s_i+1) = x_{i+1}^G = x_i^G + a_{x_i} h_i^3 + b_i h_i^2 + c_i h_i, \quad i = 1, \ldots, n_c - 1 \tag{3.64}$$

2. the slope continuity at the interior nodes, $\frac{dP_i(s_i+1)}{ds} = \frac{dP_{i+1}(s_i+1)}{ds}$:

$$3a_i h_i^2 + 2b_i h_i + c_i = c_{i+1}, \quad i = 1, \ldots, n_c - 2 \tag{3.65}$$

3. the continuity of curvature interior nodes, $\frac{d^2P_i(s_i+1)}{ds^2} = \frac{d^2P_{i+1}(s_i+1)}{ds^2}$:

$$6a_i h_i + 2b_i = 2b_{i+1}, \quad i = 1, \ldots, n_c - 2. \tag{3.66}$$

Rearranging properly relations (3.64-3.66) we can find the following relations for the unknown coefficients:

$$\frac{h_i}{3} b_{i+2} + 2\frac{h_i + h_{i+1}}{3} b_{i+1} + \frac{h_{i+1}}{3} b_{i+2} = \frac{x^G_{i+2} - x^G_{i+1}}{h_{i+1}} - \frac{x^G - x^G_{i+1} - x^G_i}{h_i}, \tag{3.67}$$

$$a_i = \frac{b_{i+1} + b_i}{3h_i} \tag{3.68}$$

$$c_i = \frac{x^G - x^G_{i+1} - x^G_i}{h_i} + h_i \frac{b_{i+1} + 2b_i}{3}, \tag{3.69}$$

for $i = 1, \ldots, n_c - 2$. Thus, relation (3.67), (3.68) and (3.69) lead to a linear system of $n_c - 2$ equations in n_c unknowns, which require two more equations to be solved. One simple way to overcome this problem is to fix $b_1 = 0$ and $b_{n_c} = 0$, which practically means to impose a zero local curvature at starting and ending points of the discretized contour. A more gentle way to treat the boundary conditions is to use the clamped end spline, which fixes the slope at the boundary points with the same value of the third order Lagrangian polynomial fitting the three nearest neighbouring points; the latter is our favourite choice.

Finally, having obtain the spline coefficients for all the elements, the local curvature along the discrete contour is:

$$K = \frac{x_s y_{ss} - y_s x_{ss}}{({x_s}^2 + {y_s}^2)^{\frac{3}{2}}}, \tag{3.70}$$

where the subscript s denotes the derivative with respect to the curvilinear abscissa.

3.7.2 Computation of the boundary integrals

In this section, we describe more extensively some numerical details. In particular, we consider the computation of the single-layer and the double-layer integral operators, which are the entries of the matrices $\boldsymbol{S}^{**}$ and $\boldsymbol{D}^{**}$ composing the discrete system of boundary integral equations.

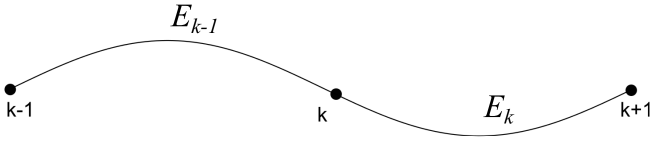

Figure 3.5: Sketch of two adjacent elements approximated by cubic splines. The symbol • represents the collocations points defined at the end of each element.

The starting point is to define the shape of the boundary element, which, in our case, is a spline connecting two collocation points, as shown in figure 3.5. We define a curvilinear abscissa, s, over the element E^k and we recast the operators (3.45) and (3.46) as

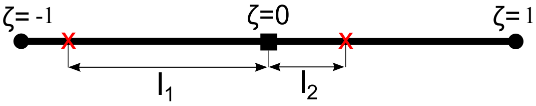

Figure 3.6: Schematic view of an element parametrized using the local coordinates ζ: the red cross marks the position of the collocation points, while the black dot marks the starting and ending points of the element.

$$\mathcal{F}_j^{SLP}(\boldsymbol{x}_0, \boldsymbol{u}; E_k) = \int_{s1}^{s2} f_i^k[\boldsymbol{x}(s)]\boldsymbol{G}_{ij}[\boldsymbol{x}(s), \boldsymbol{x_0}]h_s^k(s)\, ds \tag{3.71}$$

$$\mathcal{F}_j^{DLP}(\boldsymbol{x}_0, \boldsymbol{u}; E_k) = \int_{s_1}^{s2} u_i^k[\boldsymbol{x}(s)]\boldsymbol{T}_{ijl}[\boldsymbol{x}(s), \boldsymbol{x_0}]n_l[\boldsymbol{x}(s)]h_s^k(s)\, ds, \tag{3.72}$$

where $h_s^k(s)$ is the metric associated with the element:

$$h_s(s) = \left[\left(\frac{dx}{ds}\right)^2 + \left(\frac{dy}{ds}\right)^2\right]^{\frac{1}{2}}. \tag{3.73}$$

We apply another coordinate transformation which maps an element from the global coordinate system based on the curvilinear abscissa to a local coordinate system such that the k^{th} element's boundary points are mapped onto the interval $[-1, 1]$. This mapping will result useful for the numerical quadrature of boundary integrals and can be simply carried out using the following relation:

$$s(\zeta) = \frac{(s_1 + s_2)}{2} + \frac{(s_2 - s_1)}{2}\zeta = s_m + s_d\zeta, \tag{3.74}$$

from which we can easily define the associated metric $h_\zeta = s_d$. Introducing this new parametrization into the integrals (3.71) and (3.72) we obtain:

$$\mathcal{F}_j^{SLP}(\boldsymbol{x}_0, \boldsymbol{f}; E_k) = h_\zeta^k \int_{-1}^{1} f_i^k(\boldsymbol{x}(s(\zeta)))\boldsymbol{G}_{ij}(\boldsymbol{x}(s(\zeta)), \boldsymbol{x_0})h_s^k(s(\zeta))\, d\zeta, \tag{3.75}$$

$$\mathcal{F}_j^{DLP}(\boldsymbol{x}_0, \boldsymbol{u}; E_k) = h_\zeta^k \int_{-1}^{1} u_i^k(\boldsymbol{x}(s(\zeta)))\boldsymbol{T}_{ijk}(\boldsymbol{x}(s(\zeta)), \boldsymbol{x_0})n_k(\boldsymbol{x}(s(\zeta)))h_s^k(s(\zeta))\, d\zeta. \tag{3.76}$$

Until now, no assumption has been made on the interpolation method of the boundary quantities over the element. We use a piecewise linear variation, which is a good compromise between accuracy and programming difficulty; thus, let us consider an element parametrised using the local coordinate ζ, as show in figure 3.6, and require that:

$$\boldsymbol{u}(\zeta) = \psi_1(\zeta)\boldsymbol{u}_1 + \psi_2(\zeta)\boldsymbol{u}_2, \tag{3.77}$$

$$\boldsymbol{f}(\zeta) = \psi_1(\zeta)\boldsymbol{f}_1 + \psi_2(\zeta)\boldsymbol{f}_2, \tag{3.78}$$

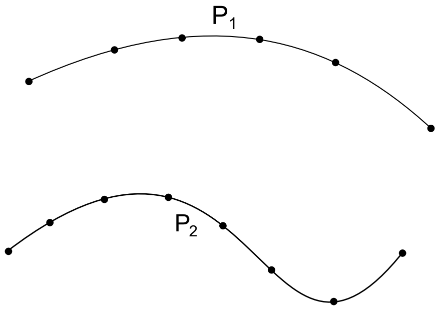

Figure 3.7: Sketch of two boundary patches, with several collocation point defined over them.

where $\psi_1 = \dfrac{l_2 - \zeta}{L}$ and $\psi_2 = \dfrac{l_1 + \zeta}{L}$ are shape functions. Introducing relations (3.77) and (3.78) into the expression of the single- and double-layer integrals, we can recast (3.75) and (3.76) as:

$$\mathcal{F}_j^{SLP}(\boldsymbol{x}_0, \boldsymbol{f}; E_k) = f_i^k A_{ij}^1 + f_i^{k+1} A_{ij}^2, \tag{3.79}$$

$$\mathcal{F}_j^{DLP}(\boldsymbol{x}_0, \boldsymbol{u}; E_k) = u_i^k B_{ij}^1 + u_i^{k+1} B_{ij}^2, \tag{3.80}$$

where A_{ij}^n and B_{ij}^n are know tensors of the form:

$$A_{ij}^n = h_\zeta^k \int_{-1}^{1} \psi_n(\zeta) \boldsymbol{G}_{ij}(\zeta) h_s(\zeta)\, d\zeta, \tag{3.81}$$

$$B_{ij}^n = h_\zeta^k \int_{-1}^{1} \psi_n(\zeta) \boldsymbol{T}_{ijl}(\zeta) n_l(\zeta) h_s(\zeta)\, d\zeta. \tag{3.82}$$

The integrals (3.81) and (3.82) can be computed numerically by using the Guass-Legendre quadrature rule, if the integrand is non-singular. The singular integral case is more tricky and special techniques must be employed, as extensively illustrated in the following section. We consider now two adjacent elements sharing the k^{th} collocation point, as shown in figure 3.5, and we write down the following quantities

$$\boldsymbol{SL}_k^l = A_{ij}^2|_k^{k-1} + A_{ij}^1|_k^k, \tag{3.83}$$

$$\boldsymbol{DL}_k^l = B_{ij}^2|_k^{k-1} + B_{ij}^1|_k^k, \tag{3.84}$$

where in the notation $|_*^*$ the superscript stands for the element over which the integral is being evaluated, while the subscript represents the collocation point considered.

As an example, referring to figure 3.7, we consider the assembling of the influence matrix $\boldsymbol{D}^{P_1 P_2}$ relative to the double-layer potential operator for two arbitrary patches, called P_1 and P_2, with N_{P_1} and N_{P_2} collocation points, respectively.

The discretized double-layer operator $\boldsymbol{D}^{P_1 P_2}$ reads

$$\boldsymbol{D}^{P_1P_2} = \begin{bmatrix} \boldsymbol{DL}_1^1 & \boldsymbol{DL}_2^1 & \dots & \boldsymbol{DL}_1^{N_{P_2}} \\ \boldsymbol{DL}_2^1 & \boldsymbol{DL}_2^2 & \dots & \boldsymbol{DL}_1^{N_{P_2}} \\ \vdots & \vdots & \vdots & \vdots \\ \boldsymbol{DL}_{N_{P_1}}^1 & \boldsymbol{DL}_{N_{P_1}}^2 & \dots & \boldsymbol{DL}_{N_{P_1}}^{N_{P_2}} \end{bmatrix}; \tag{3.85}$$

here $\boldsymbol{DL}_k^l$ stands for the quantities (3.84) calculated at the k^{th} point belonging to P_2 considering the l^{th} collocation point belonging to P_1. Particular attention should be paid when a collocation point is not shared by two adjacent segments. In this case $\boldsymbol{DL}^k$ turns out to be

$$\boldsymbol{DL}_k^l = B_{ij}^1|_k^k, \tag{3.86}$$

if the collocation point is located on the left of the element, while

$$\boldsymbol{DL}_k^l = B_{ij}^2|_k^k, \tag{3.87}$$

if the collocation point is located on the right of the element. The assembling methodology is the same for other cases, with no difference in the procedure if we consider the single-layer potential.

3.7.3 Non-singular integrals

The integrals (3.81)-(3.82) are the building blocks for the numerical solution of the boundary integral equations. Let us recall the periodic velocity Green's function and its associated stress tensor in order to highlight the problems that may arise in their numerical evaluation. Starting from $\boldsymbol{G}_{ij}$:

$$A(\hat{\boldsymbol{x}}) = \frac{1}{2}\log\{2[\cosh(\omega\hat{y}) - \cos(\omega\hat{x})]\}, \tag{3.88}$$

$$G_{11} = -A(\hat{\boldsymbol{x}}) - \hat{y}\frac{\partial A(\hat{\boldsymbol{x}})}{\partial \hat{y}} + 1, \tag{3.89}$$

$$G_{12} = \hat{y}\frac{\partial A(\hat{\boldsymbol{x}})}{\partial \hat{x}}, \tag{3.90}$$

$$G_{22} = A(\hat{\boldsymbol{x}}) + \hat{y}\frac{\partial A(\hat{\boldsymbol{x}})}{\partial \hat{x}}. \tag{3.91}$$

where $\hat{\boldsymbol{x}} = \boldsymbol{x} - \boldsymbol{x}_0$ and $\omega = \frac{2\pi}{L}$, with L the period of the flow. The components of the stress tensor $\boldsymbol{T}_{ijk}$ are:

$$T_{111} = -4\frac{\partial A(\hat{\boldsymbol{x}})}{\partial \hat{x}} - 2\hat{y}\frac{\partial^2 A(\hat{\boldsymbol{x}})}{\partial \hat{x}\partial \hat{y}}, \quad T_{112} = -2\frac{\partial A(\hat{\boldsymbol{x}})}{\partial \hat{y}} - 2\hat{y}\frac{\partial^2 A(\hat{\boldsymbol{x}})}{\partial \hat{y}\partial \hat{y}}, \tag{3.92}$$

$$T_{212} = 2\hat{y}\frac{\partial^2 A(\hat{\boldsymbol{x}})}{\partial \hat{x}\partial \hat{y}}, \quad T_{222} = -2\frac{\partial A(\hat{\boldsymbol{x}})}{\partial \hat{y}} + 2\hat{y}\frac{\partial^2 A(\hat{\boldsymbol{x}})}{\partial \hat{y}\partial \hat{y}}. \tag{3.93}$$

If the point $\boldsymbol{x}_0$ does not lay over the same element for which we are performing the integration, integrals (3.81) and (3.82) are not singular and can be approximated using the Gauss-Legendre formula, using N_q quadrature points, as:

$$h_\zeta^k \int_{-1}^{1} \psi_n(\zeta) \boldsymbol{G}_{ij}(\zeta) h_s(\zeta)\, d\zeta = h_\zeta^k \sum_{q=1}^{N_q} \psi_n(\zeta_q) \boldsymbol{G}_{ij}(\zeta_q) h_s(\zeta_q) w_q, \tag{3.94}$$

$$h_\zeta^k \int_{-1}^{1} \psi_n(\zeta) \boldsymbol{G}_{ij}(\zeta) h_s(\zeta)\, d\zeta = h_\zeta^k \sum_{q=1}^{N_q} \psi_n(\zeta_q) \boldsymbol{T}_{ijl}(\zeta_q) n_l(\zeta) h_s(\zeta_q), \tag{3.95}$$

where ζ_q is the position of the q^{th} quadrature point along the interval $[-1, 1]$ and w_q is the associated weight.

3.7.4 Singular integrals

In the case of two-dimensional flows, as considered here, since the integrand of the double-layer potential exhibits a discontinuity across the collocation point $\boldsymbol{x}_0$ special accommodations are not necessary. In contrast, the single-layer potential exhibits a logarithmic singularity for the diagonal component of $\boldsymbol{G}$. The basic idea to solve this problem is to subtract off the singularity. Thus, turning attention only to the term which contains the logarithm we add and subtract $h_s \psi(s) \log(r), r = |\boldsymbol{x} - \boldsymbol{x}_0|$, to the integrand in (3.71), obtaining:

$$\begin{aligned} -\frac{1}{2} \int_{s_1}^{s_2} h_s(s) \psi_n(s) \log\{2[\cosh(\omega \hat{x}_2) - \cos(\omega \hat{x}_1)]\}\, ds = \\ -\frac{1}{2} \left[\int_{s_1}^{s_2} h_s(s) \psi_n(s) \log\left\{ \frac{2}{r} [\cosh(\omega \hat{x}_2) - \cos(\omega \hat{x}_1)] \right\} + \right. \\ \left. h_s \psi_n(s) \log(r)\, ds \right]. \end{aligned} \tag{3.96}$$

The first term of the integrand is non-singular and can be accurately computed by Gauss-Legendre quadrature, but the second term involving $\log(r)$ is still singular and further manipulations are necessary. Calling s_0 the curvilinear abscissa of the singular point, we add and subtract $h_s(s)\psi_n(s) log(|s - s_0|)$ and recast the integral as:

$$\begin{aligned} \int_{s_1}^{s_2} h_s \psi_n(s) \log(r)\, ds = \int_{s_1}^{s_2} h_s(s) \psi_n(s) \log\left(\frac{r}{|s - s_0|} \right) ds + \\ \int_{s_1}^{s_2} h_s \psi_n(s) log(|s - s_0|)\, ds. \end{aligned} \tag{3.97}$$

Again, the first term in the integrand is non-singular, but we must proceed to desingularize the second term:

$$\begin{aligned} \int_{s_1}^{s_2} h_s(s) \psi_n(s) log(|s - s_0|)\, ds = \int_{s_1}^{s_2} \left[h_s \psi_n(s) - h_s(s_0) \psi_n(s_0) \right] \log(|s - s_0|)\, ds + \\ \int_{s_1}^{s_2} h_s(s_0) \psi_n(s_0) \log(|s - s_0|)\, ds. \end{aligned} \tag{3.98}$$

Finally we can conclude the de-singularization noting that $h_s(s_0)\psi_n(s_0)$ is constant thus:

$$\begin{aligned}\int_{s_1}^{s_2} h_s(s_0)\psi_n(s_0)\log(|s-s_0|)\,ds = h_s(s_0)\psi_n(s_0)\Big[&|s_2-s_0|\big(\log(|s_2-s_0|)-1\big)\\ &+|s_1-s_0|\big(\log(|s_1-s_0|)-1\big)\Big]. \qquad (3.99)\end{aligned}$$

Summing up, we can compute numerically the singular integral on the left-hand-side of (3.96) as:

$$\begin{aligned}&-\frac{1}{2}\int_{s_1}^{s_2} h_s(s)\psi_n(s)\log\{2[\cosh(\omega\hat{x}_2)-\cos(\omega\hat{x}_1)]\}\,ds =\\ &-\sum_{q=1}^{N_q}\frac{h_\zeta w_q}{2}\Bigg[h_s(\zeta_q)\psi_n(\zeta_q)\log\left\{\frac{2}{r}[\cosh(\omega\hat{x}_2(\zeta_q))-\cos(\omega\hat{x}_1(\zeta_q))]\right\}+\\ &h_s(\zeta_q)\psi_n(\zeta_q)\log\left(\frac{r}{|s(\zeta_q)-s_0|}\right)+\big[h_s(\zeta_q)\psi_n(\zeta_q)-h_s(s_0)\psi_n(s_0)\big]\log(|s(\zeta_q)-s_0|)\Bigg]-\\ &\frac{h_s(s_0)\psi_n(s_0)}{2}\Big(|s_2-s_0|\big(\log(|s_2-s_0|)-1\big)+|s_1-s_0|\big(\log(|s_1-s_0|)-1\big)\Big).\end{aligned}$$

3.7.5 Time advancement of the interface

The problem to be solved holds under the quasi-steady approximation and thus there is no explicit time dependency. However, because of the presence of surface tension, the interface has to be advanced through a series of intermediate states in order to find its steady state position, prescribed by the physical parameters involved in the simulation. Since we have assumed that there this no deformation along the longitudinal direction, then the interfaces is to be updated in time only along transverse direction. In doing so, the boundary element method presents notable advantages with respect to other interface tracking techniques, since we can easily perform an accurate Lagrangian tracking of the interface, using the collocation points employed for the discretization. In our code they are advanced in time using the following rule

$$\frac{d\boldsymbol{x}^{(i)}}{dt} = (\boldsymbol{u}_i\cdot\boldsymbol{n}_i)\boldsymbol{n}_i, \quad i=1,\dots,N_I, \qquad (3.100)$$

where $\boldsymbol{x}^{(i)}$ are the i^{th} collocation point and $\boldsymbol{n}_i$ is the normal to the interface at $\boldsymbol{x}^{(i)}$. Using the normal velocity to advance the interface, instead of the velocity $\boldsymbol{u}$, is found to be very effective in limiting the spreading of the collocation points, with the consequent advantage that the interface does not need to be frequently remeshed. Equation (3.100) can be discretized with any explicit scheme for ordinary differential equations. We have implemented both the first order Euler and the second order Runge-Kutta (RK2) integration, finding very few differences between the two schemes. However, since the RK2 scheme requires the evaluation of the interfacial velocity at two different time steps, with the consequent solution of the boundary element system, we prefer a simpler and faster one-step integration.

Once the interface reaches a steady state, its shape is used for the computation of the longitudinal protrusion heights.

3.7.6 Enforcement of mass conservation

One hidden issue in solving flows in the presence of interfaces, is that a unique solution of the integral equations cannot be found for arbitrary values of the viscosity ratio λ. This was described in particular by Pozrikidis [1992, 2002] and the drawback encountered in solving such equations is that a leak or an increase of the mass of fluid inside a closed domain may occur in time; this phenomenon becomes more important as the viscosity ratio λ decreases [Tanzosh et al., 1992]. One way to deal with this problem and remove the non-uniqueness of the solution is proposed in Pozrikidis [2001] and requires adding the following term

$$z_j(\boldsymbol{x}_0) \int_C u_i(\boldsymbol{x}) n_i(\boldsymbol{x}) dl \tag{3.101}$$

to the double-layer potential along the interface into the integral equations. Here $z_j(\boldsymbol{x}_0)$ is an arbitrary function such that $\int_C z_i n_i \neq 0$, with n_j the normal vector to the interface. The simplest choice is $z_j = n_j$ and, since this terms shift the eigenvalues of the double-layer potential operator, the procedure is known as *deflation*.

An alternative method to ensure mass conservation is proposed here. We start by noting that each boundary integral problem can be reduced to the solution of a linear system of the type:

$$\boldsymbol{A}\boldsymbol{x} = \boldsymbol{b}, \tag{3.102}$$

where $\boldsymbol{A}$ and $\boldsymbol{b}$ are the boundary element matrix and the right-hand-side, dependent on the original boundary integral formulation of the problem, while $\boldsymbol{x}$ is the vector containing the unknowns. For incompressible flows, the mass conservation inside a domain Ω_i can be readily written as

$$\nabla \cdot \boldsymbol{u} = 0, \tag{3.103}$$

with $\boldsymbol{u}$ the velocity vector inside the domain Ω_i. Integrating (3.103) over the volume Ω_i and taking advantage of Green's theorem we obtain

$$\int_{\partial\Omega} \boldsymbol{u} \cdot \boldsymbol{n} \, dS = 0. \tag{3.104}$$

The integral relation (3.104) can be discretized in the same fashion as the single-layer and the double-layer potentials, leading to a simple linear equation of the form

$$\boldsymbol{c} \cdot \boldsymbol{u} = 0, \tag{3.105}$$

where $\boldsymbol{c}$ is a vector containing the coefficients of the unknown velocity at the collocation points. The form of the coefficient depends, again, on the type of collocation method chosen to discretize the boundary integral equation. If we are in the presence of multiple fluid volumes, we can easily extend expression (3.105) as

$$\boldsymbol{C}\boldsymbol{x} = \boldsymbol{0}. \tag{3.106}$$

The i^{th} row of the matrix $\boldsymbol{C}$ contains the coefficients arising from the discretization of equation (3.104) for the i^{th} fluid domain. Clearly, the matrix $\boldsymbol{C}$ will present zero entries for those unknowns which are not the interfacial velocities to be constrained. We now wish to add the set of mass-conservation constraints to the boundary element system (3.102); this is not an easy task since, usually, the system is already closed and simply adding an additional constraint equation will lead to an over-determined system. Discharging as many equations as the number of constraints would be an available option, but it is not clear which equations are to be substituted and a loss of accuracy might result. To solve this issue, the idea is to introduce in the system each additional equation with associated an unknown Lagrange multiplier Λ, which will render the boundary element system well balanced and force the solution to respect mass conservation for any value of the viscosity ratio, λ. We consider the following Lagrangian functional

$$\mathcal{L} = \frac{1}{2}\boldsymbol{x}^T\boldsymbol{A}\boldsymbol{x} - \boldsymbol{x}^T\boldsymbol{b} + \boldsymbol{\Lambda}^T(\boldsymbol{C}\boldsymbol{x}), \tag{3.107}$$

where the first two terms in $\mathcal{L}$ function represent the potential energy of the unconstrained system, while the last term represents the energy needed to maintain the constraints. $\boldsymbol{\Lambda}$ is a vector containing the Lagrange multipliers, one for each interface within the domain Ω. Now, we proceed to minimize $\mathcal{L}$, requiring that its total variation, $\delta\mathcal{L}$, is zero for every possible value of $\delta\boldsymbol{x}$ and $\delta\boldsymbol{\Lambda}$, thus

$$\delta\mathcal{L} = \frac{\partial\mathcal{L}}{\partial\boldsymbol{x}} \cdot \delta\boldsymbol{x} + \frac{\partial\mathcal{L}}{\partial\boldsymbol{\Lambda}} \cdot \delta\boldsymbol{\Lambda} = 0, \tag{3.108}$$

which leads to the following conditions over the gradient of the Lagrangian functional:

$$\frac{\partial\mathcal{L}}{\partial\boldsymbol{x}} = \boldsymbol{0}, \quad \frac{\partial\mathcal{L}}{\partial\boldsymbol{\Lambda}} = \boldsymbol{0}. \tag{3.109}$$

By imposing the conditions above, we produce a new linear system, which incorporates the desired constraints:

$$\begin{bmatrix} \boldsymbol{A} & \boldsymbol{C}^T \\ \boldsymbol{C} & 0 \end{bmatrix} \begin{bmatrix} \boldsymbol{x} \\ \boldsymbol{\Lambda} \end{bmatrix} = \begin{bmatrix} \boldsymbol{b} \\ \boldsymbol{0} \end{bmatrix}. \tag{3.110}$$

This method is of easy implementation and, since usually the boundary element matrix is dense, it does not destroy an eventually banded form of the final matrix. However, the size of the matrix increases and this can become undesirable when a large number of interfaces is present.

3.7.7 Physical interpretation of the Lagrange multiplier

In order to describe the physical meaning of the Lagrange multiplier $\mathbf{\Lambda}$, we reconsider a slightly modified, but more general, version of equation (3.104):

$$\int_{\partial\Omega} \boldsymbol{u} \cdot \boldsymbol{n} \, dS = \dot{q}^*, \tag{3.111}$$

which assigns a generic value to the flow rate across the target boundary. The relation (3.111) can be readily discretized in

$$\boldsymbol{C}\boldsymbol{x} = \boldsymbol{q}, \tag{3.112}$$

where the right hand side $\boldsymbol{q}$ takes into account possible flow of fluid through the boundary $\partial\Omega$.

The Lagrangian functional now takes the form:

$$\mathcal{L} = \frac{1}{2}\boldsymbol{x}^T\boldsymbol{A}\boldsymbol{x} - \boldsymbol{x}^T\boldsymbol{b} + \mathbf{\Lambda}^T(\boldsymbol{C}\boldsymbol{x} - \boldsymbol{q}) = \mathcal{E}(\boldsymbol{x}, \boldsymbol{q}) + \mathbf{\Lambda}^T(\boldsymbol{C}\boldsymbol{x} - \boldsymbol{q}), \tag{3.113}$$

with $\mathcal{E}(\boldsymbol{x}, \boldsymbol{q})$ the *energy* associated with the boundary element linear system. Deriving the Lagrangian with respect to $\boldsymbol{q}$ we obtain:

$$\frac{\partial\mathcal{L}}{\partial\boldsymbol{q}} = \frac{\partial\mathcal{E}}{\partial\boldsymbol{q}} - \mathbf{\Lambda}^T, \tag{3.114}$$

and stationarity implies that

$$\frac{\partial\mathcal{E}}{\partial\boldsymbol{q}} = \mathbf{\Lambda}^T, \tag{3.115}$$

i.e. the Lagrange multiplier Λ represents the sensitivity of the *energy* $\mathcal{E}$ of the system with respect to variations in the mass flow rate through the contour $\partial\Omega$.

3.8 Single phase flow validation

Since the boundary element computer code used in the present study has been developed "*ad hoc*", an extensive validation campaign is mandatory in order to test the predictive capabilities of the software. The single phase validation has an important role since it is the first benchmark for the numerical integration of the discrete single-layer and double-layer operators, which are to be used also in the two-phase computations, and the linear system assembling.

We have selected to test the code with the pioneering work by Luchini et al. [1991], who first computed the protrusion heights for a series of wall textures composed by a periodic array of riblets of known shape. In this case, there is no gas filling the cavities, so we can refer to these simulations as pertaining to a fully wetted, Wenzel state. In their work, Luchini and co-workers computed the values of the protrusion heights employing a boundary element method, aimed to numerically solve a set of Laplace equations, coming form the longitudinal and transverse problem, where the latter were reformulated in term of vorticity and stream function.

The riblets shape considered is not particularly complicated and it is given in terms of the following analitycal functions:

- co-sinusoidal profile, $y(x) = \frac{2s}{\pi}x^2 - 4sx$,
- parabolic profile, $y(x) = \pi s(\cos(x) - 1)$,

where s is a parameter which tunes the depth of the protrusion, while the periodicity b of the grooves has been taken equal to 2π. Since the periodicity is not unitary, the results are presented in term of ratio between the value of the protrusion height. The simulations' strategy is based on the discretization of the boundary with an adequately large number of spline elements and the calculation of the velocity at some height $y = H$ far enough from the wall boundary. In all of our simulations, $H = 10b$ is used if not stated otherwise, which permits to avoid any boundary effect on the velocity distribution. There are no additional computational cost in defining the upper boundary, where the velocity is measured, far from the riblet since the inside of the domain is not meshed with the BEM. The results are reported together with the reference case in figure 3.8. We find excellent agreement between our simulations and the results reported by the selected reference, with a percentage error always within 1%. The values of the protrusion heights are, as expected, dependent on the riblet's geometry and tend to an asymptotic value along with the wall penetration $s \to \infty$. This is a very important physical result, since the level of slippage generated at wall has an upper bound that cannot be overcome, for any given geometry. It is worth to note that, in theory, the best possible riblets' configuration are a series of equispaced, infinity deep grooves, known as blades. In this case, an analytical solution for the protrusion heights (normalized with respect to the periodicity) can be found and it is determined to be $h_{||} = \pi^{-1}\log 2$, while $h_{\perp} = \frac{1}{2\pi}\log 2$, which is exactly equal to $\frac{h_{||}}{2}$ [Luchini et al., 1991].

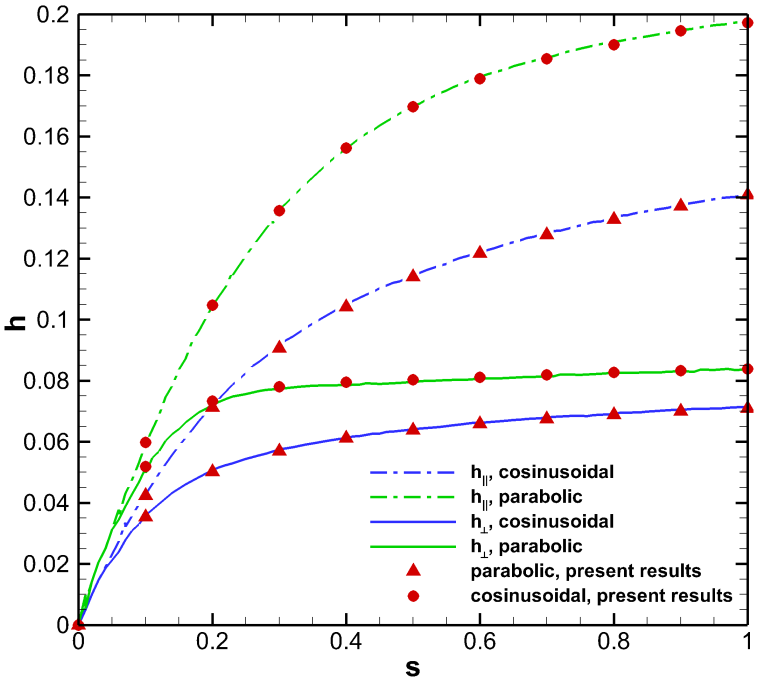

Figure 3.8: Computed protrusion heights normalized by the riblet's periodicity.

3.9 Fractal riblets

Whether one considers random roughness or regular nano-structuring of the surface texture, it appears appropriate to start by examining the properties of fractal surfaces. The application of fractals to characterize rough surfaces dates back to the eighties Mandelbrot et al. [1984], Gagnepain and Roques-Carmes [1986], Frederick [1987], upon the recognition that many rough surfaces demonstrate self-similar properties to some extent and over a certain range of scales. Today, etching techniques (plasma, laser, electrochemical), litography (photo, X-ray, etc.), deposition and other approaches are routinely used to micro- and nano-texture surfaces for applications ranging from MEMS to magnetic storage devices.

In this section, we take advantage of the boundary element method to compute the protrusion heights for Koch-like riblets which iteratively protrude either toward the fluid region or cave in at the wall. The microscopic, near-wall configuration which we have considered consists of regular triangular groove (see figure 3.9, left frames). The sides of the triangle are taken of equal length and the angle at the base, α, is taken equal to either 45^o, 60^o, 90^o or 120^o. The first fractal iteration, second column in the figure, is achieved by dividing each side of the triangle into three segments and inserting an isoscope triangle (of same vertex angle α) in place of the central segment, so that each segment of the newly created fluid-solid has equal length. The newly rough boundary created can either protrude towards the fluid (top row) or contract at the wall (bottom row). Figure 3.9 shows the first three iterations of the process, which yields what is known as the Koch curve for the case $\alpha = 60^o$. The angle α defines also the fractal dimension of each curve, characterizing its magnification.

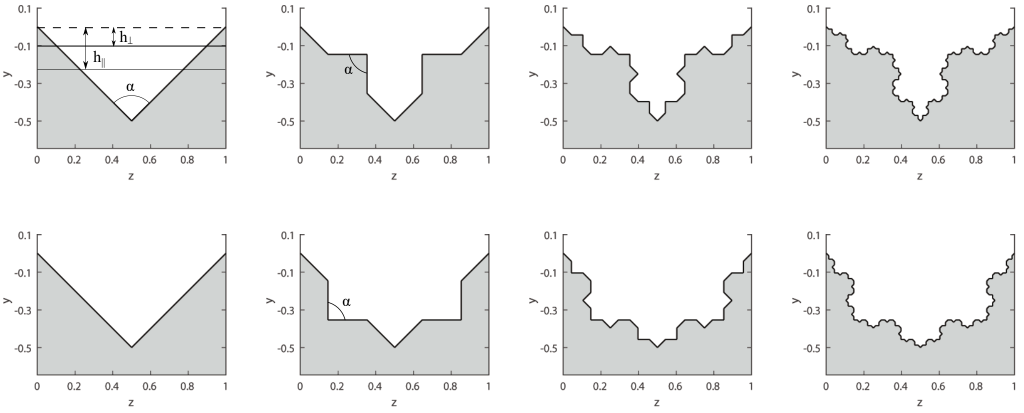

Figure 3.9: Iterative process in the construction of fractal riblets, for both outward (top row) and inward moving curves.

In fact, at each step of the iterative procedure, each line segment is replaced by $N = 4$ segments of equal length, with each self-similar copy $\dfrac{1}{S_\alpha} = \dfrac{1}{2\left(1 + sin\frac{\alpha}{2}\right)}$ as log as the original. The Housdorff dimension is $D_\alpha = \dfrac{\log(N)}{\log(S_\alpha)}$, irrespective of whether the wall sticks further out in the course of the iterations or caves in. For the cases considered here it is $D_{45} = 1.3629$, $D_{60} = 1.2619$, $D_{90} = 1.1290$, $D_{120} = 1.0526$. The fractal dimension D_α cannot, alone, characterize the surface completely; however, we will see later that for inward moving surfaces (bottom row of figure 3.9) the amount of drag reduction increases with D_α.

For each one of the wall textures shown in figure 3.9, the Stokes equation is solved in the fluid region, up to some wall units above the surface, on account of the physics of the near-wall turbulent problem which is dominated by viscous forces. The inner problem decouples into two set of equations, one for the longitudinal flow and one for the cross flow, as described by Luchini et al. [1991]. For the sake of brevity the equations and the boundary conditions are not reported here; it suffices to say that the results of the two decoupled problems yield $h_\parallel$ and $h_\perp$, given that, on a grooved surface, the asymptotic behavior of the velocity vector far from the surface has the form Crowdy [2010]:

$$(u, v, w) = (y + h_\parallel, 0, y + h_\perp), \tag{3.116}$$

with u, v and w respectively the streamwise, wall-normal and spanwise velocity components. The two protrusion heights are drawn (qualitatively) in the top left frame of figure 3.9, and are measured with reference to the (arbitrary) origin of the y-axis.

The numerical solution of the microscopic equations is carried out in a domain of spanwise dimension equal to one, and vertical dimension sufficiently large for the asymptotic solution to be established (the upper boundary can safely be taken at $y = 4$). It is accomplished by a boundary element method Alinovi and Bottaro [2018], extensively validated against results in the literature.

The calculation of the slip lengths takes advantage of the asymptotic relations

(3.116) for the velocity fields, which are directly measured by our numerical code on a auxiliary patch located far enough from the riblet at some distance $y = y^*$. The estimation of the protrusion heights is thus obtain simply by the formula $h_{||} = u/y^*$ and similarly for the transverse case.

Examples of numerical results are given in figure 3.10. The iso-colors in the figure define the streamwise velocity (which arises from the solution of a Laplace equation for u [Bechert and Bartenwerfer, 1989]), whereas the streamlines (with arrows) represent the secondary velocity vector, (v, w), stemming from the solution of a two-dimensional Stokes problem in the (y, z) plane [Luchini et al., 1991]. A larger secondary vortex appears in the image in the right frame, a feature associated to larger values of both protrusion heights.

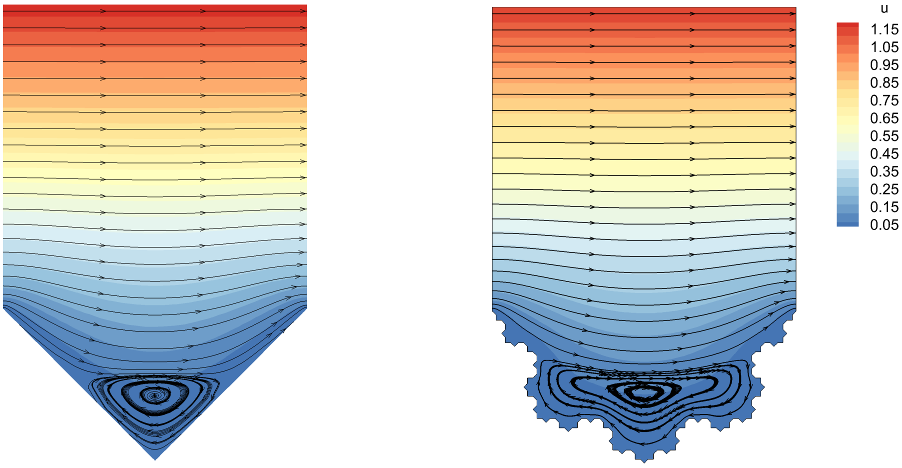

Figure 3.10: Numerical solutions for the base configuration with $\alpha = 90^o$ (left frame) and for the third, inward moving iterate. The colors refers to the streamwise velocity component, u, while the lines with arrows are streamlines of the secondary, (v, w), flow.

The distances $h_{||}$ and $h_\perp$ define virtual walls for, respectively, the longitudinal and transverse velocity profiles. The significant length scale, independent of the choice of the origin, is however Δh, displayed in figure 3.11; the figure shows that Δh increases as the wall moves inwards (triangular symbols) for all α's. By the third iteration the results are essentially converged and further iterations on the fractal curve produce negligible modifications of Δh for both the "i" and the "o" cases. The variation in Δh between the initial configuration (it = 0) and the last iteration (it = 3) quantifies, for each opening angle, α, the additional drag reduction which we might expect when using fractal riblets (as by eq. (1)). Such a variation is equal to 4% when $\alpha = 45^o$, 7% when $\alpha = 60^o$, 17% when $\alpha = 90^o$, and to almost 31% when $\alpha = 120^o$. Thus, the least efficient riblets (the triangular ones, with vertex angle $\alpha = 120^o$) are those which have the most to gain by hierarchical micro- and nano-structuring. When α is equal to 45^o we have the best results among all cases considered, in terms of drag reduction, but it is likely that even better results can be obtained by reducing α or increasing D_α as figure 3.11(b) suggests. It is important to stress, however, that the *best* results found here are not the absolute best results which could be found; it is possible, for example, that hierarchically nano-structured blade-riblets yield even larger values of Δh. The search for the *optimal* riblet shape is left for future work.

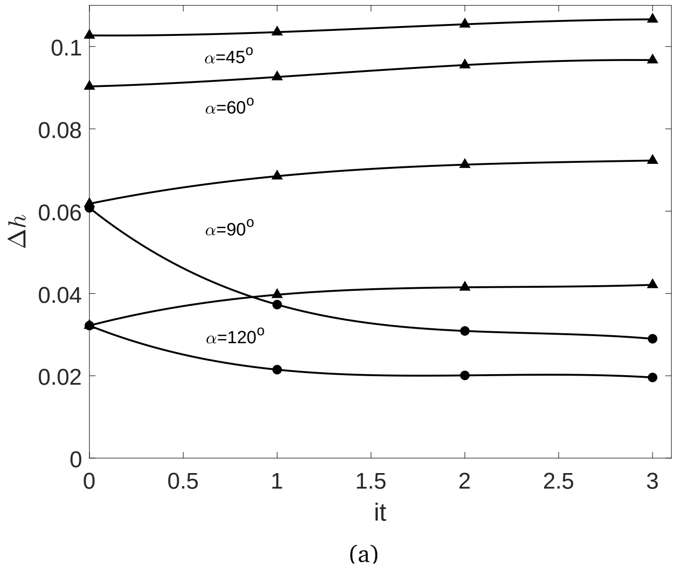

(a)

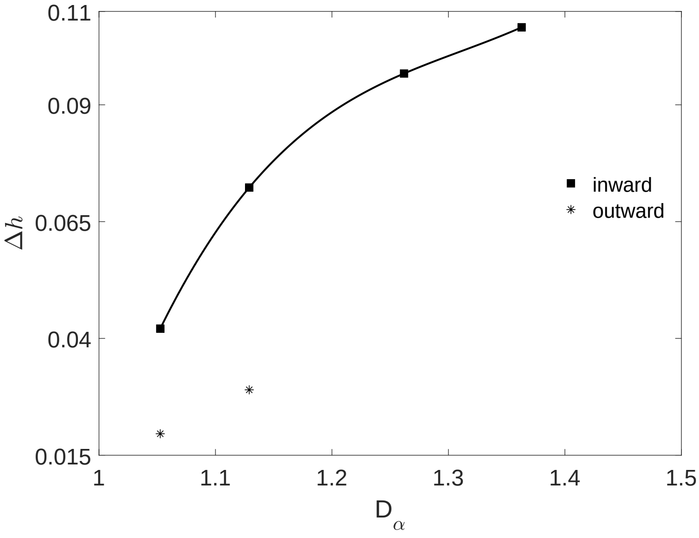

(b)

Figure 3.11: Protrusion height difference for all the cases considered, as function of the fractal iteration (a) and as function of the fractal dimension for $it = 3$ (b).

The results in terms of protrusion heights for both inward ("i") and outward ("o") moving surfaces are reported in Table 1, for the base configuration (indicated by "it = 0") and up to the third iteration. The outward protruding results for the case $\alpha = 45^o$ and $\alpha = 60^o$ are not present in the table (nor in the following figure 3.11(a)) because the vertices of the triangles added in the first iteration touch one another, creating two disconnected fluid regions.

Angle		$h_{\|\|}$					$h_\perp$			
		0	1	2	3	it	0	1	2	3
$\alpha = 45°$	"i"	0.1842	0.1851	0.1872	0.1885		0.0815	0.0816	0.0818	0.0819
$\alpha = 60°$	"i"	0.1706	0.1733	0.1762	0.1775		0.0803	0.0806	0.0807	0.0808
$\alpha = 90°$	"i"	0.1396	0.1464	0.1495	0.1506		0.0778	0.0779	0.0782	0.0783
	"o"	0.1396	0.1117	0.0989	0.0949		0.0788	0.0744	0.068	0.0659
$\alpha = 120°$	"i"	0.1026	0.1112	0.1138	0.1146		0.0704	0.0715	0.0723	0.0725
	"o"	0.1026	0.0819	0.0755	0.0737		0.0704	0.0604	0.0554	0.0541

Table 3.2: Protrusions heights, scaled by the spanwise periodicity b of the grooves.

3.10 Two phase flow validation

The two phase flow validation has been conducted in a more intensive way. We have selected a series of benchmark test cases taken from the literature, involving different types of problems. The test are aimed to validate the both Stokes and Laplace solver, with a special attention to the problem of the mass conservation occurring in a standard BEM, as discussed in [Alinovi and Bottaro, 2018].

3.10.1 Relaxation of a two dimensional droplet

We start by studying the relaxation of a two dimensional droplet from an ellipse of given aspect ratio, as show in figure 3.12. We assume that the droplet, initially at rest, lies in an infinite free space filled with a different fluid. The droplet will start to contract, under the effect of surface tension, until a circular shape is reached. During the droplet's contraction, the evolution of the semi-major axis a is monitored, up to the steady state.

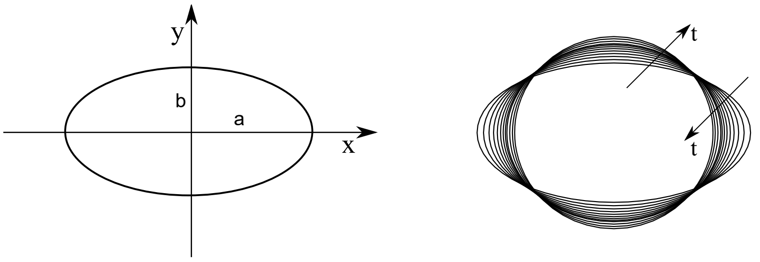

Figure 3.12: An elliptic droplet deforming into a circle. The right figure shows the evolution of the interface in time.

In order to perform this study we take advantage of the free space Green's function and its associated stress tensor, which read

$$G_{ij}(\boldsymbol{x}, \boldsymbol{x}_0) = -\delta_{ij} log(r) + \frac{\hat{x}_i \hat{x}_j}{r^2}, \quad T_{ijk}(\boldsymbol{x}, \boldsymbol{x}_0) = -4\frac{\hat{x}_i \hat{x}_j \hat{x}_k}{r^4}, \tag{3.117}$$

where r is the distance between the points $\boldsymbol{x}$ and $\boldsymbol{x}_0$, while $\hat{x}_i = x_i - x_{0_i}$.

Regarding the boundary integral formulation, we note that this case corresponds to solving the system

$$\Big[(\lambda - 1)\boldsymbol{D}^{II} + \frac{1+\lambda}{2}\boldsymbol{I}\Big]\Big[\boldsymbol{u}\Big] = -\boldsymbol{S}^{II}\Delta \boldsymbol{f}^{I}, \tag{3.118}$$

for the interfacial velocity $\boldsymbol{u}$, with the unit normal vector pointing outside of the droplet. We can force the system to respect the mass conservation constraint following the formulation in equation (3.110). Since in this case we have only one interface, the matrix $\boldsymbol{C}$ degenerates to a single equation, and, in practice, only one line and one column must be added to the original linear system.

For this problem we consider three different values of the viscosity ratio, $\lambda = \frac{1}{10}, \frac{1}{20}, \frac{1}{100}$, and three different values of the capillary number, $Ca = 0.1, 1, 10$, which tunes the rigidity of the interface and the velocity of the relaxation. Since the aspect ratio of the ellipse is $\frac{a}{b} = 2$, we aspect that, after a transient, the fluid interface assumes a circular shape with radius equal to $\sqrt{2}$ (provided b is initially set to one). For this simulation we use 60 spline elements and employ a fixed time step $\Delta t = 0.01$ for the lower capillary number, while $\Delta t = 0.05$ for the others. The number of elements is selected in order to obtain a good matching with respect to the steady state radius of the droplet (here we obtain a value close to the theoretical one, up to the fourth decimal place). However, a lower number of elements would be equally satisfactory, since the spline elements are very suitable to discretize curved boundaries. The time step is selected in order to have a stable time evolution of the interface, which could in principle suffer of numerical instability due to the explicit scheme used. Its influence on the simulations is negligible since the Stokes equation is being solved under the quasi-steady approximation. We have validated our implementation (without the Lagrange multiplier approach) against the code written by Pozrikidis and publicly available with the library *BEMLIB* Pozrikidis, finding indistinguishable differences between the results of the two codes. In the following we will call this latter method the *standard* approach, to distinguish it from techniques which enforce continuity explicitly, including the original one developed in the course of this thesis work.

The results, reported in figure 3.13 and 3.14, compare the evolution of the semi-major axis, a, in time for both the Lagrange multiplier approach and the standard formulation. Even if the initial transient path is similar, we note (symbols) a continuous decrease of the semi-axis a after the droplet has reached the circular shape. The effect of this mass loss is enhanced as the viscosity ratio and the capillary number become smaller. Imposing the constraint (3.104), the radius of the droplet remains constant in time, when t is sufficiently large, and equal to $\sqrt{2}$ for all the values of λ and Ca tested.

In section 3.7.6, we have mentioned the possibility to modify the expression of the double-layer potential to satisfy mass conservation for all possible values of λ [Pozrikidis, 2001]. We have thus performed again the simulations implementing in our code the proposed deflation correction and have compared the results with the Lagrange multiplier approach, obtaining a very good agreement between the two methods, as shown in figure 3.15. This agreement corroborates the validity of our approch. However, as will be shown in the next cases treated, we have found that the method of Lagrange multipliers yields better performance in term of mass conservation. Focusing on the normal velocity along the interface, we take its maximum absolute value as a convergence indicator. If the problem admits a steady state solution, the interface should assume a position such that the maximum normal velocity vanishes. The comparison between the methods is shown in figure 3.16. We observe that the maximum normal velocity decreases until reaching a *plateau*, whose value is dependent on the number of element used to discretize the droplet and goes down as the number of elements increases.

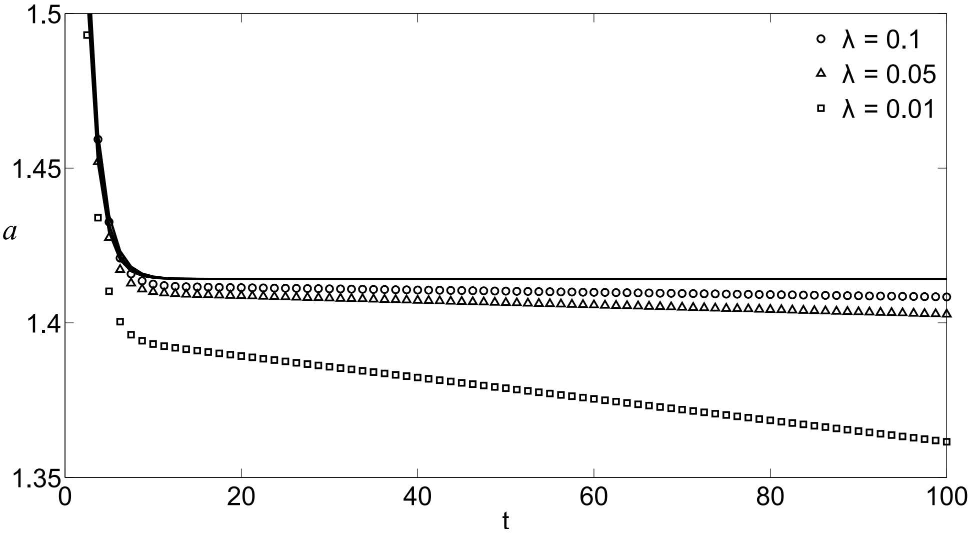

Figure 3.13: Evolution of the major semi-axis of the droplet for different values of λ and $Ca = 0.1$. The solid lines display results obtained with the Lagrange multiplier approach, while the markers refer to the standard BEM formulation, i.e. without explicitly enforcing mass conservation. At steady state, the value of $a = \sqrt{2}$ is correctly rendered by the Lagrange multiplier approach. The initial relaxation of the droplet is independent of the viscosity ratio.

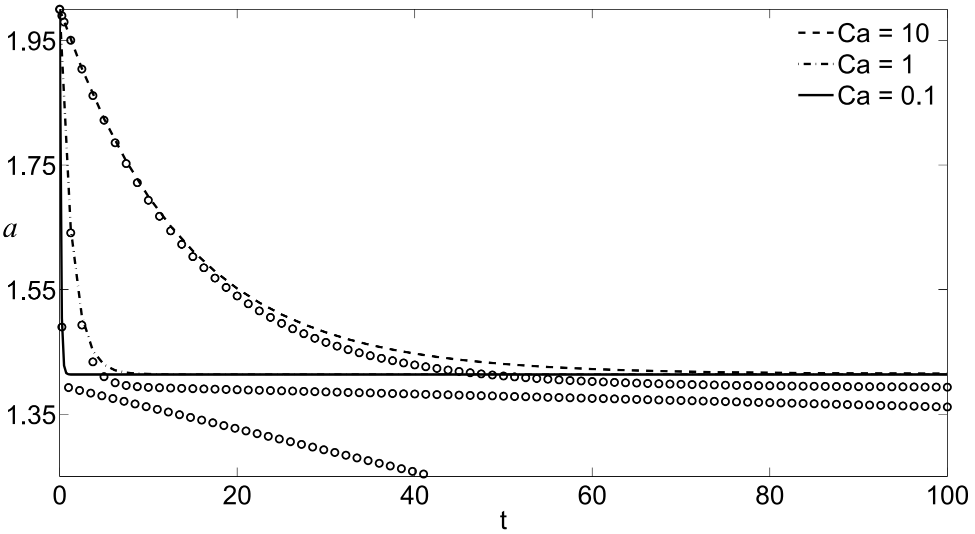

Figure 3.14: Evolution of the major semi-axis of the droplet for $\lambda = 0.01$ at different Ca. The circles denotes the variation of a with time, without using the Lagrange multiplier approach. The initial relaxation of the droplet is slower the larger is Ca, i.e for small surface tension the droplet reaches its final shape in a longer time.

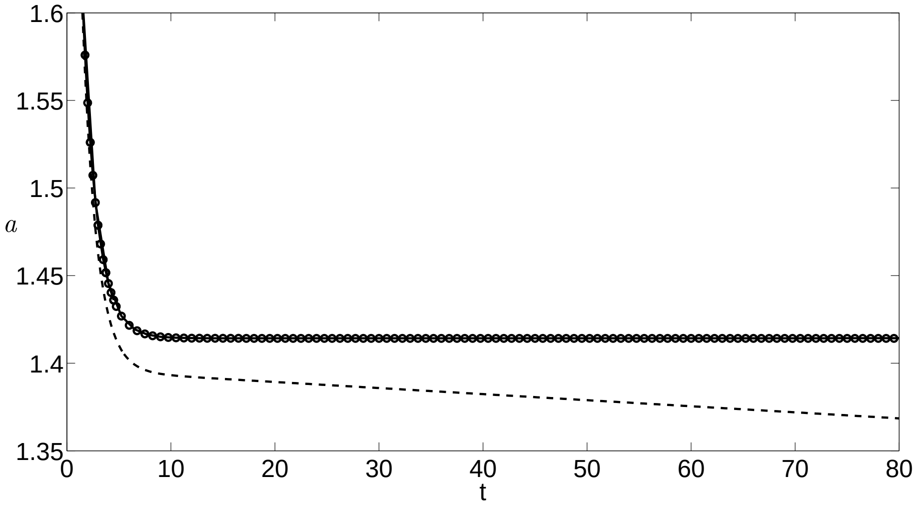

Figure 3.15: Comparison between Lagrange multiplier approach (solid line), deflation approach (empty circles), and standard formulation (dashed line) at $\lambda = 0.01$ and $Ca = 1$

.

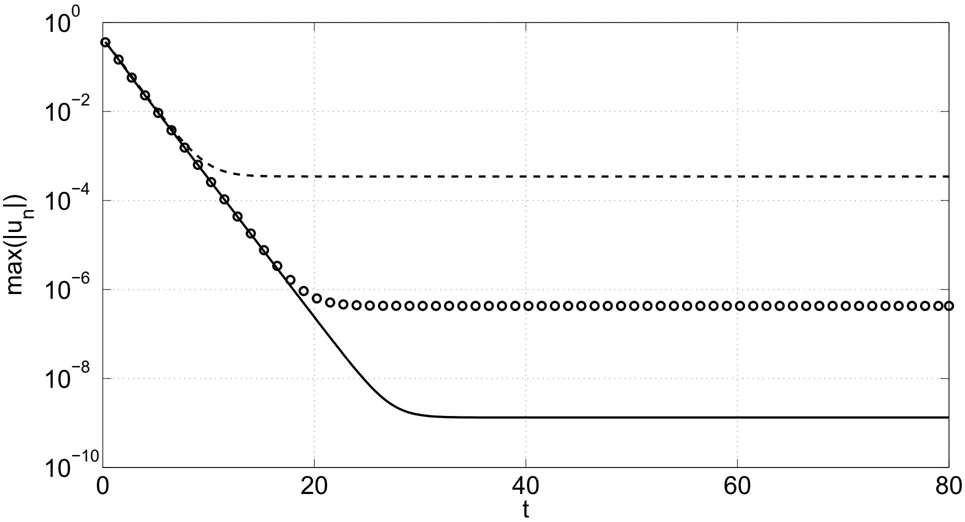

Figure 3.16: Maximum normal velocity history. The dashed line corresponds to the standard (unconstrained) implementation, the line with empty circles corresponds to the deflation approach, while the solid line correspond to the Lagrange multiplier approach.

The Lagrange multipliers approach offers a better performance in minimizing the maximum normal velocity along the droplet's interface at steady state, which is several orders of magnitude lower with respect to the method proposed by Pozrikidis [2001] at the same spatial resolution and time step. We have found out during the simulations that mass leakage depends on the number of elements employed, decreasing with the increase of the resolution. It is worth observing that the problem of mass conservation at low viscosity ratios is intrinsic to the boundary element method and using a large number of elements does not solve the problem at the source. The method described here is more accurate (at any given resolution) and computationally efficient.

3.10.2 Deformation of a droplet under a shear flow

We aim to reproduce the numerical results of a single droplet confined in a channel of height $2H$ and length L, as shown in figure 3.17. The shear flow is generated by the two channel walls, moving at a given velocity U in opposite directions. The reference numerical simulations has been performed by Sheth and Pozrikidis [1994], who have employed for their computations a finite difference code with embedded a volume of fluid method. They conducted a parametric study of the deformation of the droplet by varying the viscosity ratio droplet/outer fluid and the Reynolds number inside the channel. Since our formulation is valid only for the Stokes flows, we refer to the simulation presented in the reference at $Re = 1$, which falls reasonably close to our approximation. The droplet of viscosity μ_d is neutrally buoyant and placed in the middle of a square channel of thickness $2H$, filled with a fluid with viscosity μ_f. The diameter of the droplet, D, is equal to half the channel height. The base flow, u, generated by the applied boundary conditions can be easily calculated analytically and reads

$$u(y) = \frac{U}{H}(y - H), \tag{3.119}$$

where y is the wall-normal coordinate.

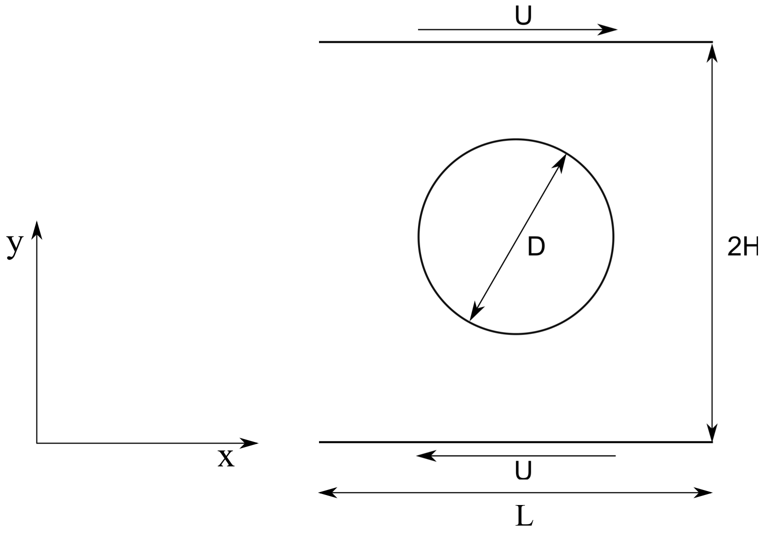

Figure 3.17: Sketch of the numerical experiment of a droplet in a shear flow.

The boundary integral equation is similar to the one employed in the previous section, but this time two walls are in the domain of interest. The effect of the walls can be taken into account by using different approaches. In both cases the Green's function can be selected in order to satisfy the periodicity of the flow, thus avoiding the discretization of the inlet and outlet of the channel. The simplest choice for the flow representation, is to derive the boundary integral equation for the disturbance

velocity generated by the droplet immersed in the flow given by the relation (3.119): this procedure has been adopted by Zhou and Pozrikidis [1993]. In our case, the walls are explicitly taken into account by adding the related single-layer and double-layer potentials. The two approaches are completely equivalent in term of results, but the second approach give raise to similar integral relation with respect to the one discussed in this thesis.
We have selected from the reference work two different cases, involving different viscosity ratios, $\lambda = \frac{\mu_d}{\mu_f}$ and droplet's surface tension σ_s(i.e. capillary numbers), as reported in table 3.3.

Case	λ	Ca
1	1	0.2
2	10	0.4

Table 3.3: Non-dimensional parameters used in present numerical experiments.

Since the flow is steady and anti-symmetric with respect to the half-channel height, the droplet is expected to deform under shear stresses acting on its surface and to reach a well defined deformed configuration. Even in this case, the agreement with the literature is very good, with the droplet fitting perfectly the shape found by Sheth and Pozrikidis [1994].

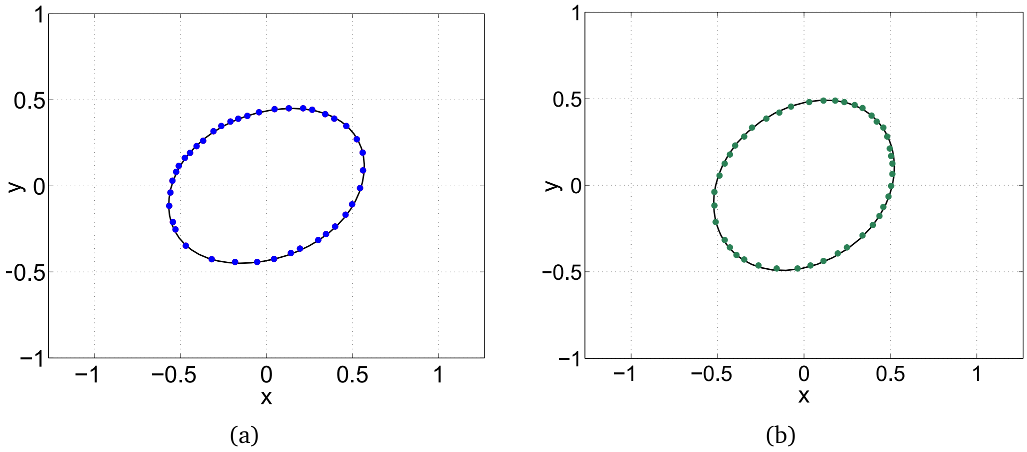

Figure 3.18: Deformation of a droplet in a shear flow. The solid lines are the computed shapes for case 1 (a) and case 2 (b), while the colored dots are the shapes computed by Sheth and Pozrikidis [1994].

3.10.3 Relaxation of a pinned interface

For this numerical example, we consider a simple cavity bounded by three walls of length L and a fluid interface, pinned at the corners of the cavity, as sketched in figure 3.19. The initial shape of the interface is a cosine wave of equation $y_0(x) = b\cos(\frac{2\pi}{L}x) - b$, where b is a constant. Similarly to the droplet's case, the surface tension between the two fluids induces the motion of the interface, which experiments a transition from the initial shape to a prescribed shape, analytically available under the hypothesis of small amplitude deflection of the interface. The Young-Laplace equation, expressed for convenience in non-dimensional form, is

$$\frac{d^2y}{dx^2}\Big[1 + \Big(\frac{dy}{dx}\Big)^2\Big]^{-\frac{3}{2}} = C_1, \tag{3.120}$$

with $C_1 = \Delta P$ the non-dimensional pressure jump across the interface and y the vertical displacement of the interface. If the curvature of the interface is small enough, the term in brackets in equation (3.120) tends to one, leading to the following approximate solution

$$y(x) = \frac{C_1}{2}x(x - L), \tag{3.121}$$

after imposing the boundary conditions

$$y(0) = 0, \quad y(L) = 0. \tag{3.122}$$

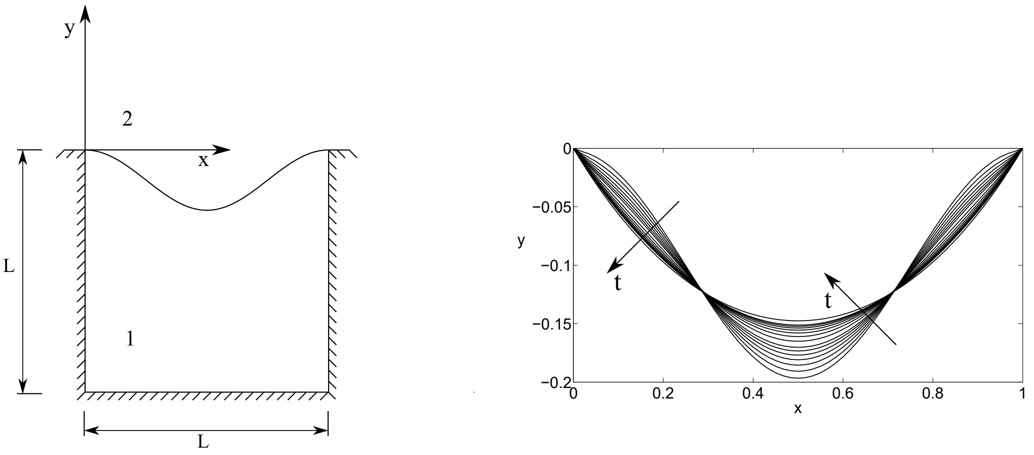

Figure 3.19: Sketch of the cavity with a wavy interface (left), and successive positions assumed by the interface during its relaxation into a parabolic shape (right).

Particular attention should be payed to the constant C_1: since the pressure difference across the interface is not known *a priori*, its value can be calculated imposing the conservation of mass inside the cavity through the relation:

$$\int_0^L y_0 dx = \int_0^L y_f dx, \tag{3.123}$$

which yields $C_1 = \frac{12b}{L^2}$. In order to obtain more precise results, equation (3.120) can be solved without approximation using standard iterative techniques.

For this simulation, we have employed 60 elements to discretize each edge of the cavity and the interface. We have set a constant time step $\Delta t = 10^{-3}$ for $Ca = 0.1$, while $\Delta t = 10^{-2}$ for the lower values of Ca. The fluid in both the domains is initially at rest and the interface moves as an effect of the surface tension. Periodic boundary condition are applied to left and right boundaries by using the following Green's function [Pozrikidis, 2002]:

$$\begin{aligned} A(\hat{\boldsymbol{x}}) &= \frac{1}{2}\log\{2[\cosh(\omega\hat{x}_2) - \cos(\alpha\hat{x}_1)]\}, && (3.124)\\ G_{11} &= -A(\hat{\boldsymbol{x}}) - \hat{y}\frac{\partial A(\hat{\boldsymbol{x}})}{\partial\hat{y}} + 1, && (3.125)\\ G_{12} &= \hat{y}\frac{\partial A(\hat{\boldsymbol{x}})}{\partial\hat{x}}, && (3.126)\\ G_{22} &= A(\hat{\boldsymbol{x}}) + \hat{y}\frac{\partial A(\hat{\boldsymbol{x}})}{\partial\hat{x}}, && (3.127) \end{aligned}$$

where $\hat{\boldsymbol{x}} = \boldsymbol{x} - \boldsymbol{x}_0$ and $\alpha = \frac{2\pi}{L}$. The components of the stress tensor $\boldsymbol{T}_{ijk}$ are:

$$T_{111} = -4\frac{\partial A(\hat{\boldsymbol{x}})}{\partial\hat{x}} - 2\hat{x}_2\frac{\partial^2 A(\hat{\boldsymbol{x}})}{\partial\hat{x}\partial\hat{y}}, \quad T_{112} = -2\frac{\partial A(\hat{\boldsymbol{x}})}{\partial\hat{y}} - 2\hat{x}_2\frac{\partial^2 A(\hat{\boldsymbol{x}})}{\partial\hat{y}\partial\hat{y}}, \qquad (3.128)$$

$$T_{212} = 2\hat{x}_2\frac{\partial^2 A(\hat{\boldsymbol{x}})}{\partial\hat{x}\partial\hat{y}}, \quad T_{222} = -2\frac{\partial A(\hat{\boldsymbol{x}})}{\partial\hat{y}} + 2\hat{x}_2\frac{\partial^2 A(\hat{\boldsymbol{x}})}{\partial\hat{y}\partial\hat{y}}, \qquad (3.129)$$

with no need to specify the missing components of $\boldsymbol{G}_{ij}$ and $\boldsymbol{T}_{ijk}$ since they are symmetric tensors.

In this case, we monitor the volume of the fluid trapped between the cavity walls and the interface, given, at each time, by the following integral relation

$$V = \int_{\Omega_1} dS = \frac{1}{2}\int_{\Omega_1} \nabla\cdot\boldsymbol{x}\,dS = \frac{1}{2}\int_{\partial\Omega_1} \boldsymbol{x}\cdot\boldsymbol{n}\,dl, \qquad (3.130)$$

which is integrated in the same fashion as other integral quantities. The results, reported in figures 3.20 and 3.21, shown a similar behavior to that observed in the droplet relaxation benchmark. The total mass inside the cavity is not conserved in time and mass leakage becomes larger as the capillary number and the viscosity ratio become smaller. The usage of the deflation approach (3.101) turns out to be not as effective as in the previous case and the mass leakage (or creation) persists, even if with a lower growth rate, as shown in figure 3.23. Instead, the Lagrange multiplier approach leads to very satisfactory results, maintaining constant the mass inside the pocket and fitting the theoretical steady-state position of the interface prescribed by equation (3.120) for every test value of λ and Ca, as shown in figure 3.22 for a representative case.

Additional features arise from the analysis of the maximum absolute value of the normal velocity along the interface during the relaxation process, shown for a representative set of parameters in figure 3.24. We note that the standard boundary element formulation is unstable: the initial decrease in the maximum value of the normal velocity is followed by an increase. This phenomenon brings, sooner or later, to the divergence of the simulation, with the interface breaking down anomalously. The double-layer deflation seems to counteract this undesirable effect, but it presents some difficulties in bringing down the maximum normal velocity below a reasonably low value. Again, the Lagrange multiplier approach gives us the best result, yielding a much better convergence with respect to the other methods tested.

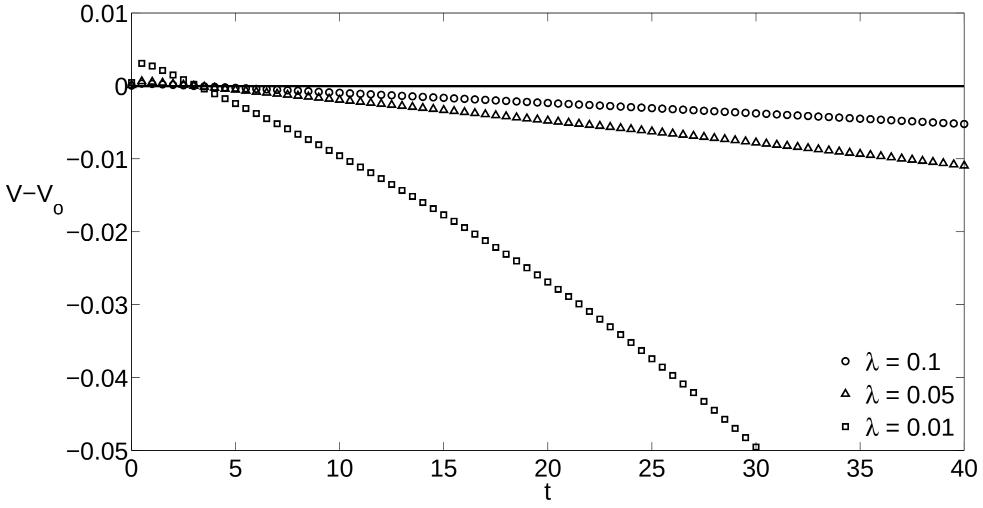

Figure 3.20: Time variation of the volume of fluid contained inside the cavity (V_0 is the initial value) for different values of λ and $Ca = 0.1$. The loss of fluid within the cavity is enhanced as the viscosity ratio λ decreases. The solid line represents the mass variations in time for the same cases when using the Lagrange multiplier approach.

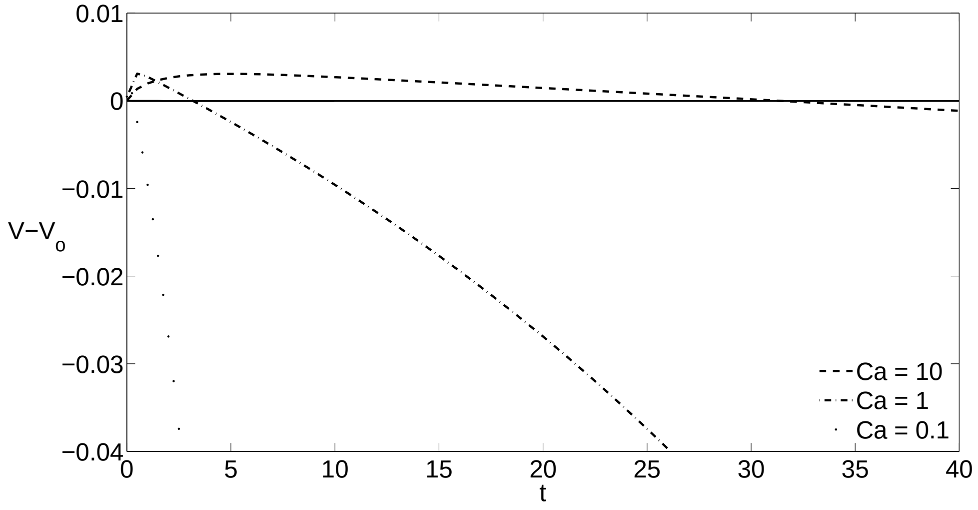

Figure 3.21: Time variation of the volume of fluid contained inside the cavity for different values of Ca and $\lambda = 0.01$. The loss of fluid within the cavity is enhanced by a decreasing value of Ca. The solid line represents the mass variations in time for the same cases when using the Lagrange multiplier approach.

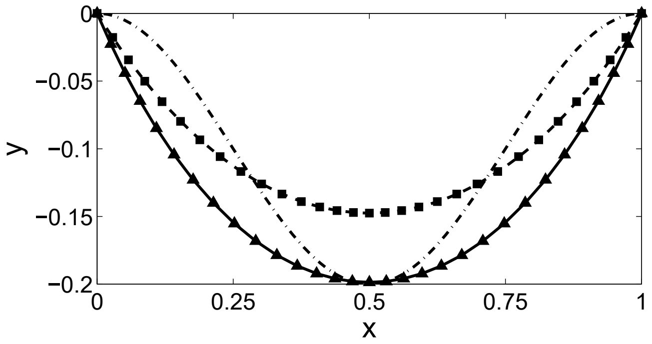

Figure 3.22: Position assumed by the interface starting from a co-sinusoidal shape (.− line) for $\lambda = 0.05$ and $Ca = 0.1$. The $-\blacktriangle$ line represents the computed position for the standard boundary element implementation at $t = 10.5$, while the solid squares represent the final steady solution with the Lagrange multiplier correction which, at the same instant of time, agrees with the theoretical solution given by equation (3.121) (dashed line).

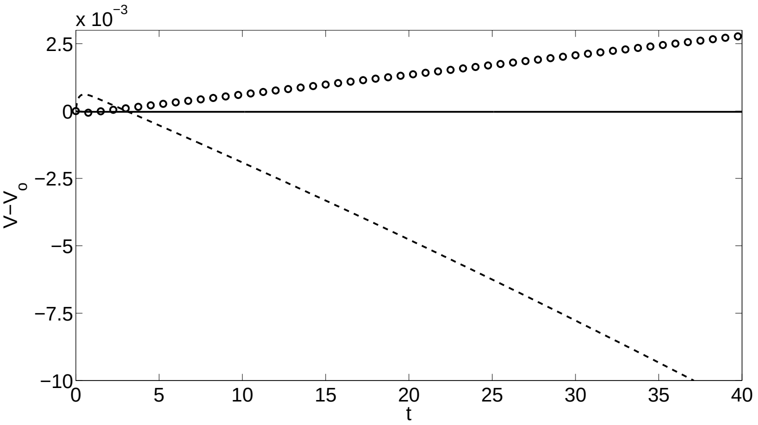

Figure 3.23: Comparison between standard implementation (dashed line), double layer deflation (empty circles) and Lagrange multiplier approach (solid line), for $\lambda = 0.05$ and $Ca = 1$.

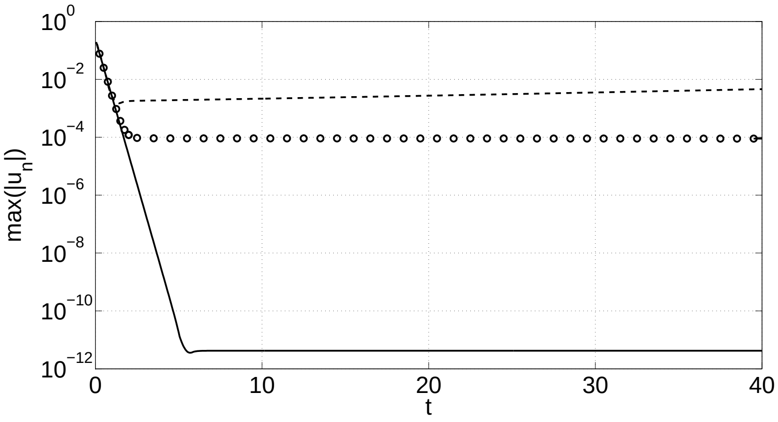

Figure 3.24: Maximum normal velocity along the interface for $\lambda = 0.01$ and $Ca = 1$ for the standard boundary element implementation (dashed line), double-layer deflation (empty circles) and Lagrange multiplier approach (solid line).

It is also interesting to compare the results obtained using the boundary element method with a standard *Volume of Fluids* method (VoF) implemented with the finite volume framework provided by openFOAM [2015]. The VoF method was introduced firstly by Hirt and Nichols [1981] and it is based on defining an indicator function, called volume fraction, bounded between $[0, 1]$. The extremities of the interval are associated to the two fluids, while the interface is found in the cell with values between 0 and 1.

This approach is widely used to compute multiphase flows, but it is well know to suffers of the undesired phenomenon known as *parasitic currents* [Harvie et al., 2005]. This numerical issue consists in the generation of non-physical velocities near the fluid interface and the phenomenon becomes very significant in the presence of surface-tension-dominated flows. If the magnitude of these velocities is not very large, the method is able to capture the interface with satisfactory accuracy, eventually generating small oscillations of the volume fraction, but the flow fields will result unclean. To underline this fact, we can look at the velocity magnitude inside the fluid domain at steady state, as shown in figure 3.25. For the finite volume computation, we have used a fine Cartesian mesh, with a spacing between the grid points of $\frac{1}{300}$, over which the Stokes equation are solved. The viscosity ratio is set to $\lambda = 0.018$ and the capillary number is $Ca = 0.1$, based on the velocity scale $u_{ref} = \frac{\nu_2}{L}$. We can clearly see how the VoF produces significant velocities in the proximity of the interface, which persist in time, while the boundary element method does not suffers of this unwanted phenomenon.

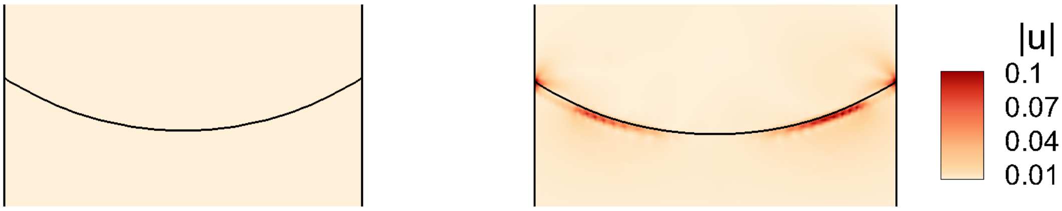

Figure 3.25: Absolute velocity iso-surfaces in the proximity of the interface for the problem sketched in figure 3.19 using BEM with Lagrange multiplier correction (left) and VoF (right).

3.10.4 Flow over superhydrophobic surfaces: comparison with existing results

The flow over superhydrophobic surfaces has been extensively studied from both a theoretical and numerical point of view, assuming that on the interface a perfect slip applies. This is a reasonable hypothesis only in the case of a very small viscosity ratio between the working fluid and the lubricant fluid. The validations pass through different works available in literature, involving both the longitudinal and the transverse flows. The first important comparison to be done is with respect to the analytical formula found by Philip [1972], who has given the exact value of the protrusion heights for a wall composed by alternating stripes with slip/no-slip boundary condition, aligned and perpendicular to the flow direction, by using conformal mapping. This type of wall pattern mimics an idealized super-hydrophobic surface with a flat and infinitely rigid interface. The analytical formula for the protrusion heights, given in function of the solid fraction $\phi_s = 1 - \dfrac{w}{b}$ reads

$$\frac{h_{||}}{b} = \frac{1}{\pi}\log(\sec\left[\frac{\pi}{2}(1-\phi_s)\right]), \quad h_\perp = \frac{h_{||}}{2}. \tag{3.131}$$

We selected three different values of ϕ_s, equal to $0.25, 0.50, 0.75$ respectively and the results, shown in figure 3.26, are extremely close with respect the theoretical values.

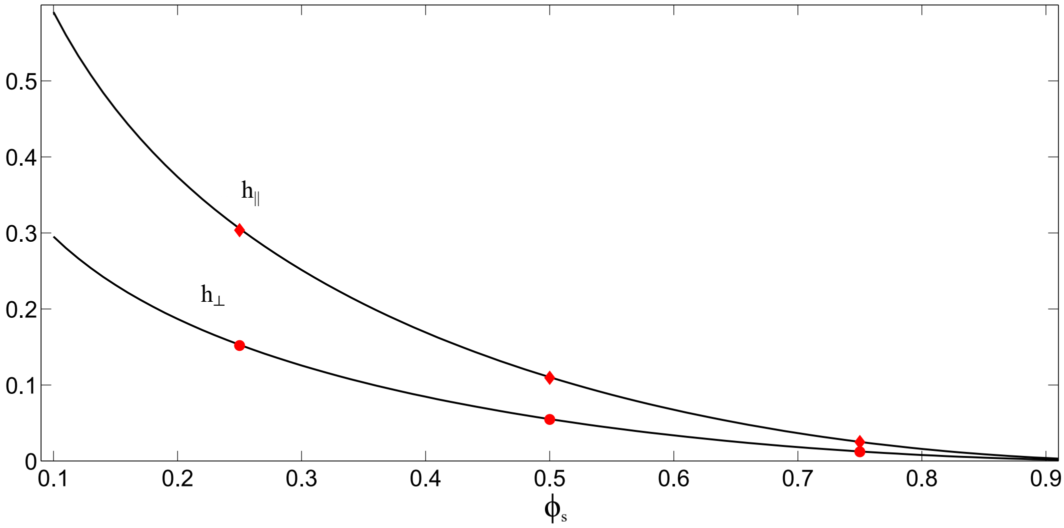

Figure 3.26: Comparison between the protrusion heights calculated by Philip [1972], in solid lines, and the present calculations shown with red symbols.

An extension to Philip's works has been done recently by Crowdy [2010] and by Davis and Lauga [2009], who found a semi-analytical formula for the longitudinal and traverse protrusion heights respectively, including the effect of the curvature of the interface. They considered a circular shape of the interface for both the protruding and the depressing interface case. This is a good approximation that turns out to be exact only in the case of protruding interface in the presence of a sufficiently small capillary number, that makes the interface rigid. In the case of a depressing bubble, the circular shape is in principle not correct, even if the error is not large for small curvatures. The correct interface position is to be sought from the solution of the Young-Laplace equation (3.120), which suggests that a parabolic shape is the correct one. The protrusion heights are given in both cases in terms of a power expansion of the protrusion angle, defined as the angle that the tangent to the interface at the pinning point forms with the horizontal. These formulas however are considered to be valid under the hypothesis of small values of the interface span c. Both the models for the transverse and the longitudinal protrusion height perform quite well for value of c up to 0.5.

We start by considering the transverse problem, governed by the Stokes equation. In this case we do not fix the interface, but we let the solution to reach the steady state by updating the interface position in time. The mass conservation is enforced using the Lagrange multiplier approach, which is mandatory in order to obtain a mass-satisfying solution. In our numerical simulations we employed the same set-up shown in figure 3.4 and we computed the slip length by varying the viscosity ratio, the capillary number, the length of the cavity c, and the volume ratio Φ defined as the ratio of the volume of the gas to the volume of the cavity. We use Φ instead of the protrusion angle since this quantity is independent form the shape of the interface, while θ can be defined strictly for the circular shape interface, which is not the case of the depressing bubble. We note moreover that, according to our definition, $\Phi > 1$ means that the meniscus is protruding outside of the cavity. Davis and Lauga [2009] derived an analytical formula for the tranverse protrusion height which, according to our nomenclature, reads:

$$\frac{h_\perp}{b} = \left(\frac{c}{b}\right)^2 \int_0^\infty A(s)\,ds, \tag{3.132}$$

where $\frac{c}{b}$ is assumed to be small and the integrand function is

$$A(s) = \frac{s}{\sinh 2s(\pi-\theta) + s\sin(2\theta)} \times \Big[\cos(2\theta) + \frac{s\sin 2\theta \cosh s\pi + \sinh s(\pi - 2\theta)}{\sinh s\pi}\Big], \tag{3.133}$$

where in our case, the angle θ is expressible in term of the volume fraction Φ with no difficulties.

In figure 3.27 we propose a comparison between the analytical model and our numerical simulations. The agreement is good, especially for the values of $c = 0.30$ and $c = 0.50$, but this is not surprising, since the analytical model is valid in the limit of small values of c. If one compares the value of the slip length with $c = 0.70$ and flat interface ($\Phi = 1$), the model by Davis and Lauga [2009] yields $\frac{b}{s} = 0.0963$, while both Philip's and our calculations give $\frac{b}{s} = 0.126$. Increasing the viscosity ratio λ has the effect of decreasing the slip length, since for small λ the approximation of perfect slip along the interface is better. We will return to the effect of the viscosity ratio in the next chapter, with a more extensive discussions. The present simulations also confirm the existence of a critical value of Φ for which the slip length becomes negative. This condition, already pointed out by Steinberger et al. [2007] and Sbragaglia and Prosperetti [2007], occurs when the interface has an excessive protrusion outside of the cavity. The largest value of the protrusion height is found, almost independently of Ca and λ, when Φ is close to 1.05, i.e. when the interface is very mildly protruding out of the cavity. The definite answer on the drag-reducing abilities of the surface can however come only from the resolution of the companion problem for the longitudinal protrusion height since, as shown by Luchini et al. [1991], shear stress reduction at the wall depends to first order on the difference between longitudinal and transverse protrusion heights.

The interface deforms under the action of the shear flow, as shown in figure 3.28, but for a sufficiently low capillary number, it presents a very small deviation from the steady shape position that it would have in the absence of forcing flow. The flow field generated inside the domain are reported in figure 3.29 for both Φ larger and smaller than one.

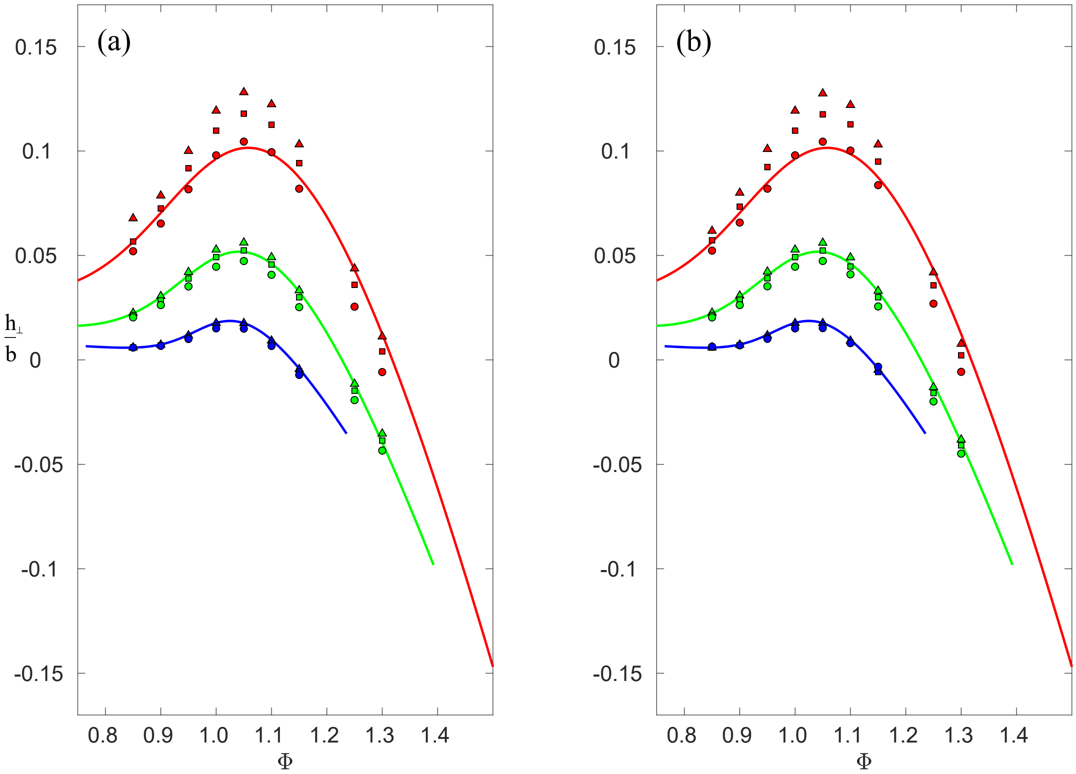

Figure 3.27: Comparison in transverse protrusion heights between the analytical model by Davis and Lauga [2009] and the present numerical simulations. The solid lines correspond to the analytical model by Davis & Lauga for $c = 0.30$ (lower line), $c = 0.50$ (intermediate line), $c = 0.70$ (upper line). Symbols are the simulations, for the same values of c, with $\lambda = 0.018$ (Δ), $\lambda = 0.05$ ($\square$), $\lambda = 0.1$ ($\circ$). (a) $Ca = 1$; (b) $Ca = 0.1$

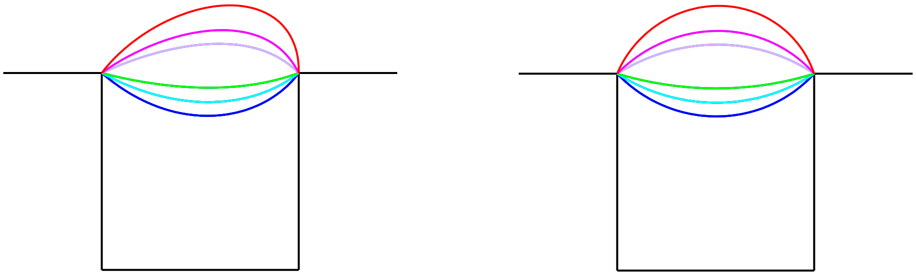

Figure 3.28: Shape of the interface for $Ca = 1$ (left) and $Ca = 0.1$ (right) and $\lambda = 0.1$. The values of Φ are $0.85, 0.90, 0.95, 1.10, 1.15, 1.25$ and the flow is from left to right.

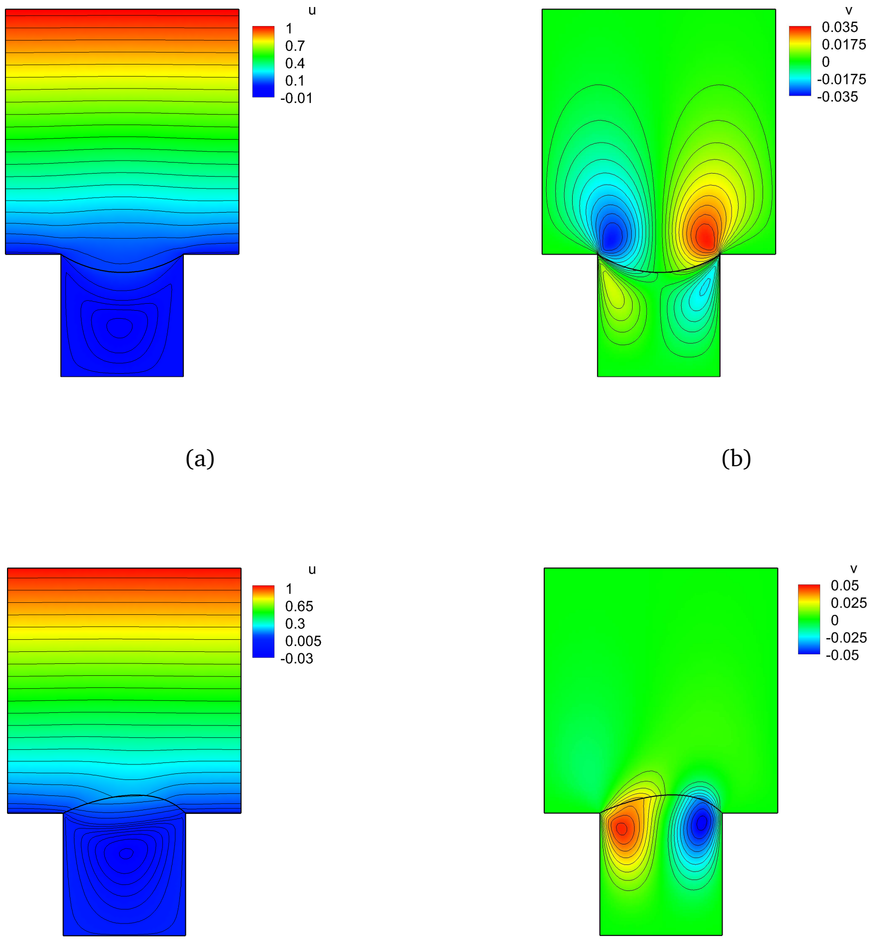

(a) (b) (c) (d)

Figure 3.29: Iso-contours of the streamwise and wall normal velocity for $\lambda = 0.1$ and $Ca = 1$. The value of the volume ratio is $\Phi = 0.85$ (a)-(b) and $\Phi = 1.15$ (c)-(d).

We move further to the validation of the longitudinal problem. In this case we reproduce exactly the set-up found in literature, since here there is no time advancing of the interface and any shape can be set. The analitycal formula by Crowdy [2010] is available for the longitudinal flow and reads

$$\frac{h_{||}}{b} = \left(\frac{c}{b}\right)^2 \frac{\pi}{24}\left[\frac{3\pi^2 - 4\pi\theta + 2\theta^2}{(\pi - \theta)^2}\right], \tag{3.134}$$

where again the angle θ is expressed in term of Φ.

Figure 3.30 reports the comparisons between our numerical simulations, the analytical model and the finite element calculations by Teo and Khoo [2010]. We employ $\lambda = 0.018$ (air-water), which is low enough to consider the perfect slip approximation used by the reference works as reasonably applicable. The results are in perfect agreement with the reference data by Teo and Khoo [2010] and the curve at $c = 0.75$

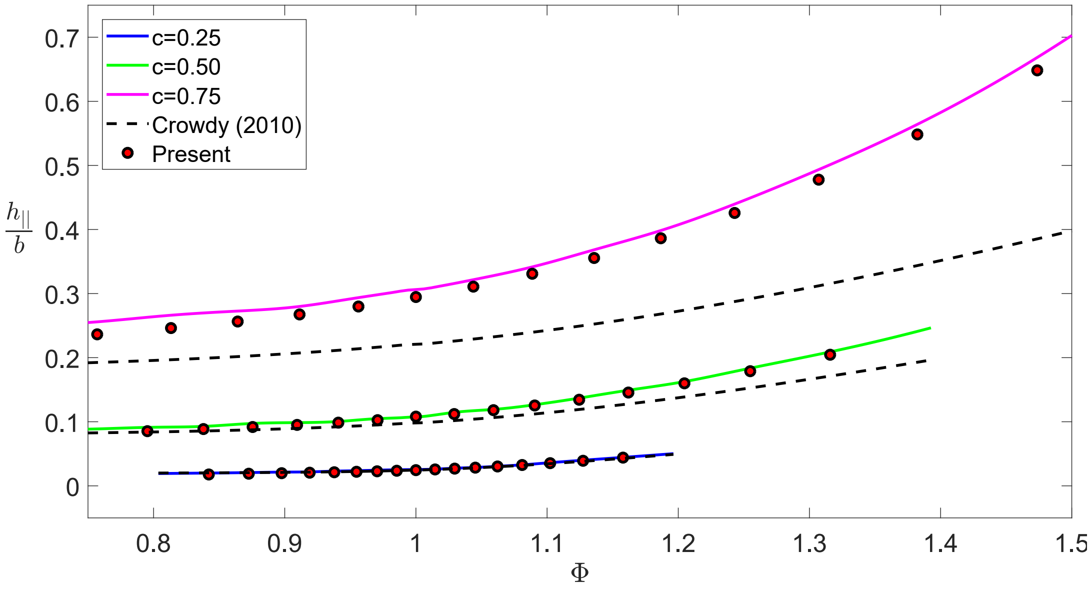

Figure 3.30: Comparison in longitudinal protrusion heights between the analytical model by Crowdy [2010], the numerical results by Teo and Khoo [2010] (solid lines) and the present numerical simulations for different values of c at $\lambda = 0.018$.

is slightly above the values calculated by our simulations, simply because the span of the interface is large and the effect of the non-zero viscosity ratio is mildly felt. The analytical approximation by Crowdy [2010] gives very good result for $c < 0.50$; beyond this value of c the difference between the numerical and the analytical results become large and the model is no more applicable.

3.10.5 Final remarks on validations

In this section, we have applied our boundary element code to different selected test cases for both one-phase and two phase flows. For all the validations, the results are very close to the references, thus we are confident on the predictive capabilities of the code. During the validation campaign we have shown how a viscosity ratio $\lambda < 1$ and the presence of a large interfacial tension cause issues in mass conservation, offering clear examples and a novel remedy. The method proposed is based on an easy-to-implement modification of the linear system obtained by the discretization of the governing boundary integral equation, which consists in adding one constraint equations for the interfacial velocity for each interface inside the domain of interest, by the use of Lagrange multipliers. The technique is very effective in limiting the mass leakage/creation for all the benchmark problems considered. In comparison with the deflation method, introduced by Pozrikidis [2001], it achieves a better convergence, reducing the maximum absolute velocity normal to the interface by several orders of magnitude and ensuring mass conservation even in cases where the double-layer deflation approach fails. We have also taken advantage of the validation step to compare the analytical results available in the literature and the numerical simulations. This comparison highlights that the formulas derived by Davis and Lauga [2009] and

Crowdy [2010] provide a very good estimate of the protrusion heights up to $c \approx 0.5$, which is a surprising large value, since they are both valid under the dilute limit approximation (i.e. very small value of c).

3.11 Flow over superhydrophobic surfaces and LIS

In this section we compare the values of the slip lengths for both the longitudinal and transverse problem, as function of salient geometrical and physical parameters. For our simulation campaign, we set the thickness of the lubricant film $\delta = 0.5$ and let c assume three different values of increasing magnitude, respectively $0.30, 0.50, 0.70$. The interface is either depressing into or protruding out of the wall cavity in dependence of the volume fraction Φ. The viscosity ratio λ between the lubricant and the working fluid is varied from low to high values, keeping in mind that $\lambda < 1$ is commonly encountered in gas-water situations (e.g for air-water $\lambda = 0.018$), while $\lambda > 1$ belongs to oil lubricants. In particular it can be found that $\lambda = 20 \div 100$ is commonly encountered for silicon oils [Than et al., 1988], while $\lambda = 25 \div 50$ is characteristic of vaseline oils [Roelands, 1966], considering water as the working fluid. The capillary number tunes the stiffness of the interface and, in practical applications, it is usually low enough to guarantee an almost rigid interface, undeformed with respect to the shape that would be assumed without flow forcing. In this situation, the interface is described by a circular arch for the case of a protruding bubble [Davis and Lauga, 2009], while a parabolic shape occurs when the lubricant fluid is depressing into the wall cavity. During our simulations, we have found out that a $Ca > 0.25$ is sufficiently small to guarantee a substantially rigid interface, with very small deviation with respect to the steady-state position. This is a favorable result that avoid employing very small values of Ca, which may create an instability of the interface with the explicit time advancing scheme used. Moreover, we found that the protrusion heights exhibit a very low dependency from the capillary number, especially if it is set low enough to guarantee a stiff interface. The reason behind this result is that the value of the protrusion height is mainly influenced by the shape of the interface, which does not vary significantly for $Ca > 0.25$. Due to these considerations, a value $Ca = 0.1$ is employed in our calculations.

We start our analysis by comparing the computed longitudinal and transverse protrusion heights for different viscosity ratios, starting from low to high values, and for different interface spans, which are the most salient parameters involved in the problem. In figure 3.31, the trend of the protrusion heights is shown against the volume fraction Φ. The perpendicular protrusion height $h_\perp$, reported in the left column, shows as expected a dependency on the viscosity ratio and we observe that its magnitude increases as λ and c increase. The physical interpretation is straightforward: on the one hand, the slippage over the lubricant film is promoted by a low value of the viscosity ratio and, on the other, the working fluid encounters a lower resistance as the portion of no slip wall is decreased. Moreover, we note that the reduction in

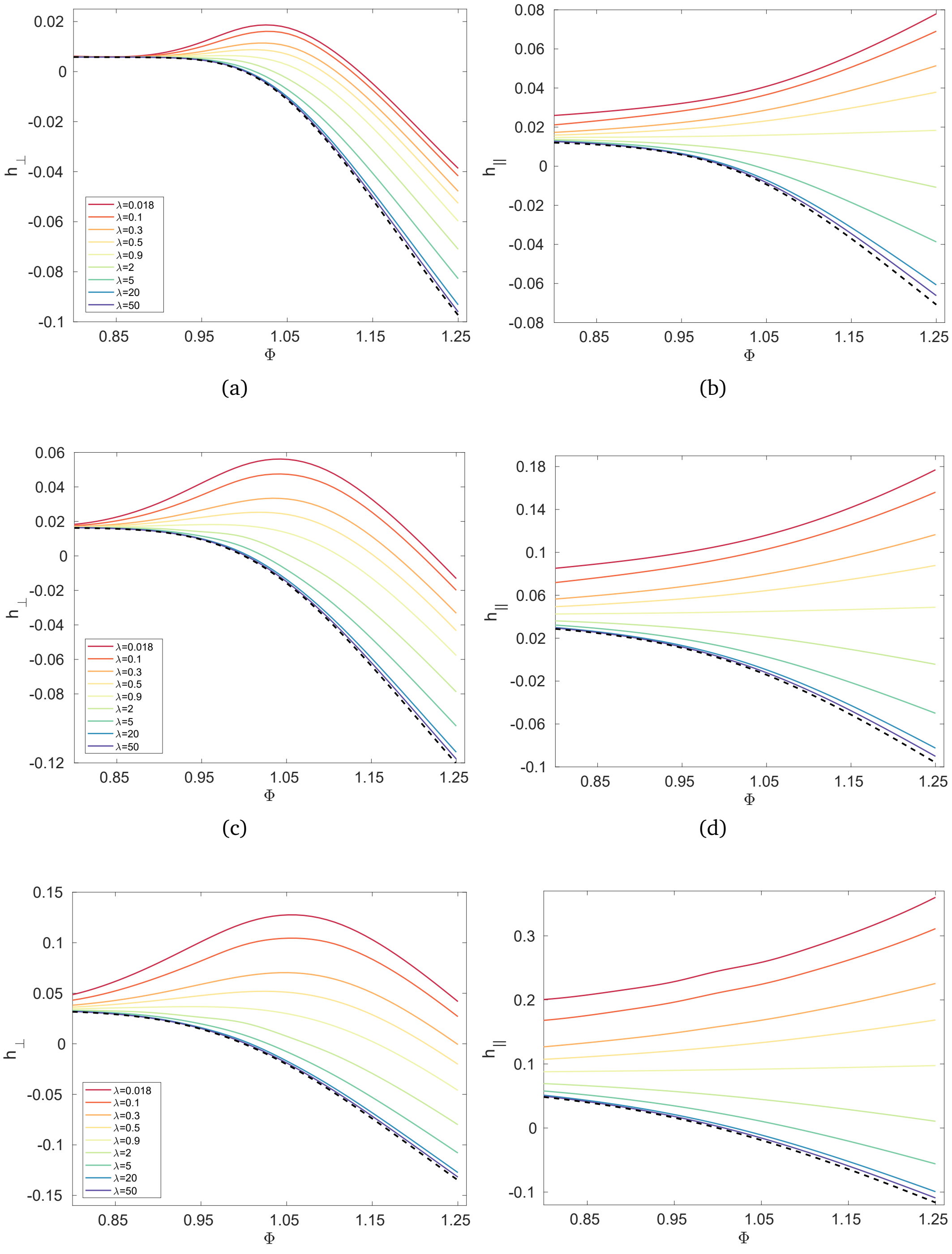

(a) (b)

(c) (d)

(e) (f)

Figure 3.31: Computed transverse (left column) and longitudinal protrusion heights for increasing values of c and a wide range of λ at $Ca = 0.1$. The value of the interface span c is increased from top to bottom namely $c = 0.30$ in the top row, $c = 0.50$ in the middle row and $c = 0.70$ in the bottom row. The dashed lines report the values of the protrusion heights when $lambda \to \infty$, i.e. when the interface is solid.

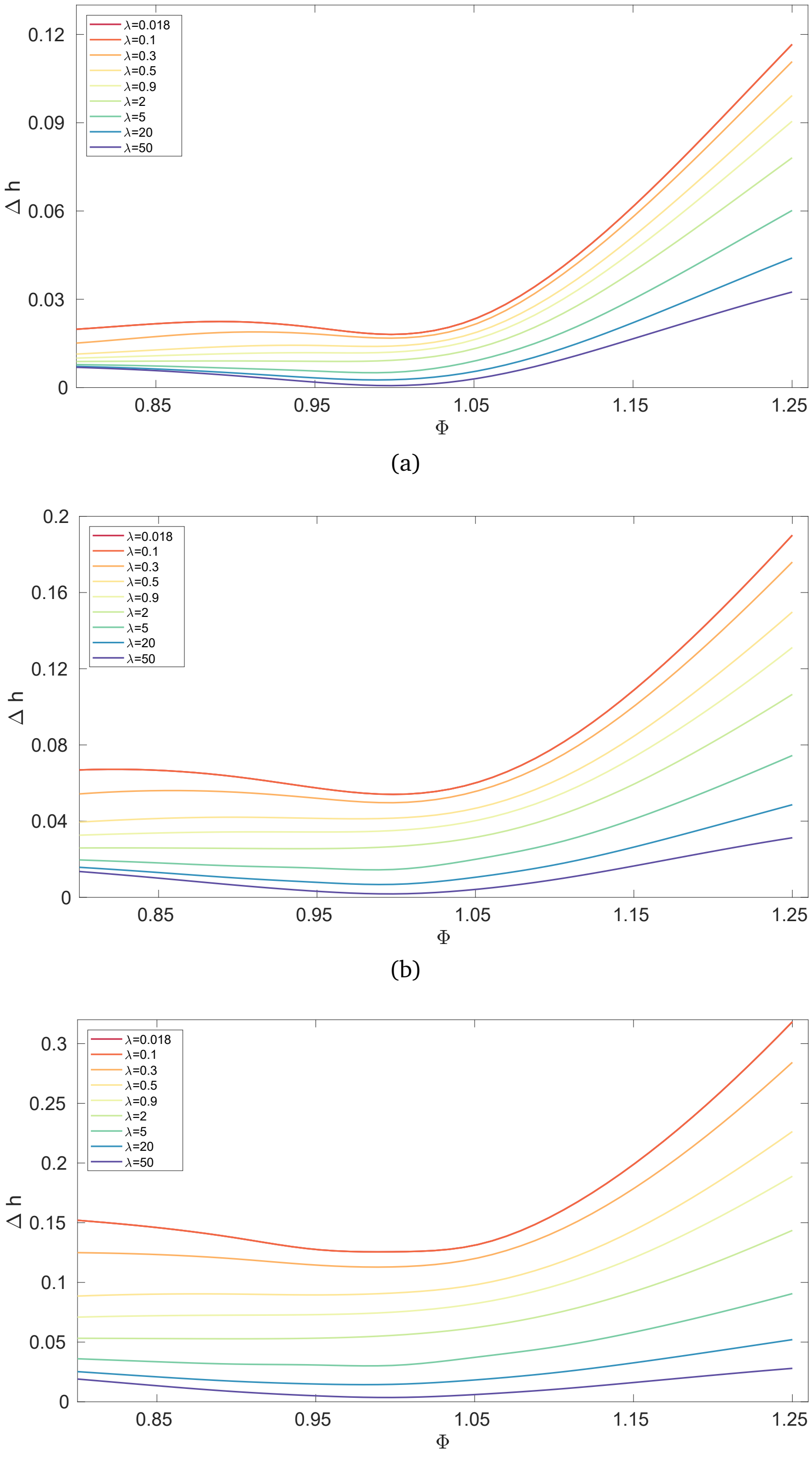

(a)

(b)

(c)

Figure 3.32: Computed difference between transverse and longitudinal protrusion heights for increasing values of c and a wide range of λ at $Ca = 0.1$. The value of the interface span c is increased from top to bottom, from $c = 0.30$ to $c = 0.70$.

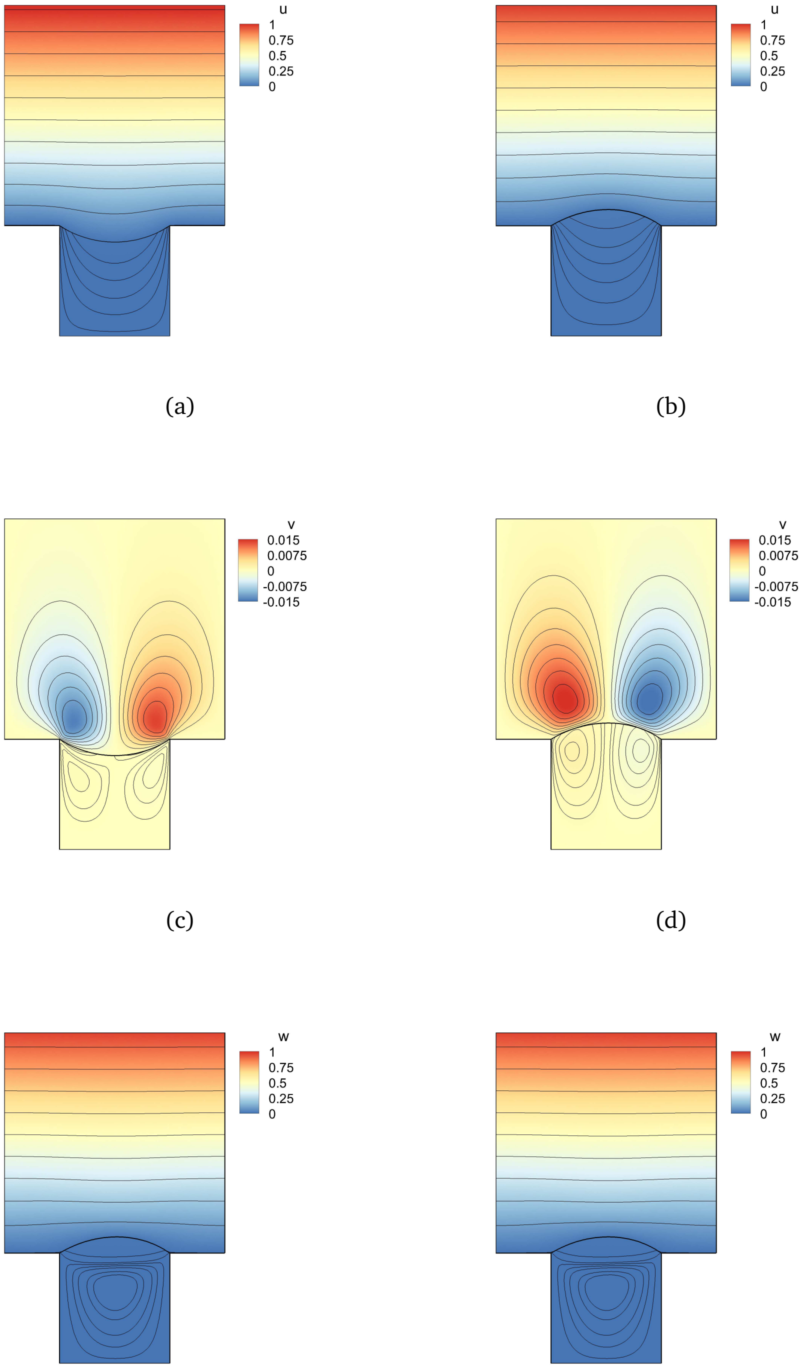

(a) (b)

(c) (d)

(e) (f)

Figure 3.33: Flow field developing into the computational domain for two representative cases with a depressing (left) and protruding (right) interface at $\lambda = 20$ and $Ca = 0.1$. (a)-(b): longitudinal velocity component; (c)-(d) wall normal velocity component; (d)-(e) transverse velocity component.

magnitude, associated to the increase of the lubricant fluid viscosity, is not linear and, for example, an increases of λ from 0.018 to 0.1 produces a small drop in the the protrusion height, with the two curves that remain quite close, especially for the lower value of c. Another information that can be inferred is that the viscosity ratio does not only affect the magnitude of $h_\perp$ but also its trend as function of Φ. In particular, as soon as $\lambda > 1$, the protrusion height presents a maximum for a value of Φ slightly larger than the unity. The maximum position is however not constant and moves slightly leftward as λ increases. The slip length keeps reducing with the increase of the viscosity ratio until $\lambda = 1$ is reached. A further increment of λ profoundly changes the trend of the protrusion height, which, from this point on, will no longer present a maximum. We can note that for values of λ approximately grater than 5, the curve become very close to the dashed line reported in figure 3.31, which corresponds to the slip length computed with the no-slip condition applied over the interface. This result is consistent with the fact that a lubricant fluid with a large viscosity compared to that of the working flow, in practice, behaves like a solid wall, minimizing the slippage and drastically reducing the drag reduction performance of the surface. Finally, we note that the protrusion height shows an asymmetric behaviour with respect to the unitary value of Φ (i.e. flat interface). For a given value of c, increasing the volume fraction after the optimal value, the slip length starts to monotonically decrease following a quasi-linear variation, whose slope is almost independent from the viscosity ratio. Reducing the volume fraction, we obtain that the value of the slip length decreases again but never crosses the limit delineated by dashed line since, in the limit of $\Phi \to 0$, the geometry behaves like riblets similar to those studied by Luchini et al. [1991].

For the parallel protrusion heights $h_{||}$, reported in the right column of figure 3.31, we can extract similar features to those discussed for $h_\perp$. Again there is a strong dependence on the viscosity ratio, and the magnitude of the parallel protrusion height increases as λ decreases. The decrement of the slip length associated with an increase of the viscosity ratio is not linear. The fact that the reduction of the protrusion height does not scale linearly with the reduction of the viscosity ratio is potentially a favorable behaviour which hypothetically permits to use a couple of fluids forming a more robust interface, while minimizing the penalty associated to the increase of the viscosity ratio. The longitudinal slip lengths do not exhibit a maximum as function of the volume fraction, but keep increasing along with Φ for $\lambda < 1$, while showing an opposite and non-symmetric trend with respect to the value of the viscosity ratio. This particular behaviour of the parallel slip length was also reported by Ng and Wang [2011], who allowed a partial slip over the interface by means of the Navier boundary condition with an intrinsic slip-length, which however did not have a clear physical meaning. Also in this case, for a large value of λ the curves collapse on the dashed line, representing the longitudinal protrusion height for the no-slip condition applied on the interface. Thus, it is found again that a large viscosity of the lubricant fluid leads the interface to behave similarly to a no-slip wall.

It is now important to underline, that the standalone values of the protrusion heights may have a small relevance when a turbulent flow over SHS/LIS is being considered. As pointed out by Luchini [1996], the parameter that controls the drag reduction is the difference between the slip lengths: the larger is this difference the larger will be the drag reduction to be expected. This topic is being discussed in the next section. Following this criterion, it is useful to look at this difference reported in figure 3.32. The best drag reduction, at any given viscosity ratio, will be obtain for the most protruding bubble, while the worst scenario coincide with the value of Φ which maximize the transverse protrusion height, corresponding to an inflection of the curves representing Δh. These considerations are expected to be not valid if the typical size of the bubble mattress becomes to large with respect to the size of viscous sublayer. In this case, especially for the LIS cases involving a high viscosity ratio, a surface roughness-behaviour is expected [Jiménez, 2004], turning the drag reduction into a drag increase.

The flow field for both longitudinal and transverse flow can be reconstructed into the domain and is shown in figure 3.33 for a representative case at $\lambda = 20, c = 0.50, Ca = 0.10$ and $\phi = 0.90$ and $\Phi = 1.10$. As expected, consists in a recirculation zone taking place between the wall cavity and the interface for the transverse flow, while a linear velocity profile is established for both u and w at a sufficient distance above the interface.

3.12 Outlook and perspective

The flow over superhydrophobic and liquid-impregnated surfaces has been simulated taking advantage of the Stokes problem decoupling, which leads to the definition of the longitudinal and the transverse problems. This procedure is possible only taking into account a periodic wall texture along the streamwise direction and this limitation does not allow to evaluate the flow past other important configurations, such as pillars, which, conversely, require a fully three dimensional simulation. The extension of the present work in 3D would surely possible but has some bottlenecks outlined in this section. The boundary integral formulation is in principle not difficult to extend in three dimensions, since the assembling procedure presented in section 3.5 still applies and the final result will be formally very similar to equations (3.57). Naturally, the single and double layer operators turn from line to surface integrals extended over the patches composing the computational domain. The difficulties are more related to the numerical solution of the boundary integral equation then on their theoretical definition. From a practical point of view, the first issue encountered is the discretization of surfaces in triangles or, for a better accuracy, in $6-$nodes curved triangle with the associated difficulties related to the complication of the quadrature formulas for the integral operators [Pozrikidis, 2002]. Moreover, the doubly periodic Green's function for the Stokes flow, which in two dimensions has the closed form (3.88), in three dimensions loses this feature and it is to be found by Fourier series expansion or by Ewald summation method [Pozrikidis, 1996], thus increasing in a consistent manner the difficulties of the calculations. The integral operators present a non-regular behaviour when the field point lays on domain's boundary; the de-singularization of the integrals becomes very difficult and it usually performed by the employing specific mathematical identities which, however, creates some issue in a direct solution of the discrete boundary element system. The solution is usually found by iteration with a process, introduced by Pozrikidis [Pozrikidis, 2002], similar to the Gauss-Seidel method.

Considering all these technical issues, it is maybe a good idea concentrate the efforts on the direct numerical simulations of the turbulent flow over SHS/LIS in a similar fashion to the one employed for the surface roughness. This approach is surely computational expensive but presents the advantages that the evaluation of the drag reduction performance of the coating is not restricted to the validity limit of the protrusion heights approach. The solution of the problem in this sense is however far to be trivial and passes thorough the use of a proper level-set (LS) or volume of fluid (VoF) approach [Hirt and Nichols, 1981]. Two main issues have been detected with this approach during the development of the present work. The first is related to the lack of a proper boundary condition, within the LS/VoF framework, able to guarantee the anchoring of the interfaces at the pinning edges of the underlying wall texture. This is due to the fact that the both LS and VoF solve an hyperbolic equation for the transport of the indicator function and thus the boundary conditions that can be specified are of Dirichlet or Neumann type. None of the two is able to fulfill the proposed target, since the pinning is physically the result of the energy balance between the solid, the liquid and the gaseous phase which is not taken into account in the model. A rough way to overcome this issue is to assign a discontinuous Dirichlet boundary condition, prescribing a jump of the indicator function in the region where the pinning is desired. Even if working, the stability of the calculation can be significantly affected by this procedure. The second problem is addressed to the creation of parasitic currents consisting in the generation of non-physical velocities near the fluid interface and the phenomenon becomes very significant in the presence of surface-tension-dominated flows. Very promising in the mitigation of this problem seems to be the numerical method proposed by Raeini et al. [2012], even if it is not of easy implementation, it may constitute a valid approach to the problem. Another promising methodology has been very recently proposed by Xie and Xiao [2017] and it presents an affordable programming difficulty.

Chapter 4

The macroscopic problem

In this chapter, we discuss the results related to the macroscopic problem with a focus on the estimation of a drag reduction induced by SHS/LIS coatings in a turbulent flow in a channel. Since in this case the characteristic length scale might be very different with respect to the microscopic flow near the wall protrusions, the key-idea is to use the calculated values of the protrusion heights to model the slippage at each wall by means of an equivalent boundary condition applied to a fictitious and smooth surface. A suitable condition was introduced by Navier [1823] and reads

$$\boldsymbol{u} = \boldsymbol{h}\left(\frac{\partial \boldsymbol{u}}{\partial n}\right), \quad \boldsymbol{h} = diag(h_{||}, h_{\perp}) \tag{4.1}$$

where $\boldsymbol{u}$ is understood as the velocity field components in the in-plane directions and $\boldsymbol{h}$ is the slip tensor, which depends on the wall texture, while the condition for the wall normal velocity is simply $v = 0$. Equation (4.1) gives a relation between the slip velocity and the wall shear stress. Any orientation of the SHS/LIS with respect to the flow direction can be obtained by a simple rotation of the slip tensor $\boldsymbol{h}$, as already shown in chapter 2.

In general, we consider a three-dimensional unsteady flow governed by the momentum and continuity equation for an incompressible, Newtonian fluids

$$\nabla \cdot \boldsymbol{u} = 0, \tag{4.2}$$

$$\frac{\partial \boldsymbol{u}}{\partial t} + (\boldsymbol{u} \cdot \boldsymbol{\nabla})\boldsymbol{u} = -\boldsymbol{\nabla} P + \frac{1}{Re_b}\nabla^2 \boldsymbol{u} + \boldsymbol{f}. \tag{4.3}$$

The equations have been made non-dimensional by choosing a reference length and velocity scales, U^* and L^*, and introducing the corresponding Reynolds number $Re = \frac{U^* L^*}{\mu}$, where ρ and μ are the density and dynamic viscosity of the fluid considered.

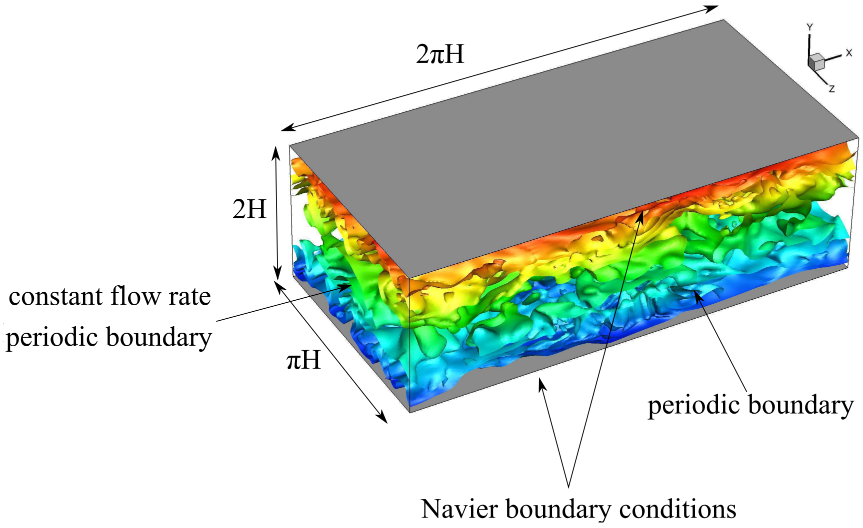

Figure 4.1: Computational domain with dimensions and boundary conditions. The colors represent iso-surfaces of instantaneous streamwise velocity colored by the bottom wall distance.

We consider for our calculations a classical turbulent channel flow studied so far by Kim et al. [1987], shown in figure 4.1, together with the boundary conditions. We perform our simulations at nominal $Re_\tau = 180$, corresponding to $Re_b = \dfrac{U_b H}{\nu} \approx 2800$, using the mean bulk velocity. Periodic boundary conditions are applied in both streamwise and spanwise directions, while the upper and the lower wall are assumed to be coated with a SHS/LIS, taken into account via the Navier boundary condition. The values of the slip lengths are taken from microscopic calculations found in chapter 3 and conveniently re-normalized using the half channel height H. The flow inside the channel is driven by a pressure gradient $\boldsymbol{f}$ that maintains a constant streamwise flow rate in time.

4.1 Numerical method

The finite volume method is a numerical approach for solving compressible and incompressible fluid flows in any number of space dimensions and it is the numerical method employed in our macroscopic calculations. The starting point is the discretization of the conservation equations (4.2): the fluid domain is subdivided in a finite number of small, non overlapping, control volumes by a grid which defines the control volume boundaries. The computational nodes, where the unknown variables $(\boldsymbol{u}, p)$ are to be computed, can be arranged mainly in two different ways:

- staggered;
- collocated.

The staggered arrangement, allocates the velocities at the control volume boundaries and the pressure in the cell center, while, in the collocated arrangement, all the unknowns are computed in the control volume center. Despite their simplicity, collocated grids were out of favour for a long time in the past because of their aptitude to create pressure oscillations in the flow field. However, after solutions of this problem have been proposed [Rhie and Chow, 1983], the collocated arrangement was preferred thanks to its simplicity in non-Cartesian grid generation.

The basic idea of the finite volume method is to require the satisfaction of the conservation equations at each control volume; thus, if the mass and momentum balance are satisfied at each control volume (CV), they will be satisfied on the whole domain. The Navier-Stokes equations and continuity equation are integrated over each control volume assuming the following integral form:

$$\int_\Omega \frac{\partial u_i}{\partial t}\, d\Omega + \int_\Omega u_i \frac{\partial u_j}{\partial x_j}\, d\Omega = -\int_\Omega \frac{\partial p}{\partial x_j}\, d\Omega + \int_\Omega \frac{1}{Re}\frac{\partial}{\partial x_j}\frac{\partial u_i}{\partial x_j}\, d\Omega + \int_\Omega f_i\, d\Omega, \tag{4.4}$$

$$\int_\Omega \frac{\partial u_i}{\partial x_i}\, d\Omega = 0. \tag{4.5}$$

In figure 4.2 a three-dimensional Cartesian control volume is presented together with the notations used. The CV consist of six plane faces, denoted with lower case letters (e, w, n, s, t, b), corresponding to their orientation with respect to the central node (P).

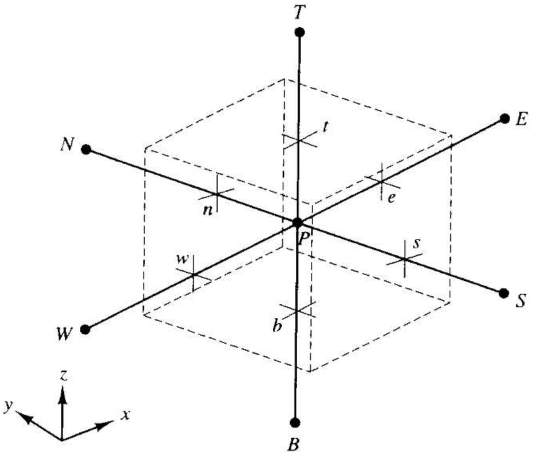

Figure 4.2: Control volume for a three dimensional Cartesian grid.

The volume integrals involving the convective and the diffusion terms can be conveniently transformed into surface integrals over the CV boundaries using Gauss' divergence theorem and the incompressibility condition:

$$\int_\Omega u_i \frac{\partial u_j}{\partial x_j}\, d\Omega = \int_S u_i \boldsymbol{u}\cdot\boldsymbol{n}\, dS, \tag{4.6}$$

and

$$\int_\Omega \frac{1}{Re}\frac{\partial}{\partial x_j}\frac{\partial u_i}{\partial x_j}\, d\Omega = \int_S \frac{1}{Re}\nabla u_i \cdot \boldsymbol{n}\, dS. \tag{4.7}$$

An arbitrary flux ϕ through the CV boundaries can be calculated as the sum of all fluxes through the surface composing the control volume as:

$$\int_S \phi \, dS = \sum_{k=1}^{N} \int_{S_k} \phi \, dS, \tag{4.8}$$

where N is the number of control volume faces and ϕ can be either the convective or the diffusive flux defined in equations (4.6)-(4.7).

In order to numerically solve the equations, an approximation for the surface integrals must be made. The common practice consists in estimating the surface fluxes, for an arbitrary face k, with the mid-point rule as:

$$\int_{S_k} \phi \, dS \approx \phi_k S_k. \tag{4.9}$$

The integral is approximated by the value of ϕ at the surface center, times the area of the surface at which the integral is calculated. It is possible to show that this approximation is of second order accuracy. Usually, for collocated grids, the value of ϕ at the face center is not known and an interpolation is needed in order to express ϕ_k as a function of neighboring computational nodes. Referring to figure 4.2, the value of ϕ at the CV face centers is obtained by linear interpolation between the two nearest nodes, as follows (e.g. for the "e" face):

$$\phi_e = \lambda \phi_P + (1 - \lambda) \phi_E, \tag{4.10}$$

where λ is a weight defined as:

$$\lambda = \frac{x_e - x_E}{x_E - x_P}. \tag{4.11}$$

This scheme is called central difference scheme and it is of second order accuracy. For clarity, the discretization of the convective fluxes will be shown only for the e-face of the cartesian CV shown in figure 4.2 and only for the velocity component u along the x direction. The fluxes at the other surfaces can be treated in the same fashion applying the appropriate subscripts permutation. Applying the above approximation, the discrete convective and diffusive fluxes read

$$\int_{S_e} u_i \boldsymbol{u} \cdot \boldsymbol{n}_e \, dS_e \approx m_e u_e = m_e [\lambda u_P + (1 - \lambda) u_E], \tag{4.12}$$

and

$$\int_{S_e} \frac{1}{Re} \nabla u_i \cdot \boldsymbol{n}_e \, dS_e \approx \frac{S_e}{Re} \frac{u_E - u_P}{x_E - x_P}; \tag{4.13}$$

$m_e = u_e S_e$ in (4.12) is the mass flow rate through the surface e.

The spatial discretization is completed by the approximation of the pressure gradient and the body forces, also called source terms. For an arbitrary source term $\boldsymbol{q}$

the following approximation is applied:

$$\int_{\Omega_P} \boldsymbol{q}\, d\Omega \approx \boldsymbol{q}_P \Delta\Omega_P \quad . \tag{4.14}$$

The integral is estimated by the product between the central value of $\boldsymbol{q}$ in the control volume center and the cell volume $\Delta\Omega$. Adopting this rule, the finite volume approximation for the pressure term becomes (e.g along the x direction):

$$\int_{\Omega} \frac{\partial p}{\partial x_j}\, d\Omega \approx \frac{(p_e - p_w)}{\Delta x_p} \Delta\Omega; \tag{4.15}$$

p_e and p_w are the interpolated values of p at the control volume faces e and w using the already defined central difference scheme.

Analogously, the forcing term $\boldsymbol{f}$ is:

$$\int_{\Omega_P} \boldsymbol{f}\, d\Omega \approx \boldsymbol{f}_P \Delta\Omega_P. \tag{4.16}$$

It is worth to note that problems may appear using collocated grids and pressure oscillation may appear in the flow field and lead to non-physical results. The problem is resolved using a method, originally developed by Rhie and Chow [1983], which consists in correcting the mass flow rate through a control volume surface by using additional terms involving the pressure gradient at the target face.

4.1.1 Fractional Step Method

The lack of an explicit equation for the pressure complicates the numerical solution of the Navier-Stokes equation. The continuity equation in incompressible flows can be consider more as a kinematic constraint for the velocity field, rather than a dynamic equation. One way to solve this problem relies on the fractional step method. This technique is often used to advance in time the fluid flow governing equations and was firstly developed by Chorin [1968] and then improved by other authors [Kim and Moin, 1985, Perot, 1993]. The algorithm is based on Hodge's decomposition of any vector field into a solenoidal and an irrotational part and, typically, consists of two stages:

- prediction;
- correction.

In the prediction step, the momentum equation is solved, but the resulting solution does not satisfy the continuity equation. In the correction step the previous solution is corrected and the velocity field is projected onto a divergence-free field.

Several numerical implementations are available in the literature; in the present study we employ the fractional step method proposed by Kim and Moin [1985]. The method is semi-implicit and not all the terms of the momentum equation are discretized in time in the same manner. In particular the second order Crank-Nicolson

scheme is used for the wall-normal diffusive term and the second order Adams-Bashforth scheme for all the other terms in the momentum equation.
The two-step time advancement scheme can be written as:

$$\frac{\hat{\boldsymbol{u}} - \boldsymbol{u}_i^n}{\Delta t} = -\mathcal{N}_l(\boldsymbol{u}^n, \boldsymbol{u}^{n-1}) - \mathcal{G}(\phi^n, \phi^{n-1}) + \frac{1}{Re}\mathcal{L}(\hat{\boldsymbol{u}}_i, \boldsymbol{u}^n), \tag{4.17}$$

$$\frac{\boldsymbol{u}^{n+1} - \boldsymbol{u}^n}{\Delta t} = -\mathcal{G}(\phi^{n+1}), \tag{4.18}$$

together with the continuity condition:

$$\mathcal{D}(\boldsymbol{u}^{n+1}) = 0, \tag{4.19}$$

where $\mathcal{N}_l$ and $\mathcal{D}$ are shorthand notations for the discrete non-linear and the diffusion terms, while $\mathcal{G}$ and $\mathcal{L}$ stand for the discrete gradient and laplacian operators. The scalar quantity ϕ, known as projection variable, is to be found by solving the following Poisson problem (projection step), arising after the divergence operator is applied to the equation (4.18):

$$\mathcal{L}\phi = \frac{1}{\Delta t}\mathcal{D}\hat{\boldsymbol{u}}; \tag{4.20}$$

equation (4.20) to be solved along with Neumann boundary conditions applied at the solid walls [Kim and Moin, 1985].

In summary, the strategy to solve the Navier-Stokes equation with the fractional step method consists in predicting the velocity field using equation (4.17), then finding the projection variable from the equation (4.20) and finally correcting the velocity field using the relation (4.18).

The numerical procedure described has been implemented in a well-established curvilinear finite volume code [Omidyeganeh and Piomelli, 2013, Rosti et al., 2016, Pinelli et al., 2017] written in Fortran 77 and parallelized with OpenMPI.

4.2 DNS results

Since the parameter space is quite large, we propose to perform the simulations fixing the periodicity b of the SHS/LIS such that $b^+ = \dfrac{bu_\tau}{\nu} \approx 10$ with small variations due to the fact that the friction velocity slightly decreases along with the increase of the slip at the walls. There are two reasons to maintain a small periodicity: from a theoretical point of view, the protrusion height approach within the Navier boundary condition is demonstrated to be valid for $b^+ < 20$ [Luchini, 2015, Seo and Mani, 2016]. From a practical point of view, SHS/LIS are characterized by a small periodicity, since large cavities suffer of lubricant layer depletion.

We are interested in determining the drag reduction, expressed in terms of the friction coefficient $C_f = \dfrac{2\tau_w}{\rho U_b^2}$, as function of the protrusion heights, calculated from

Case	$h_{\|\|}^{\times 10^3}$	$h_{\perp}^{\times 10^3}$	$\Delta h^{\times 10^3}$	$\frac{C_f}{C_{f0}}$	$error\%$
1	12.3	6.00	6.30	0.86	-
2	9.30	3.00	6.30	0.84	-2.3
3	6.30	0.0	6.30	0.88	$+2.6$

Table 4.1: Test cases for the protrusion heights offset.

the microscopic problem solved in the previous section. The reason behind the drag reduction is to be found close to the wall and in the effect that a slip velocity has on the near-wall turbulence. On the one hand, an increase of slip in the streamwise direction (i.e. a large value of the slip length) tends to reduce the skin friction and to attenuate the wall cycle. On the other hand, a spanwise slip has a much less trivial effect. As shown by Choi et al. [1994] and Min and Kim [2004], the creation of a slip velocity in the spanwise direction tends to increase the drag because of the enhancement of the strength of the near-wall streamwise vortices. The skin friction drag reduction for a combined longitudinal and transverse slip is a consequence of the competition between these two mechanisms. Following the theory developed by Luchini et al. [1991], the most important parameter governing the skin-friction drag is the difference between the protrusion heights. Thus, before proceeding further, it is important to test that considering the difference of the protrusion height as the main parameter governing the drag reduction is a reasonable approximation, at least for small values of the slip lengths and thus Δh.

We start by testing the following cases, reported in table 4.1, which present the same value of Δh, but different $h_{||}$ and $h_{\perp}$. In particular, in cases 2 and 3, the values of the protrusion heights have been modified by subtracting a constant offset, leading to a situation where only the longitudinal slip is allowed, and to a mixed case where slip is allowed in both streamwise and spanwise directions. For each case, we have calculated the friction coefficient, scaled with the reference C_f computed for the standard no slip walls case (denoted as C_{f_0}), together with the percentage error, $error = \dfrac{C_f - C_{f_{ref}}}{C_{f_{ref}}} \times 100$, where the reference is case 1. What we can note is that there is a small difference between the drag reduction computed in the three cases. However, the percentage difference in the skin friction is much smaller (one order of magnitude) with respect to the variation of the slip lengths. This difference in friction coefficient suggests that the protrusion height $h_{||}$ in the direction of the flow has a slightly larger impact on the drag reduction. To shed more light on this behaviour, we restrict ourselves to the case $\Delta h = 0$, with $h_{||} = h_{\perp}$, where a negligible drag reduction should be expected; however, this is not the case since some drag reduction is indeed observed as demonstrated by Min and Kim [2004] and Luchini [2015] and also by our simulations and this is consistent with the observation of drag reduction for isotropic lattices (e.g. circular posts), where the slip lengths are equal.

The error committed in considering the drag reduction dependent only on the difference between the protrusion heights increases with the increase of the value of the longitudinal slip. This is suggested by Luchini [2015] who conducted a series of DNS employing a fixed value of $h_{||} = h_{\perp}$ and varied the slip at the walls for increasing values of b^+ (i.e. increasing $h_{||}^+$ and $h_{\perp}^+$). In his simulations he has shown that the drag reduction presents a quadratic behaviour in b^+ and for $b^+ \approx 25$ the resulting drag reduction is about 10%. The fact that a linear relation between Δh and the amount of drag reduction cannot hold in the case of large values of the slip lengths is also suggested by the Navier boundary condition itself: upon increasing $h_{||}$ and $h_{\perp}$ the wall tends to be a no-shear region, thus yielding a drag reduction of 100%. Further discussions and clarifications on the effect of the protrusion heights on the skin friction drag reduction can be made on the basis of the results obtained by Busse and Sandham [2012]. In their paper, the authors analyzed in detail the effect of the protrusion heights on the percentage drag reduction for a turbulent channel flow. They conducted a large number of direct numerical simulations both at $Re_{\tau} = 180$ and $Re_{\tau} = 360$ for several values of $h_{||}^{+0}$ and $h_{\perp}^{+0}$ within the range $[0, 100] \times [0, 100]$. The super-script $\bullet^{0+}$ means that the protrusion heights are expressed in wall units based on the nominal Re_{τ}. Their results clearly show that the effect of the transverse protrusion heights on the drag increase effect is non-linear and saturates at $h_{\perp}^{+0} \approx 4$. This justifies the fact that the skin friction drag is always observed to decrease for $h_{||}^{+0} > 3.5$ and for any arbitrary large value of $h_{\perp}^{0+}$. In general, the combined effect of the slip lengths on the drag reduction is shown in figure 4.3(a). The contour plot highlights the zone of drag reduction and drag increase with respect to the reference value for a standard channel at nominal $Re_{\tau} = 180$ and it is obtained by cubic interpolation of their numerical results. The red dots represent our numerical results which are in good agreement with the predictions by Busse and Sandham [2012] and corroborate their calculations. The values of the slip lengths used in our DNS are taken from the microscopic problems and are reported in table 4.2. Since for the microscopic texture analyzed the parallel protrusion height is always bigger then the transverse one, in our cases a drag reduction is always obtained.

Beyond the theoretical importance of the results reported in figure 4.3(a), it is useful to stress the fact that not all the zones in this plot are of practical and physical application, since the Navier boundary condition is demonstrated to be valid up to a certain level of slip. To fix the idea, let us look in more detail to the simulations conducted by Luchini [2015]. He considered the wall coated by longitudinal no-shear stripes, mimicking a superhydrophobic surfaces with a flat interface between the phases. The ratio between the interface span and the texture periodicity b was fixed to 0.5 and a series of direct numerical simulation at $Re_{\tau} \approx 180$ were conducted for different values of b. He demonstrated that the protrusion heights yield very similar results to those obtained by taking into account the real wall texture up to $b^+ \approx 20$. The protrusion heights normalized by the periodicity for such walls are easily calculated from Philip's theory and are $h_{||} = 0.11$ and $h_{\perp} = 0.055$, respectively.

Considering the upper bound of $b^+ = 20$, it is easy to find that, in wall units, the slip lengths are $h_{||}^{+0} \approx 2.5$ and $h_{\perp}^{+0} \approx 1.2$, which give a first idea of the region of validity of the protrusion height approach.

In literature, there are several theoretical predictions that have been attempted over the years which try to establish some relation between the drag reduction and difference in the protrusion heights. Luchini [1992] and, later on, Bechert et al. [1997] tried to link the difference in the protrusion heights following a similar reasoning, which has Prandtl's universal formula as starting point:

$$\left(\frac{C_f}{2}\right)^{-\frac{1}{2}} = k^{-1}\log\left(\left(\frac{C_f}{2}\right)^{\frac{1}{2}} Re\right) + B + A, \tag{4.21}$$

where Re is the Reynolds number and B is a constant. Linearizing (4.21) for small changes in C_f and A we obtain:

$$\frac{\Delta C_f}{C_{f_0}} = -\frac{\Delta A}{(2C_{f_0})^{-\frac{1}{2}} + (2k)^{-1}}, \tag{4.22}$$

where C_{f_0} is the reference friction factor for the standard no-slip wall at the actual Re_τ and k is von Karman's constant, which we can take equal to 0.41.

Thus, attention is turned on how the universal constant A changes when the turbulent boundary layer is influenced by non-smooth wall textures (e.g. riblets, SHS, LIS or roughness). For a smooth wall the velocity profile in the viscous sublayer takes the form $u^+ = y^+$, while in the logarithmic region it becomes $u^+ = k^{-1}\log(y^+) + A$. The two laws meet at the point y_0^+, satisfying the following equation

$$y_0^+ = k^{-1}\log(y_0^+) + A, \tag{4.23}$$

yielding $y_0^+ = 10.8$ for $k = 0.41$ and $A = 5$. Luchini [1992] suggested that the point y_0^+ should shift by the quantity Δh^+ in the presence of surface texture. Linearizing equation (4.23) about the smooth wall value and letting $y_0^+ = 10.8 + \Delta h^+$, it is obtained:

$$\Delta A = 0.774\Delta h^+. \tag{4.24}$$

Following the same reasoning, but using a slightly different values for k and A, Bechert et al. [1997] found a coefficient of 0.785, while Jiménez [1994] used a formula similar to equation (4.24) on account of the linearity of the viscous regime, recommending a coefficient of 0.66. Later on, Luchini [1996] reconsidered the formula (4.24) imposing the coefficients in front of Δh^+ to be equal to one, since he argued that it is not the point y_0^+ which undergoes a translation, but the whole velocity profile should be shifted by the quantity Δh^+. The final form of the correlation for the friction factor reduction is thus given by

$$\frac{C_f}{C_{f_0}} = 1 - \frac{\Delta h^+}{(2C_{f_0})^{-\frac{1}{2}} + (2k)^{-1}}. \tag{4.25}$$

The effect of a given micro-ribbed surface (whether superhydrophobic, LIS or not) is thus that of changing A and this becomes equivalent to the *roughness function* used to characterize rough surfaces, at least in simple geometries [Jiménez, 2004].

Unfortunately, this simple and practical rule is not valid for all possible values of $h_{||}$ and $h_{\perp}$ which have, as shown in figure 4.3, a non-trivial effect on the drag reduction, especially when they assume a large value in magnitude. Gathering together the information on the drag reduction collected by our numerical simulations, by Min and Kim [2004] and by Busse and Sandham [2012], it is however possible to estimate a region of validity of the relation (4.25). The simulations taken as samples are indicated in figure 4.3(b), by circles in different colors: the red dots represent our numerical simulations, the green dots are results from Min and Kim [2004], while magenta indicates the calculations by Busse and Sandham [2012]. We refer only to the drag reducing region since, for the particular wall texture under investigation in this work, $h_{||} > h_{\perp}$ and the only possible effect is a drag reduction. Figure 4.4 shows a comparison between the analytical formula 4.25 and the numerical simulations. The values of Δh are normalized using the actual friction velocity ($u_\tau = u_{\tau 0}\sqrt{\frac{C_f}{C_{f_0}}}$) as velocity scale, which is a more suitable choice with respect to u_{τ_0}, since Re_τ might slightly change as function of the wall slippage. The correlation between the numerical data and the linear relation 4.25 turns out to be satisfying in region bounded by the dashed lines in figure 4.3(b), where the maximum value of the protrusion heights is $h_{||}^{+0} \approx 3.2$ and $h_{\perp}^{+0} \approx 1.5$ or $h_{||}^{+} \approx 2.7$ and $h_{\perp}^{+} \approx 1.3$. In a more conservative way, we can assume $h_{||}^{+} \approx 2.3$ ($h_{||}^{+0} \approx 2.6$) and $h_{\perp}^{+} \approx 1.1$ ($h_{\perp}^{+0} \approx 1.2$). These values are very near to the ones estimated by Luchini's simulations.

As a final note, we remark that relation (4.25) becomes invalid if the wall textures becomes so large in characteristic size to interact non linearly with the near-wall turbulent structures with the near-wall turbulent structures. It is also invalid if the protrusion heights assume large values as detailed above. If a case of study falls outside this limit, the simplified application of the Navier boundary condition is no more applicable and calculations have to be performed by considering the real wall morphology, together with the difficulties involved.

Unfortunately, the computational costs prohibit the usage of DNS at the Reynolds numbers commonly encountered in engineering applications. For small values of Δh, the formula (4.25) turns out to be useful to make some predictions of drag reduction at higher Reynolds numbers. If we consider a turbulent flow at $Re = 2800$ and one at $Re = 10^6$, with the same Δh^+, we can obtain that

$$\frac{\Delta C_f|_{Re=10^6}}{\Delta C_f|_{Re=2800}} = \frac{(2C_f)^{-\frac{1}{2}}|_{Re=10^6} + (2k)^{-1}}{(2C_f)^{-\frac{1}{2}}|_{Re=2800} + (2k)^{-1}} \approx 0.6. \tag{4.26}$$

It can thus be argued that the drag reduction advantage decreases with the increase of the Reynolds number. The interpretation embodied by the equation above has been suggested to us by Paolo Luchini.

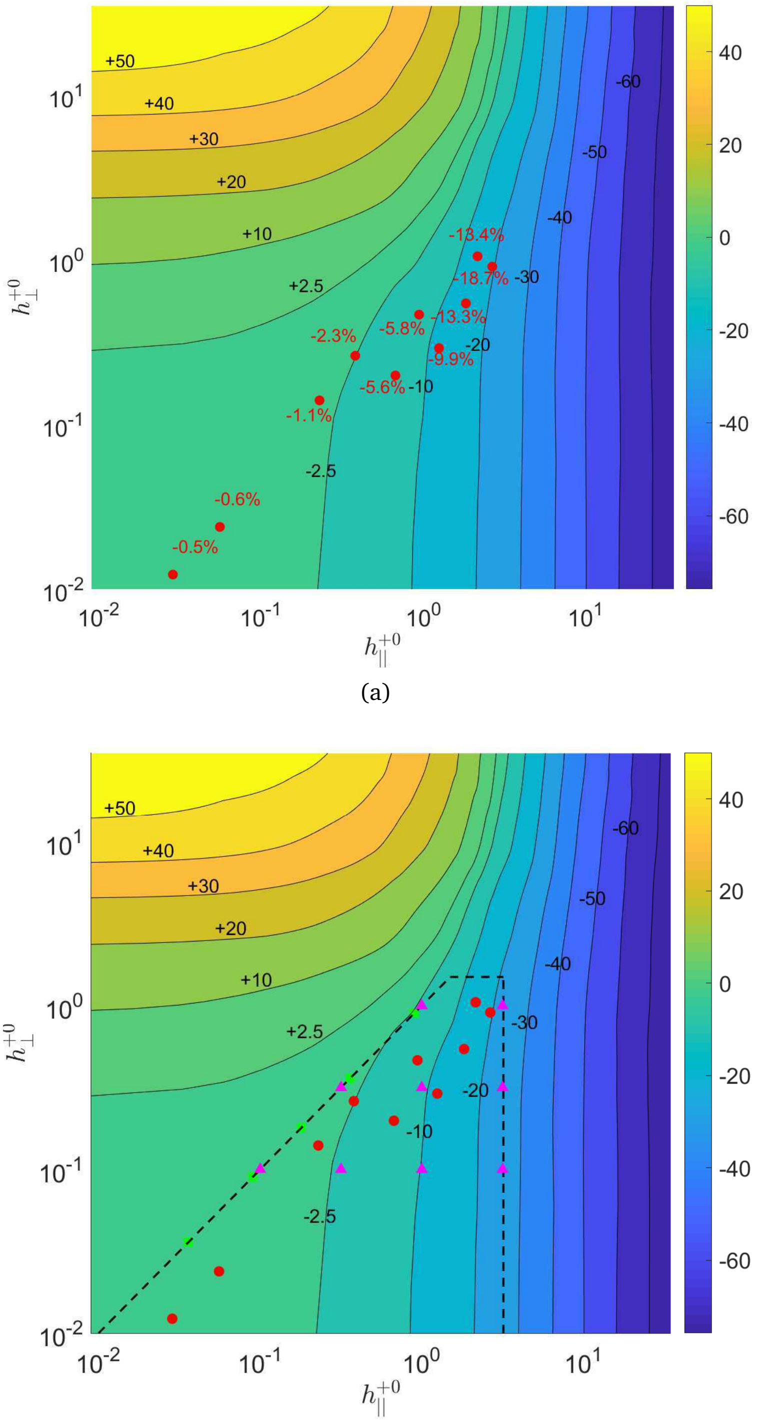

(a)

(b)

Figure 4.3: Iso-contours of percentage drag reduction versus longitudinal and transverse protrusion heights at $Re_\tau = 180$ (adapted from Busse and Sandham [2012]). (a) Comparison of present DNS indicated by red dots together with the reference data for drag reduction; (b) Estimated limits of validity of relation 4.25 (dashed lines) together with the present simulations (red circles), those by Min and Kim [2004] (green squares) and those by Busse and Sandham [2012] (magenta triangles).

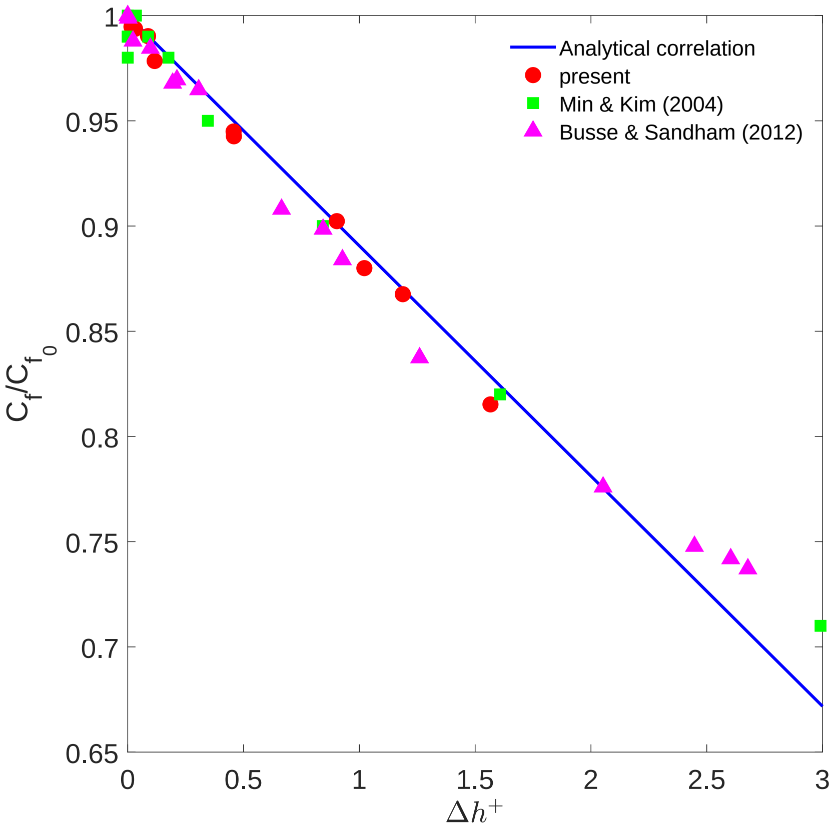

Figure 4.4: Friction factors as function of the difference in protrusion heights in wall units. The cases simulated are reported in table 4.2.

In figure 4.5(a), the mean velocity profiles for different values of Δh^+ are shown. As expected, the profiles are shifted upward with an increasing magnitude with respect to Δh^+, indicating that a drag reduction occurs. Analyzing the root mean square of the components of the velocity fluctuations, presented in figure 4.5(b)-(d), we can note a decrease of the magnitude of the fluctuations for all the velocity components with respect the no-slip case, except in the near-wall region.

In figure 4.6(a)-(b), the contours of the instantaneous spanwise vorticity in a $y - z$ plane shows that the increase of Δh^+ causes a weakening of the vortex structures, due to increased wall slip in the longitudinal direction. This consideration is supported by the visualization of the iso-surfaces of the Q-criterion (see figure 4.6(c)-(d)), which is the second invariant of the velocity gradient tensor, highlighting the turbulent structures attenuation with the increase of Δh^+.

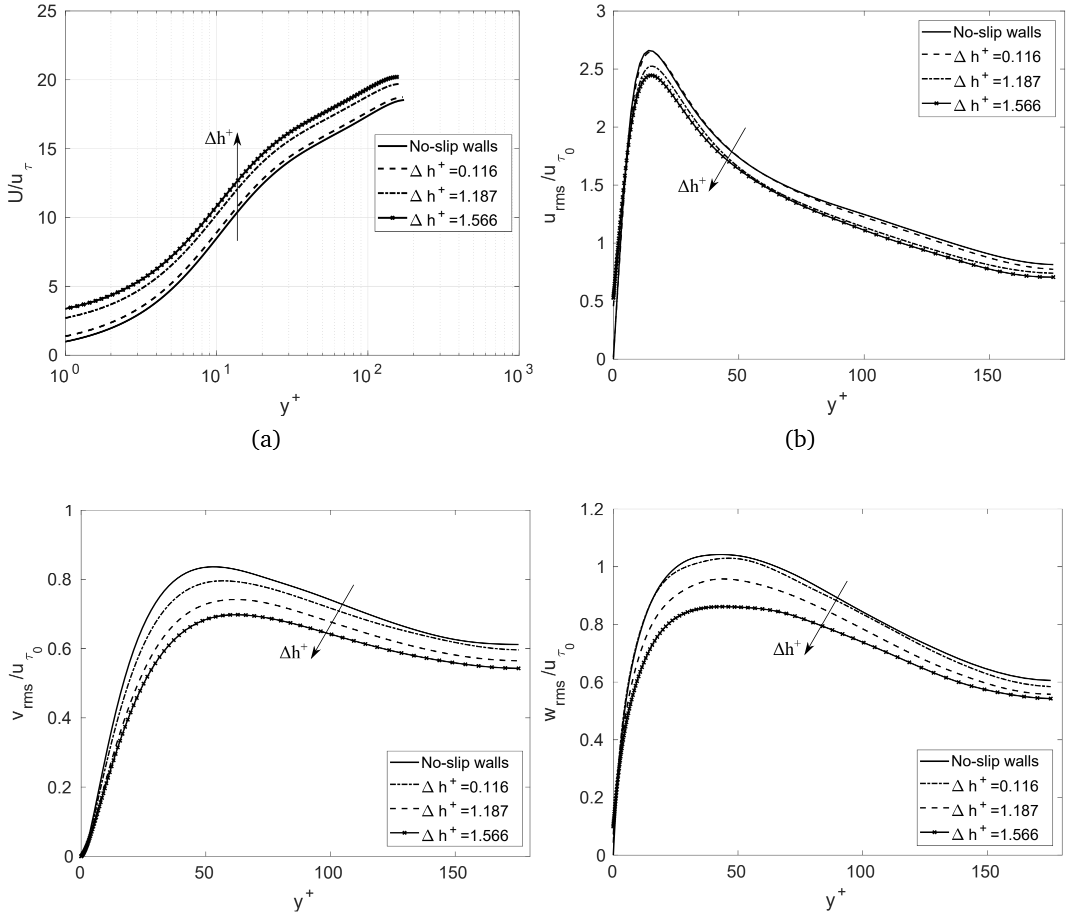

(a) (b)

(c) (d)

Figure 4.5: Turbulent statistics for different values of Δh^+. (a) Mean velocity profiles normalized by the friction velocity u_τ of each case; (b) root mean square of the streamwise velocity component; (c) root mean square of the wall normal velocity component; (d) root mean square of the spanwise velocity component. All the root mean squares are normalized with the friction velocity u_{τ_0} of the reference no-slip case, in order to highlight their decrease in the buffer layer and log-law region.

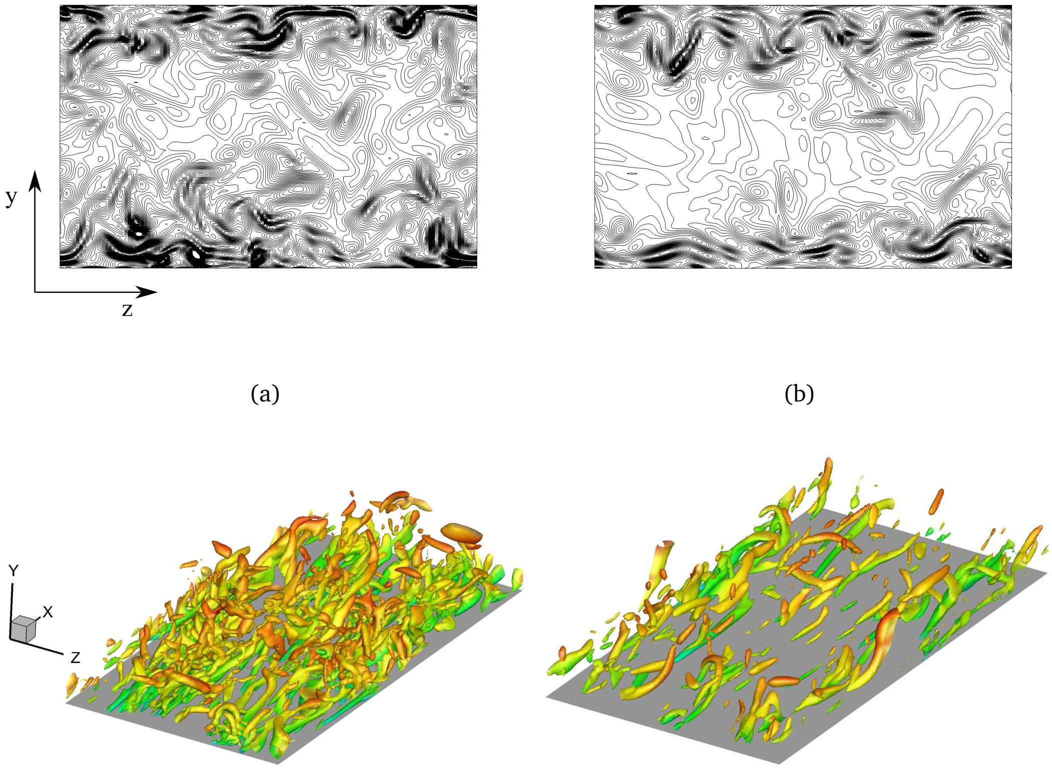

(a) (b)

(c) (d)

Figure 4.6: Turbulent structures inside the channel. (a)-(b) Iso-contours of the instantaneous spanwise vorticity component in the $y - z$ plane at $x = \pi H$ in the range $[-6, 6]$, plotted with an increment of 0.2, for $\Delta h^+ = 0.016$ (left) and $\Delta h^+ = 1.566$ (right); (c)-(d) instantaneous iso-surfaces of the Q-criterion ($Q = 0.7$) for the same cases, colored by the streamwise velocity component.

Table 4.2: Cases selected for direct numerical simulations.

Case	$h_{\|\|}^{\times 10^3}$	$h_{\perp}^{\times 10^3}$	$\Delta h^{\times 10^3}$	Δh^{+}
$\lambda = 0.018, c = 0.50, \Phi = 0.85$	4.46	1.13	3.33	0.457
$\lambda = 0.018, c = 0.50, \Phi = 1.00$	5.34	2.64	2.70	0.458
$\lambda = 0.018, c = 0.50, \Phi = 1.15$	7.09	1.65	5.44	0.902
$\lambda = 0.018, c = 0.70, \Phi = 0.85$	10.38	3.09	7.29	1.187
$\lambda = 0.018, c = 0.70, \Phi = 1.00$	12.24	5.96	6.28	1.022
$\lambda = 0.018, c = 0.70, \Phi = 1.15$	15.09	5.16	9.93	1.566
$\lambda = 20, c = 0.50, \Phi = 0.85$	1.300	0.80	0.50	0.088
$\lambda = 20, c = 0.50, \Phi = 1.00$	0.16	0.069	0.093	0.016
$\lambda = 20, c = 0.70, \Phi = 0.85$	2.16	1.48	0.68	0.116
$\lambda = 20, c = 0.70, \Phi = 1.00$	0.32	0.13	0.18	0.031

Chapter 5

Conclusions and perspectives

The flow over superhydrophic and liquid-impregnated surfaces has been studied from two points of view: the microscopic and the macroscopic one. The microscopic problem has attempted to remove some approximations used in the previous models simulating the flow in the proximity of the wall asperities filled with gas/oil, taking into account different viscosity ratios between the working and the lubricant fluid and the effect of surface tension. The main goal of this problem was the derivation of the protrusion heights as function of the salient geometrical and physical parameters involved in the problem, since they are a direct measure of the drag reduction properties of such coatings. The macroscopic problem has involved direct numerical simulations of a turbulent flow in a plane channel at moderate Reynolds number; the slippage at the walls has been modeled through the Navier boundary conditions, which directly employ the values of the protrusion heights coming from the solution of the microscopic problem. The results can be summarized in the following way:

- The modal analysis of the flow over SHS highlighted the presence of a new streamwise wall-vortex mode in the case of a single SH wall, driven by the wall boundary condition and capable to reduce significantly the value of the Reynolds number for the onset of the instability. The non-modal analysis shows that while the presence of two SH walls yields a slight reduction in energy growth over time, the case of only one SH wall produces an increase of the disturbance kinetic energy for a large range of values of $h_{||}$ when θ is sufficiently greater than zero. It is further shown that, for a single SH wall, beyond a threshold slip length, for values of the inclination angle of the micro-ridges around 45° the gain becomes unbounded with the final target time, a sign of the onset of the wall-vortex modal instability.

- a boundary integral formulation for the longitudinal and the transverse flow over SHS/LIS has been proposed and numerically solved using the boundary element method. The viscosity ratio λ between the working and the lubricant fluid has shown the major non-trivial effect in the variation of both protrusion heights, profoundly altering their behavior as function of the depression into or protrusion out of the wall cavity assumed by the interface. Other interesting features, such as the presence of a maximum value in the transverse slip length for $\lambda < 1$ and its disappearance for $\lambda > 1$, have been well delineated by the calculations.

- a new remedy accounting for mass conservation at low viscosity ratio has been proposed and validated within a standard boundary element framework. The method is easy-to-implement and has given better results with respect to known methodologies [Pozrikidis, 2001];
- the direct numerical simulations have showed that slippage at the walls can be conveniently modeled through the Navier boundary conditions, at least as long as the periodicity of the wall texture is smaller than $b^+ \approx 20$. The most important parameter impacting drag reduction has been found mainly in the quantity $\Delta h = h_{||} - h_{\perp}$ [Luchini et al., 1991], but some care is needed since the flow is more influenced by the value of the longitudinal protrusion height $h_{||}$, with this effect growing with the slippage in the streamwise direction [Luchini, 2015]. However, up to the limit of applicability of the Navier boundary conditions, to consider the drag reduction as function only of Δh is a reasonable approximation. Moreover, the simulations have shown a very good agreement with the analytical correlation proposed by Luchini [1996], which can be conveniently used for a quick approximation of the drag reduction induced by SHS, LIS or, in general, non-smooth walls.

Future developments

This work presents some natural extensions that could lead to a better understanding of the slippage and drag reduction phenomena induced by SHS/LIS coatings:

- The study of flow over different wall coatings has been undertaken primarily assuming the decoupling of the Stokes equation into two almost stand-alone problems (i.e. the transverse and the longitudinal problem). This simplification is not possible in the case of general three dimensional lattices, which have not been studied yet with the same details as the two dimensional geometries;
- there are few numerical simulations or models analyzing the robustness of the interface under working conditions. This is a very important point in practical applications and a challenge from a numerical point of view. For LIS, which up to today seem to be most promising in terms of large scale applications, it would be interesting to study non-newtonian effects on the physics of the interface and their consequences on the slippage properties of the surfaces;

- there are several works studying the turbulent flow over SHS/LIS with various degrees of approximation at the walls (Navier boundary conditions, striped no-slip/no-shear surfaces with different textures etc.). The simulations are limited to moderate Reynolds numbers and thus, could be interesting to study the effect of slippage on turbulence at high Reynolds number, for example through large eddy simulations;
- direct numerical simulations of turbulent flow over SHS/LIS, including gas/oil cavities at the walls without taking advantage of any approximation, is a fascinating topic even if computationally very expensive. A step in this direction has been made recently by Seo et al. [2018], even if a full dynamic coupling of the lubricant layer with the external fluid still needs to be dealt with.

Bibliography

E. Alinovi and A. Bottaro. A boundary element method for Stokes flows with interfaces. *J. Comput. Phys.*, Volume 356:261–281, 2018. doi: https://doi.org/10.1016/j.jcp.2017.12.004.

E. Asmolov and O. Vinogradova. Effective slip boundary conditions for arbitrary one-dimensional surfaces. *J. Fluid Mech.*, 706:108–117, 2012. doi: http://dx.doi.org/10.1017/jfm.2012.228.

W. Barthlott and C. Neinhuis. Purity of the sacred lotus, or escape from contamination in biological surfaces. *Planta*, 202(1):1–8, 1997. doi: https://doi.org/10.1007/s004250050096.

M. Z. Bazant and O. I. Vinogradova. Tensorial hydrodynamic slip. *J. Fluid Mech.*, 613:125–134, 10 2008. ISSN 1469-7645. doi: https://doi.org/10.1017/S002211200800356X.

D. W. Bechert and M. Bartenwerfer. The viscous flow on surfaces with longitudinal ribs. *J. Fluid Mech.*, 206:105–129, 1989. doi: https://doi.org/10.1017/S0022112089002247.

D. W. Bechert, M. Bruse, W. Hage, J. G. T. V. D. Hoeven, and G. Hoppe. Experiments on drag-reducing surfaces and their optimization with an adjustable geometry. *J. Fluid Mech.s*, 338:59–87, 1997. doi: https://doi.org/10.1017/S0022112096004673.

A. V. Belyaev and O. I. Vinogradova. Effective slip in pressure-driven flow past super-hydrophobic stripes. *J. Fluid Mech.*, 652:489–499, 6 2010. ISSN 1469-7645. doi: https://doi.org/10.1017/S0022112010000741.

A. Bottaro. Superhydrophobic surfaces for drag reduction. *Istituto Lombardo (Rend. Scienze)*, 148:239–268, 2014.

O. Buhaug, J. Corbett, V. Eyring, O. Endresen, J. Faber, S. Hanayama, D. S. Lee, D. Lee, A. Lindstad, H. nad Markowska, A. Mjelde, D. Nelissen, C. Palsson, J. Winebrake, W.-Q. Wu, K. Yoshida, and J. Nilsen. Prevention of air pollution from ships: second imo ghg study. *London: International Maritime Organization*, 2009.

A. Busse and N. D. Sandham. Volume of fluid (vof) method for the dynamics of free boundaries. *Phys. Fluids*, 24:055111, 2012. doi: https://doi.org/10.1063/1.4719780.

A. B. D. Cassie and S. Baxter. Wettability of porous surfaces. *J. Chem. Soc. Faraday Trans*, 40:546, 1944. doi: https://doi.org/10.1039/TF9444000546.

C.-H. Choi and C.-J. Kim. Large slip of aqueous liquid flow over a nanoengineered superhydrophobic surface. *Phys. Rev. Lett.*, 96:066001, 2006. doi: https://doi.org/10.1103/PhysRevLett.96.066001.

H. Choi, P. Moin, and J. Kim. Active turbulence control for drag reduction in wall-bounded flows. *J. Fluid Mech.*, 262:75–110, 1994. doi: https://doi.org/10.1017/S0022112087000892.

A. J. Chorin. Numerical solution of the navier-stokes equations. *Math. Comp.*, 22:745–762, 1968. doi: https://doi.org/10.1090/S0025-5718-1968-0242392-2.

D. Crowdy. Slip length for longitudinal shear flow over a dilute periodic mattress of protruding bubbles. *Phys. Fluids*, 22:121703, 2010. doi: https://doi.org/10.1063/1.3531683.

D. Crowdy. Effective slip lengths for longitudinal shear flow over partial-slip circular bubble mattresses. *Fluid Dynamics Research*, 47:065507, 2015. doi: https://doi.org/10.1088/0169-5983/47/6/065507.

A. M. Davis and E. Lauga. Geometric transition in friction for flow over a bubble mattress. *Physics of Fluids*, 21(1):011701, 2009. doi: http://dx.doi.org/10.1063/1.3067833.

A. K. Epstein, T.-S. Wong, R. A. Belisle, E. M. Boggs, and J. Aizenberg. Liquid-infused structured surfaces with exceptional anti-biofouling performance. *Proceedings of the National Academy of Sciences*, 109:13182–13187, 2012. doi: https://doi.org/10.1073/pnas.1201973109.

F. L. Frederick. Scaling law for contoured length of engineering surfaces. *J. Appl. Phys.*, 62(6):2570–2572, 1987. doi: https://doi.org/10.1063/1.339427.

K. Fukagata and N. Kasagi. A theoretical prediction of friction drag reduction in turbulent flow by superhydrophobic surfaces. *Phys. Fluids*, 18:051703, 2006. doi: https://doi.org/10.1063/1.2205307.

J. J. Gagnepain and C. Roques-Carmes. Fractal approach to two-dimensional and three-dimensional surface roughness. *Wear*, 109(1):119–126, 1986. doi: https://doi.org/10.1016/0043-1648(86)90257-7.

R. García-Mayoral and J. Jiménez. Drag reduction by riblets. *Philosophical Transactions of the Royal Society of London A: Mathematical, Physical and Engineering Sciences*, 369(1940):1412–1427, 2011. doi: https://doi.org/10.1098/rsta.2010.0359.

A. Giacomello, S. Meloni, M. Chinappi, and C. M. Casciola. Cassie-Baxter and Wenzel states on a nanostructured surface: Phase diagram, metastabilities, and transition mechanism by atomistic free energy calculations. *Langmuir*, 28(29):10764–10772, 2012. doi: https://doi.org/10.1021/la3018453.

G. H. Golub and C. F. Van Loan. *Matrix computations 2nd edition*. John Hopkins University Press, 1989.

D. J. E. Harvie, M. R. Davidson, and M. Rudman. An analysis of parasitic current generation in volume of fluid simulations. In R. May and A. J. Roberts, editors, *Proc. of 12th Computational Techniques and Applications Conference CTAC-2004*, volume 46, pages C133–C149, Apr. 2005. doi: https://doi.org/10.1016/j.apm.2005.08.015.

C. W. Hirt and B. D. Nichols. Volume of Fluid (VoF) method for the dynamics of free boundaries. *Journal of Computational Physics*, 39(1):201–225, 1981. doi: http://dx.doi.org/10.1016/0021-9991(81)90145-5.

S. H. Hsu and W. Sigmund. Artificial hairy surfaces with a nearly perfect hydrophobic response. *Langmuir Letter*, 26:1504–1506, 2010. doi: https://doi.org/10.1021/la903813g.

J. Hyväluoma and J. Harting. Slip flow over structured surfaces with entrapped microbubbles. *Phys. Rev. Lett.*, 100:246001, 2008. doi: https://doi.org/10.1103/PhysRevLett.100.246001.

J. Jiménez. The structure and control of near wall turbulence. *Phys. Fluids*, 6:994, 1994. doi: https://doi.org/10.1017/S0022112087000892.

J. Jiménez. Turbulent flows over rough walls. *Annu. Rev. Fluid Mech.*, 36:173–196, 2004. doi: https://doi.org/10.1146/annurev.fluid.36.050802.122103.

J. T. Katsikadelis. *Boundary elements theory and applications*. Elsevier, 2002.

J. Kim and P. Moin. Application of a fractional-step method to incompressible navier-stokes equations. *J. Comp. Phys.*, 59:308–323, 1985. doi: https://doi.org/10.1016/0021-9991(85)90148-2.

J. Kim, P. Moin, and R. Moser. Turbulence statistics in fully developed channel flow at low reynolds number. *J. Fluid Mech.*, 177:133–166, 1987. doi: https://doi.org/10.1017/S0022112087000892.

E. Lauga and C. Cossu. A note on the stability of slip channel flows. *Phys. Fluids*, 17:088106, 2005. doi: https://doi.org/10.1063/1.2032267.

E. Lauga and H. A. Stone. Effective slip in pressure-driven Stokes flow. *J. Fluid Mech.*, 489:55–77, 2003. doi: https://doi.org/10.1017/S0022112003004695.

C. Lee and C. J. Kim. Maximizing the giant liquid slip on superhydrophobic microstructures by nanostructuring their sidewalls. *Langmuir*, 25:12812–12818, 2009. doi: https://doi.org/10.1021/la901824d.

P. Luchini. Effects of riblets on the growth of laminar and turbulent boundary layers. In K. K. P. K. S. Choi and T. V. Truong, editors, *Emerging Techniques in Drag Reduction*, pages 101–116, Berlin, Germany, 1992. Mech. Eng. Publ.

P. Luchini. Reducing the turbulent skin friction. In *European Congress on Computational Methods in Applied Sciences and Engineering,- ECCOMAS 1996; 1996, Paris, France*, 1996.

P. Luchini. Linearized no-slip boundary conditions at a rough surface. *J. Fluid Mech.*, 737:349–367, 2013. doi: https://doi.org/10.1017/jfm.2013.574.

P. Luchini. The relevance of longitudinal and transverse protrusion heights for drag reduction by a superhydrophobic surface. In *European Drag Reduction and Flow Control Meeting - EDRFMC 2015; March 23-26, 2015, Cambridge, U.K.*, pages 81–82, 2015.

P. Luchini and A. Bottaro. Adjoint equations in stability analysis. *Annu. Rev. Fluid Mech.*, 46:493–517, 2014. doi: https://doi.org/10.1146/annurev-fluid-010313-141253.

P. Luchini, F. Manzo, and A. Pozzi. Resistance of a grooved surface to parallel flow and cross-flow. *Journal of Fluid Mechanics*, 228:87–109, 1991. doi: https://doi.org/10.1017/S0022112091002641.

B. B. Mandelbrot, D. E. Passoja, and A. J. Paullay. Fractal character of fracture surfaces of metals. *Nature*, 308(5961):721–722, 1984. doi: https://doi.org/10.1038/308721a0.

M. B. Martell, J. B. Perot, and J. P. Rothstein. Direct numerical simulations of turbulent flows over superhydrophobic surfaces. *J. Fluid Mech.*, 620:31–41, 2009. doi: https://doi.org/10.1017/S0022112008004916.

M. B. Martell, J. P. Rothstein, and J. B. Perot. An analysis of superhydrophobic turbulent drag reduction mechanisms using direct numerical simulation. *Phys. Fluids*, 22:065102, 2010. doi: https://doi.org/10.1063/1.3432514.

D. D. Maynes, N. N. Tullett, R. R. Nielson, J. J. Vanderhoff, and B. W. Webb. Influence of superhydrophobic walls on the thermal transport to liquid droplets. In *Heat and Mass Transport Processes, Parts A and B*, volume 10, pages 427–435, 2011.

T. Min and J. Kim. Effects of hydrophobic surface on skin-friction drag. *Phys. Fluids*, 16:L55, 2004. doi: https://doi.org/10.1063/1.1755723.

T. Min and J. Kim. Effects of hydrophobic surface on stability and transition. *Phys. Fluids*, 17:108106, 2005. doi: https://doi.org/10.1063/1.2126569.

A. Mohammadi, H. Moradi, and J. Floryan. New instability mode in a grooved channel. *J. Fluid Mech.*, 778:691–720, 2015. doi: https://doi.org/10.1017/jfm.2015.399.

C. L. M. H. Navier. Memoire sur les lois du mouvement des fluides. *Mem. Acad. R. Sci. Inst. Fr.*, 6:389, 1823. doi: http://www.jstor.org/stable/107159.

C.-O. Ng and C. Y. Wang. Effective slip for Stokes flow over a surface patterned with two- or three-dimensional protrusions. *Fluid Dynamics Research*, 43:065504, 2011.

M. A. Nilsson, R. J. Daniello, and J. P. Rothstein. A novel and inexpensive technique for creating superhydrophobic surfaces using teflon and sandpaper. *Journal of Physics D: Applied Physics*, 43(4):045301, 2010. doi: http://stacks.iop.org/0022-3727/43/i=4/a=045301.

D. M. Nosenchuck and G. L. Brown. *Discrete spatial control of wall shear stress in a turbulent boundary layer*, pages 689–698. Elsevier Science Publishers B.V., New York, 1993. doi: https://doi.org/10.1007/978-3-642-50971-1_44.

M. Omidyeganeh and U. Piomelli. Large-eddy simulation of three-dimensional dunes in a steady, unidirectional flow. Part 1. Turbulence statistics. *J. Fluid Mech.*, 721:454–483, 2013. doi: https://doi.org/10.1017/jfm.2013.36.

openFOAM. *OpenFOAM. The Open Source CFD Toolbox. User Guide*, 2015. URL `http://www.openfoam.org`.

J. Ou and J. P. Rothstein. Direct velocity measurements of the flow past drag-reducing ultrahydrophobic surfaces. *Phys. Fluids*, 17:103606, 2005. doi: https://doi.org/10.1063/1.2109867.

J. Ou and J. P. Rothstein. Drag reduction in turbulent flows over superhydrophobic surfaces. *Phys. Fluids*, 21:085103, 2009. doi: https://doi.org/10.1063/1.3207885.

J. Ou, B. Perot, and J. P. Rothstein. Laminar drag reduction in microchannels using ultrahydrophobic surfaces. *Phys. Fluids*, 16:4635, 2004. doi: https://doi.org/10.1063/1.1812011.

S. Ozbay, C. Yucee, and H. Y. Erbil. Improved icephobic properties on surfaces with a hydrophilic lubricating liquid. *ACS Appl. Mater. Interfaces*, 39:22067–22077, 2015. doi: https://doi.org/10.1021/acsami.5b07265.

H. Park, G. Sun, and C. J. Kim. Superhydrophobic turbulent drag reduction as a function of surface grating parameters. *J. Fluid Mech.*, 747:722–734, 2014. doi: https://doi.org/10.1017/jfm.2014.151.

J. B. Perot. An analysis of the fractional step method. *J. Comput. Phys.*, 108:51–58, 1993. doi: https://doi.org/10.1006/jcph.1993.1162.

J. R. Philip. Flows satisfying mixed no-slip and no-shear conditions. *Z. Andew. Math. Phys.*, 23:353–370, 1972. doi: https://doi.org/10.1007/BF01595477.

A. Pinelli, M. Omidyeganeh, C. Brücker, A. Revell, A. Sarkar, and E. Alinovi. The PEL-skin project: Part IV—Control of bluff body wakes using hairy filaments. *Meccanica*, 52:1503–1514, 2017. doi: https://doi.org/10.1007/s11012-016-0513-0.

C. Pozrikidis. *BEMLIB*. URL `http://dehesa.freeshell.org/BEMLIB/`.

C. Pozrikidis. *Boundary integral and singularity methods for linearized viscous flow*. Cambridge University Press, 1992.

C. Pozrikidis. Computation of periodic green's functions of stokes flow. *J. Engrg. Math.*, 30:79–96, 1996. doi: https://doi.org/10.1007/BF00118824.

C. Pozrikidis. Expansion of a compressible gas bubble in Stokes flow. *J. Fluid Mech.*, 442:171–189, 2001. doi: https://doi.org/10.1017/S0022112001004992.

C. Pozrikidis. *A practical guide to boundary element methods with the software library BEMLIB*. CRC Press, 2002.

A. Q. Raeini, M. J. Blunt, and B. Bijeljic. Modelling two-phase flow in porous media at the pore scale using the volume-of-fluid method. *J. Comput. Phys.*, 231:5653 – 5668, 2012. doi: https://doi.org/10.1016/j.jcp.2012.04.011.

D. Rawlings and K. Malone. Rigid tipped riblets, Apr. 1 2014. URL `https://www.google.com/patents/US8684310`. US Patent 8,684,310.

C. M. Rhie and L. Chow. Numerical study of the turbulent flow past an airfoil with trailing edge separation. *AIAA*, 21:1525–1532, 1983. doi: https://doi.org/10.2514/3.8284.

C. Roelands. Correlational aspects of the viscosity-temperature-pressure relationship of lubricating oils. *Ph.D. Thesis, TU Delft*, 1966.

B. J. Rosenberg, T. Van Buren, M. K. Fu, and A. J. Smits. Turbulent drag reduction over air- and liquid- impregnated surfaces. *Phys. Fluids*, 28:015103, 2016. doi: https://doi.org/10.1063/1.4939272.

M. E. Rosti, M. Omidyeganeh, and A. Pinelli. Direct numerical simulation of the flow around an aerofoil in ramp-up motion. *Phys. Fluids*, 28:025106, 2016. doi: https://doi.org/10.1063/1.4941529.

J. G. Savins. A stress-controlled drag-reduction phenomenon. *Rheologica Acta*, 6(4): 323–330, 1967. doi: https://doi.org/10.1007/BF01984629.

M. Sbragaglia and A. Prosperetti. Effective velocity boundary condition at a mixed slip surface. *Journal of Fluid Mechanics*, 578:435–451, 2007. doi: https://doi.org/10.1017/S0022112007005149.

P. Schmid and D. Henningson. *Stability and Transition in Shear Flows*. Number v. 142 in Applied Mathematical Sciences. Springer, New York, 2001.

C. Schönecker and S. Hardt. Longitudinal and transverse flow over a cavity containing a second immiscible fluid. *J. Fluid Mech.*, 717:376–394, 2013. doi: https://doi.org/10.1017/jfm.2012.577.

C. Schönecker, T. Baier, and S. Hardt. Influence of the enclosed fluid on the flow over a microstructured surface in the Cassie state. *J. Fluid Mech.*, 740:168–195, 2014. doi: https://doi.org/10.1017/jfm.2013.647.

J. Seo and A. Mani. On the scaling of the slip velocity in turbulent flows over superhydrophobic surfaces. *Phys. Fluids*, 28(2):025110, 2016. doi: https://doi.org/10.1063/1.4941769.

J. Seo, R. García-Mayoral, and A. Mani. Pressure fluctuations and interfacial robustness in turbulent flows over superhydrophobic surfaces. *J. Fluid Mech.*, 783: 448–473, 2015. doi: https://doi.org/10.1017/jfm.2015.573.

J. Seo, R. García-Mayoral, and A. Mani. Turbulent flows over superhydrophobic surfaces: flow-induced capillary waves, and robustness of air-water interfaces. *J. Fluid Mech.*, 835:45–85, 2018. doi: https://doi.org/10.1017/jfm.2017.733.

A. V. Shenoy. Drag reduction with surfactants at elevated temperatures. *Rheologica Acta*, 15(11):658–664, 1976. doi: https://doi.org/10.1007/BF01524753.

K. S. Sheth and C. Pozrikidis. Effects of inertia on the deformation of liquid drops in simple shear flow. *Computers & Fluids*, 24:101–119, 1994. doi: https://doi.org/10.1016/0045-7930(94)00025-T.

N. Shirtcliffe, G. McHale, M. Newton, G. Chabrol, and C. Perry. Dual-scale roughness produces unusually water-repellent surfaces. *Adv. Mater.*, 16:1929–1932, 2004. doi: https://doi.org/10.1002/adma.200400315.

B. R. Solomon, K. S. Khalil, and K. K. Varanasi. Drag reduction using lubricant-impregnated surfaces in viscous laminar flow. *Langmuir*, 30:10970–10976, 2014. doi: https://doi.org/10.1063/1.3207885.

S. Srinivasan, S. S. Chhatre, J. M. Mabry, R. E. Cohen, and G. H. McKinley. Solution spraying of poly(methyl methacrylate) blends to fabricate microtextured, superoleophobic surfaces. *Polymer*, 52:3209–3218, 2011. doi: https://doi.org/10.1016/j.polymer.2011.05.008.

A. Steinberger, C. Cottin-Bizonne, P. Kleimann, and E. Charlaix. High friction on a bubble mattress. *Nature Materials*, 6(9):665–668, 2007. doi: http://dx.doi.org/10.1038/nmat1962M3.

H. A. Stone, A. D. Stroock, and A. Ajdari. Engineering flows in small devices: microfluidics toward a lab-on-a-chip. *Annu. Rev. Fluid Mech.*, 36:381–411, 2004. doi: https://doi.org/10.1146/annurev.fluid.36.050802.122124.

Y. Su, B. Ji, K. Zhang, H. Gao, Y. Huang, and K. Hwang. Nano to micro structural hierarchy is crucial for stable superhydrophobic and water-repellent surfaces. *Langmuir*, 26:4984–4989, 2010. doi: https://doi.org/10.1021/la9036452.

J. Szodruch. Viscous drag reduction in transport aircraft. *AIAA*, 91:0685, 1991. doi: https://doi.org/10.2514/6.1991-685.

J. Szumbarski. Instability of viscous incompressible flow in a channel with transversely corrugated walls. *J. Theo. Applied Mech.*, 45(3):659–683, 2007.

J. Tanzosh, M. Manga, and H. Stone. Boundary integral methods for viscous free-boundary problems: Deformation of single and multiple fluid-fluid interfaces. In *Boundary Element Technology VII, C.A. Brebbia and M.S. Ingber Eds.*, pages 19–39. Springer, 1992.

C. Teo and B. Khoo. Flow past superhydrophobic surfaces containing longitudinal grooves: effects of interface curvature. *Microfluidics and Nanofluidics*, 9:499–511, 2010. doi: https://doi.org/10.1007/s10404-010-0566-7.

P. Than, L. Preziosi, J. D. D., and M. Arney. Measurement of interfacial tension between immiscible liquids with the spinning road tensiometer. *Journal of Colloid and Interface Science*, 124:552 – 559, 1988. doi: https://doi.org/10.1016/0021-9797(88)90191-9.

S. Turk, G. Daschiel, A. Stroh, Y. Hasegawa, and B. Frohnapfel. Turbulent flow over superhydrophobic surfaces with streamwise grooves. *J. Fluid Mech.*, 747:186–217, 2014. doi: https://doi.org/10.1017/jfm.2014.137.

M. J. Walsh. Effect of detailed surface geometry on riblet drag reduction performance. *Journal of Aircraft*, 27:572–573, 1990. doi: https://doi.org/10.2514/3.25323.

M. J. Walsh and J. B. Anders. Riblet/lebu research at nasa langley. *Applied Scientific Research*, 46:255–262, 1989. doi: https://doi.org/10.1007/BF00404822.

R. Wenzel. Resistance of solid surfaces to wetting by water. *Industr. and Eng. Chemistry*, 28:988–994, 1936. doi: https://doi.org/10.1021/ie50320a024.

B. Xie and F. Xiao. Toward efficient and accurate interface capturing on arbitrary hybrid unstructured grids: The thinc method with quadratic surface representation and gaussian quadrature. *Journal of Computational Physics*, 349:415 – 440, 2017. doi: https://doi.org/10.1016/j.jcp.2017.08.028.

T. Young. An essay on the cohesion of fluids. *Philos. Trans. R. Soc. Lond. B. Biol. Sci.*, 95:65–87, 1805. doi: http://www.jstor.org/stable/107159.

K. Yu, C. Teo, and B. Khoo. Linear stability of pressure-driven flow over longitudinal superhydrophobic grooves. *Phys. Fluids*, 28:022001, 2016. doi: https://doi.org/10.1063/1.4940336.

H. Zhou and C. Pozrikidis. The flow of suspensions in channels: Single files of drops. *Phys. Fluids*, 5:311, 1993. doi: https://doi.org/10.1063/1.858893.